

Naval Research Laboratory

Washington, DC 20375-5000



2

NRL Memorandum Report 6517

Advanced Concepts Theory Annual Report 1988

FINAL REPORT

*Plasma Radiation Branch
Plasma Physics Division*

August 3, 1989

AD-A211 665

This research was sponsored by the Defense Nuclear Agency under Subtask RL RA/Advanced Concepts Development, and Work Unit Title, 00050, "X-Ray Source Development Theory", MIPR No. 88-577.

DTIC
ELECTE
AUG 24 1989
S B D

Approved for public release; distribution unlimited.

88

8

24

1989

REPORT DOCUMENTATION PAGE				Form Approved OMB No 0704-0186	
1a REPORT SECURITY CLASSIFICATION UNCLASSIFIED			1b RESTRICTIVE MARKINGS		
2a SECURITY CLASSIFICATION AUTHORITY			3 DISTRIBUTION / AVAILABILITY OF REPORT Approved for public release; distribution unlimited.		
2b DECLASSIFICATION / DOWNGRADING SCHEDULE					
4 PERFORMING ORGANIZATION REPORT NUMBER(S) NRL Memorandum Report 6517			5 MONITORING ORGANIZATION REPORT NUMBER(S)		
6a NAME OF PERFORMING ORGANIZATION Naval Research Laboratory		6b OFFICE SYMBOL (If applicable) Code 4720	7a NAME OF MONITORING ORGANIZATION		
6c ADDRESS (City, State, and ZIP Code) Washington, DC 20375-5000			7b ADDRESS (City, State, and ZIP Code)		
8a NAME OF FUNDING / SPONSORING ORGANIZATION Defense Nuclear Agency		8b OFFICE SYMBOL (If applicable) RAEV	9 PROCUREMENT INSTRUMENT IDENTIFICATION NUMBER		
8c ADDRESS (City, State, and ZIP Code) Alexandria, VA 22310			10 SOURCE OF FUNDING NUMBERS		
			PROGRAM ELEMENT NO 62715H	PROJECT NO	TASK NO
					WORK UNIT ACCESSION NO DN880-191
11 TITLE (Include Security Classification) Advanced Concepts Theory Annual Report 1988					
12 PERSONAL AUTHOR(S) Code 4720 - Plasma Radiation Branch					
13a TYPE OF REPORT Annual		13b TIME COVERED FROM 1/88 TO 12/88		14 DATE OF REPORT (Year, Month, Day) 1989 August 3	
15 PAGE COUNT 158					
16 SUPPLEMENTARY NOTATION This research was sponsored by the Defense Nuclear Agency under subtask RL RA/Advanced Concepts Development, Work Unit Title, 00050, X-Ray Source Development Theory, MIPR No. 88-577.					
17 COSATI CODES			18 SUBJECT TERMS (Continue on reverse if necessary and identify by block number)		
FIELD	GROUP	SUB-GROUP			
			Z-Pinch physics		
			Radiation MHD		
			Plasma opening switches		
			Non-LTE dynamics		
19 ABSTRACT (Continue on reverse if necessary and identify by block number)					
<p>This report details the work of the Plasma Radiation Branch conducted in FY 88 with respect to several critical problems concerning the design of z-pinch implosions and the optimization of their radiative output. Separate sections describe progress in the analysis of z-pinch experiments, the development of atomic, electron, plasma and MHD dynamical models to describe z-pinch implosions, and the analysis of plasma opening switches.</p>					
20 DISTRIBUTION / AVAILABILITY OF ABSTRACT <input checked="" type="checkbox"/> UNCLASSIFIED/UNLIMITED <input type="checkbox"/> SAME AS RPT <input type="checkbox"/> DTIC USERS			21 ABSTRACT SECURITY CLASSIFICATION UNCLASSIFIED		
22a NAME OF RESPONSIBLE INDIVIDUAL Jack Davis and Kenneth Whitney			22b TELEPHONE (Include Area Code) (202) 7673278		22c OFFICE SYMBOL Code 4720

CONTENTS

EXECUTIVE PROGRAM SUMMARY	v
I. SCALING Z-PINCH PLASMAS WITH ATOMIC NUMBER FOR A GIVEN K-SHELL YIELD	1
II. THEORETICAL AND EXPERIMENTAL COMPARISONS OF GAMBLE II ARGON GAS PUFF EXPERIMENTS	12
III. ANALYSIS PROCEDURES FOR PLASMA RADIATION SOURCE WIRE EXPERIMENTS	23
IV. ELECTRON THERMALIZATION AND RUNAWAY STUDIES	37
V. DIELECTRONIC RECOMBINATION FROM FLUORINE-LIKE IONS	67
VI. THE DENSE Z-PINCH AS A PLASMA RADIATION SOURCE	75
VII. Z-PIMP: A ZERO-D Z-PINCH IMPLOSION CODE	79
VIII. MODELING THE RADIATION HYDRODYNAMICS OF MIXED ELEMENT PULSED POWER DRIVEN LOADS	94
IX. CHARGE EXCHANGE NEUTRAL SIMULATION FOR A REFLEX SWITCH	113
X. CONTINUUM THEORY OF THE REFLEX TRIODE	127
DISTRIBUTION LIST	137



Accession For	
NTIS GRA&I	<input checked="" type="checkbox"/>
DTIC TAB	<input type="checkbox"/>
Unannounced	<input type="checkbox"/>
Justification	
By	
Distribution/	
Availability Codes	
Dist	Avail and/or Special
A-1	

EXECUTIVE PROGRAM SUMMARY

The main goal being addressed in a variety of different ways by the NRL Plasma Radiation Source (PRS) Theory Program is to determine the power scaling relations of different PRS loads using elements from hydrogen to higher atomic number loads such as titanium, iron, copper, selenium, or krypton in order to increase 10 kilovolt photon yields. In working toward the achievement of this goal, ongoing theory activities were conducted this year in a number of interrelated areas. They include the development of:

- o PRS load power scaling relations
- o Data analysis procedures
- o Z scalable atomic models
- o Non-Maxwellian electron dynamical calculations leading to the analysis of runaway electrons and machine decoupling calculations.
- o Scalable M- and L-shell atomic structure opacity calculations
- o Bennett equilibrium models to investigate the radiative performance of dense z-pinch PRS's that are generated by long rise-time current pulses
- o Improvements to existing Branch MHD models
- o Theories to better understand reflex switches

In Section I, simple scaling arguments are summarized as to how specification of a desired total K-shell emission can be used to determine the parameters of an imploding array z-pinch plasma as a function of the atomic number of the pinch. A detailed description of these theoretical arguments was written up for publication in an NRL Memorandum Report. The model

used to derive these scaling relations ignores all hydrodynamic details of the z-pinch implosion and thermalization processes and assumes that all of the plasma mass is imploded and thermalized. The pinch is also assumed to be driven by a prescribed linearly rising current. The scaling laws that are derived from these assumptions, in effect, contain phenomenological scaling parameters whose values will need to be more accurately determined by more detailed theoretical calculations and/or by z-pinch experiments on a variety of different machines.

In Sections II and III, two extensive data analyses are described that were carried out on NRL Gamble II and Maxwell Laboratory Blackjack V (BJ5) experimental data respectively. The results of both analyses were presented at the DNA Advanced Pulse Power Conference and were written up for inclusion in the conference proceedings.

In the first analysis, a comparison was completed of a 1-D MHD theoretical simulation of a Z-pinch gas implosion with the measured results obtained from a series of argon gas puff experiments run at NRL. Specifically, comparisons were made of L- and K-shell emissions and of energy coupling into the diode region. The intention of this work was to compare two key areas where theory and experimental measurements overlap. A side benefit of the analysis was the observation that there are experimental benefits to be reaped if the experimental plasmas could be made to behave more closely as a 1-D snowplow implosion.

Consistently larger L-shell emissions were observed in the experiment (factors of 3) than were theoretically computed. Together with the lower observed experimental K-shell emission (factors of 5) these experimental/theoretical discrepancies suggest that the theoretical plasmas burn through to the K-shell more rapidly due to more thermalization of kinetic energy.

However, perhaps the most interesting result obtained by doing this comparison was the rather large difference between the amount of experimental energy observed to have been expended in the diode region and the amount of energy that the 1-D circuit theory coupled to the plasma load. Except for the largest mass loadings, the amount of energy experimentally measured to be coupled into the diode region was much larger than the theoretical value found to be coupled to the load, by as large as a factor of 4 for some of the smaller loads. This result indicates a large amount of experimental

inefficiency since apparently more energy is being supplied to the experimental plasmas but less K-shell radiation is being produced. There are a number of possible explanations for this result and they are provided in the paper contained in the Proceedings Pulse Power Conference. We conclude from this work that there is a need for more systematic experiments and improved diagnostics coupled with theoretical support that will help us to understand how the machine energy is coupled to the PRS plasma. From this knowledge, we might be able to design experiments that make PRS plasmas behave more like the theoretical plasma and allow us to substantially increase K-shell emission.

The analysis described in Section III of Maxwell's titanium data that was obtained from X-pinch, single wire, and wire array experiments required an extensive data base of computer generated results, which themselves were processed and carefully analyzed. A detailed description of these analysis procedures and of the tentative conclusions that were drawn from them has been published as an NRL Memorandum Report No. 6383. This analysis was made on three of the optimal PRS experiments, which were obtained by varying the amount of mass per unit length to maximize the total K-shell radiated energy. The three optimal shots analyzed - one six-wire array, one single wire, and one six-wire X-pinch - all yielded around 300 to 400 J in the K-shell region. Their initial optimal mass loadings, however, varied over a considerably larger range from 90 to 1460 $\mu\text{g}/\text{cm}$.

It is important to theoretically estimate and compare the plasma conditions giving rise to the K-shell emission in the different experiments. For this analysis, a completely systematic approach was developed which takes into account uncertainties in the experimental measurements and which can be applied to the L-shell or other experiments.

The results of the analysis showed that both the single wire and the X-pinch geometries produced denser, more concentrated emission regions compared with the wire array. Most significantly, it would also appear from these experiments, that though a large initial mass is necessary to achieve good machine coupling, only a small fraction of the original mass participated in the super-kilovolt x-ray conversion at later times.

The above two analyses of experimental data achieved three objectives. One, they provided quantitative data sets for experimental-theoretical

comparisons that can be used in the future to evaluate the effects that improvements in our theoretical models will have on our understanding of the PRS load dynamics. Two, they raised a number of important empirical questions. And three, they suggest future directions to move in order to seek some answers.

Some of the questions that were raised are:

1. Why is more energy coupled into the diode region than can be coupled by a circuit into a model, thermalized, PRS load? Where does the extra energy go? Does it go into longitudinal plasma motion, radiation, into runaway electrons on axis, or is it stored in the coronal (gyrokinetic) plasma that surrounds the PRS load?
2. Do the different geometry PRS loads always tend to produce comparable yields when optimized machine coupling for each load is achieved or was this an accidental finding of the titanium experiments? What determines the different fractional mass participations that are observed to produce these yields? Do these observations suggest that mixed element PRS loads must be designed in order to simultaneously maintain good machine coupling and increase K-shell yields at 10 kilovolts?

Future work in the Plasma Radiation Branch will address problems of instability growth, runaway electrons, and mixed element MHD in order to address these questions. One mechanism under investigation for load decoupling is the possibility of runaway electron production. To address this problem, last year's calculation of non-Maxwellian electron distribution functions has been extended to the case where the distribution changes due to the time evolving plasma conditions that are present in a wire array PRS implosion. This work is described in Section IV. The electron calculation consists of a post-analysis of a z-pinch MHD calculation. Solutions to a Fokker-Planck equation are obtained as a function of time with this equation receiving information from the MHD calculation on the strength of electric and magnetic fields and about the plasma implosion history including velocities, positions, and electron densities. From these solutions, one can determine the extent to which ohmic and compressional heating drive the electrons from a Maxwellian distribution. Only one MHD run has been analyzed to date. The

results of the calculation did not show runaway electron production at the time of plasma collapse and x-ray production due to the relative strengths of the electric and magnetic fields. This theoretical finding is in contrast to some experimental evidence that shows that runaway electrons are, in fact, generated at this time. This discrepancy between theory and experiment is currently under investigation.

Work has also proceeded in several directions to understand the scaling of PRS loads with atomic number, Z , and with machine input power. The first-generation development of a Z -scalable atomic model was completed this year and it has been successfully utilized to carry out both detailed radiation transport and the 1-D MHD array implosion calculations described above to analyze the electron problem. This model enables us to include excited state structure in all of the ionization stages throughout the L-, M- and N-shells, and not just in the last dozen or so as has been done in the past. This capability will allow us to model any load from argon, titanium and copper, through selenium and krypton, which will be very useful for future wire and gas puff studies.

Besides its scalability, the model has the further desirable feature that it keeps the ionization calculations simple while allowing one to realistically calculate the effects of the detailed and complex atomic structure on opacity in the L- and M-shell. These calculations are extremely important for obtaining accurate scalable values of radiation loss rates for MHD implosion calculations. One simply puts back the multiplet structure of an ion into the radiation transport opacity calculation that is left out of the ionization calculation.

Progress in this direction this year proceeded as follows. The multiplet structure for the $\Delta n=0$ transitions was completed for sodiumlike through argonlike ions. By using the multiplet factors, the $\Delta n=0$ line profiles can be split into their component parts, corresponding to the different configurations and states in an ion. This provides a much more accurate calculation of the opacity in these transitions and of how this opacity affects the radiation losses in the M-shell than can be done using purely hydrogenic approaches. Using Z -scaled atomic data and the same multiplet structure, the radiation loss rate for the $\Delta n=0$ transitions in the M-shell

were calculated for optically thick selenium plasmas. The results from this analysis were published in the IEEE Transactions on Plasma Science, 16, 552, October 1988. The study indicates that, as the ion density increases above the coronal limit, $\Delta n \neq 0$ transitions contribute progressively more to the radiative cooling rate. It was found that line emission from the $\Delta n \neq 0$ transitions and plasma opacity are generally more important to the calculation of selenium radiation cooling rates than line emission from the $\Delta n = 0$ transitions. However, getting the line structure right is crucial to the accurate calculation of any radiation loss rate. Better results are expected as multiplet structure in the $\Delta n = 1$ and 2 levels is included in both L- and M-shells, and as further line structure, such as spin-orbit coupling, is added. As a first step towards including the effects of spin-orbit splitting in the Z-scalable atomic model, we are looking at the importance of the $3p$ ($^2P_{3/2}$) to $3s$ ($^2S_{1/2}$) transition in sodiumlike selenium to plasma diagnostics of M-shell plasma emission conditions.

Because of the significance of atomic scaling relations to PRS load design, an important part of the Plasma Radiation Branch's work concerns the development of a reliable data base of scalable atomic data. As we scale to moderate Z plasmas, such as Ti through Kr, one of the weakest areas in our data base development concerns the calculation of dielectronic recombination (DR) rates. They are an important recombination process for high temperature plasmas and the DR rate coefficients are necessary tools for plasma diagnostics.

Most of the previous work on DR, report total ground-state-to-ground-state rate coefficients as a function of temperature. However, separate bookkeeping and presentation of partial atomic data such as energies, autoionization rates, radiative rates and dielectronic recombination rates are extremely important for many reasons. With only the total rate coefficients it is not possible to study the density effect on these rates and to calculate DR rates accurately at densities of PRS interest; dielectronic recombination rates to these specific final excited states are needed.

Work in this area to develop the necessary procedures to calculate the partial as well as the total DR rates in the isoelectronic sequence for Argon through Krypton is discussed in Section V along with a first application of these rates. These data will be used in FY 89 for obtaining Z-scaling laws

for both the autoionization and the DR rate coefficients. Once such scaling laws are available, it will be possible to carry out more accurate analyses of the feasibility of different elements as plasma sources for Z-pinchs.

One of the applications of the above work of special interest will be to the interpretation of the x-ray data obtained at Physics International using nickel exploding wires. They obtained some beautifully resolved satellite spectra in their K-shell data. The analysis of this data should yield important information on the runaway electron content of these plasmas and provide a consistency check on the thermal analysis of Ti described in Section III.

There has also been a substantial amount of work done on studying the dynamics of Dense Z-Pinch Plasma Radiation Source (DZPRS) loads. Because of the $1/r$ nature of the magnetic force and the fact that these loads are located on the axis of a Z-pinch, it should be possible to couple more energy into a DZPRS load than a conventional gas puff.

We have been investigating a new idea involving the "radiative collapse" of the plasma, whereby a fiber of deuterium or a thin wire of some other material, such as aluminum, is collapsed on axis by radiative cooling. This type of implosion is inherently different from the conventional way of doing PRS work. Although current passes through the plasma as in the conventional array PRS, the time rate of change of this current is very small. This reduces the effects of inertial forces and should, in principle, produce a stable pinch -- there is some experimental evidence for this stability. This leads to a physical state known as "Bennett-equilibrium" in which the average particle pressure of the plasma is balanced by the magnetic field pressure at the boundary of the plasma. When this occurs, the only forces controlling the expansion or contraction of the plasma come from the relative strengths of the radiative cooling rate and ohmic heating rate. If the radiative rates dominate, then the plasma will collapse, hence the name "radiative collapse". In general the ohmic heating rate is larger than the radiative cooling rate until the time at which the current becomes greater than or equal to the "Pease-Braginskii" current.

The reason for investigating this type of configuration is that we want to produce terrawatts of radiation in the 3-15 keV range without resorting to excessively powerful pulse power machines. In the past people have tried, using conventional PRS techniques, to produce radiation in this range on

relatively modest machines, such as Gamble II, by going to extremely small mass loadings. Because the densities achieved in these implosions never got much above 10^{19} cm^{-3} the yields were never large. It is hoped that the stability and increased density of these "radiative collapsed" loads will overcome some of the conventional PRS problems. Simple theoretical results show that over 50 kJ of > 3 keV radiation can be produced with modest machines. The modeling of this dynamics requires high density equations of state and conductivity models to take into account plasma degeneracy and strongly coupled plasma effects. A brief summary of this work is given in Section VI.

Because of the evolving nature of the PRS program as new concepts in plasma load design are proposed, it is useful to model plasma implosions using zero-dimensional radiation-hydrodynamics as a succinct and rapid theoretical resource. In particular, it is useful to investigate different parameter regimes of radiative collapse with such a computer code. A newly improved zero-D computer model called ZPIMP was constructed this year to investigate these plasma implosions. For the hydrodynamic equations, this code is structured much like a typical multi-zone 1-D simulation code. The spatial and temporal finite difference forms of the hydrodynamic equations are derived in detail. These results are then reduced to three zones, with most of the mass contained in the central zone, which is characterized by an averaged density, ion temperature, and electron temperature. This finite difference approach to the hydrodynamics in particular, allows one to calculate separate velocities for the inner and outer radii of the shell. The ionization dynamics is handled by a non-LTE CRE model and the probability-of-escape method for radiative transfer is used to handle opacity and trapping effects in the lines.

This zero-D model was used to determine the implosion time, final radius, maximum charge state, temperature, and peak radiated power of an aluminum vapor in annular shells and filled cylinders for various mass loadings, initial radii, and initial shell thicknesses. Circuit parameters for these calculations were chosen to match the NRL GAMBLE II device

This code and the results of these calculations are discussed in detail in an NRL Memorandum Report ZPIMP: A Zero-D Z-Pinch Implosion Code, by J. L. Giuliani and J. Rogerson, which has been recently published. A summary of this work is presented in Section VII. Presently, investigations with this simulation code are underway to determine those initial conditions, such as

outer and inner puff gas radii and mass loading, which will optimize the aluminum K-shell yield on the Gamble II machine in experiments that are planned for FY89.

We are also presently simulating recent structured target PRS experiments on the Physics International DNA/PITHON pulsed power generator with a multimaterial radiation-hydrodynamics model. This ongoing work is described in Section VIII. The experiments at PI involve the implosion of a cylindrical neon puff-gas onto a thin layered Al/CH target. The goal of the experiments is to produce a stable, uniform and efficient x-ray source. It is known from experiments involving double puffs that the presence of a central core plasma enhances stability and overall radiating efficiency.

A self-consistent multimaterial radiation-hydrodynamics model with non-LTE ionization dynamics and radiation transport is being employed in the simulations. Detailed atomic models for neon and aluminum have been used in calculating the ionization state, radiation emission, and radiation transport in the puff-gas and target plasmas.

Because experiments involving more than one element are difficult to interpret, a series of computer simulations have been carried out with the above-mentioned non-LTE radiation hydrodynamics model. A typical experiment involves the discharge of hundreds of kilojoules of electrical energy through a cylindrical neon gas puff, heating it and imploding it radially at speeds of about $3-5 \times 10^7$ cm/sec; the gas puff impinges and stagnates onto a thin aluminum coated capillary, converting the kinetic energy of implosion into thermal energy. Rapid plasma heating in the stagnation region results in ionization of the aluminum to the K-shell and partial stripping of the neon. In addition, K-shell radiation from both the aluminum and the neon can produce strong photopumping and enhanced ionization in adjacent plasma. The hot, dense plasma in the stagnation region can undergo rapid radiative cooling and recombination. In fact, anomalous brightness was initially reported in the 4f-3d and 4d-3p lines of Al XI and the 4-3 line of Ne X; however, opacity considerations made interpretation of the aluminum results difficult. In simulating experiments where gas puffs impinge on solid density targets, it is crucial that the dynamics of the target be modeled correctly. In addition to radiative preheat from the hot puff gas, some current may flow through the target at early times. This possibility has generally been neglected in

simulations of pulsed power implosions, but even if the current is quickly choked off, it can have an impact on the evolution of the target. In the numerical modeling of the experiment, emphasis was placed on understanding the dynamics of the target and on the role of optical pumping.

Switch Physics (Sections IX and X)

The reflex switch concept J. M. Creedon, et.al., J. Appl. Phys. 57, 1582 (1985), developed by Physics International and presently implemented at Physics International on the EYESS device² represents an important option on the path to both a higher dose "x10" Bremsstrahlung simulator and higher power PRS sources that use inductive energy storage and plasma opening switch technology. Since the Bremsstrahlung x10 machine could be constructed as an array of modules, each operating from its own switch, it is important in this case that these switches be synchronized. The reflex switch offers the advantage in principle that it can be externally triggered to achieve this overall synchronization. Like the plasma erosion opening switch, the density controlled opening switch, and the plasma filled diode, the reflex switch has hardware problems to be solved. For the reflex switch, a major problem is the need for an axial magnetic guide field, which in turn requires the use of auxillary current coils and shielding hardware. However, like the plasma-field diode, the reflex switch has the advantage that it is its own load, thus eliminating any inductance downstream of the switch.

Present reflex switches are triode devices that initially have a high impedance when the capacitor attempts to discharge its energy into the storage inductor. However, as the electron population builds up and begins to oscillate (reflex) through the center anode foil of the triode, a low impedance state is created and the switch assumes its closed state. Current then builds in the inductive store until the switch opens. Unfortunately, the time over which the switch stays closed does not scale to high current densities as its scaling behavior at low current densities suggests. Consequently, the attempt to scale the reflex switch to the x10 machine appears to be thwarted by the tendency of this switch to open too soon at current levels in excess of 1/2 megampere.

What determines the current limit at which the reflex switch behavior departs from low current scaling is not fully understood at present. Some of what we do understand is the following. As the electrons begin to oscillate (reflex) through the anode foil their population builds up around it and their energy spectrum fills out through their interaction with the foil. This allows ion current to flow more readily from the anode, the space charge fields to be altered, and the low impedance state of the triode to be set up. Thus, ion emission is one of the keys to understanding how the low impedance state develops after a few tenths of a μ sec because the ions neutralize the electron space charge and shorten the effective gap spacing of the electrodes. The ions may also play an important role in shorting out the reflex switch prematurely, which causes it to go into its open state. Ion emission is therefore one of the phenomena that we are investigating in order to determine the nature of the reflexing state and its tendency to short out at high current densities.

In addition there are two other phenomena that are also under investigation; namely ion charge exchange and electron drag from either plasma turbulence caused by the two stream instability, or by electron neutral-atom collisions in the electrode gaps.

In Section IX, a computer code NEUTRAL is described, which has been written to model protons charge-exchanging in a neutral hydrogen gas. Such a simulation is important in understanding the anomalous gap closure in a reflex switch, since it has been suggested that such a premature closure is caused by a high energy flux of neutrals traversing the anode - cathode gap. The NEUTRAL code uses Monte Carlo techniques to model the charge-exchange process and pushes particles in an applied or self-consistent electric field. Output from the code consists of neutral and ion fluxes and neutral energy profiles. The neutral flux and energy profiles are needed in finding the gap closing time. To verify that the code NEUTRAL is operating correctly, we have compared the code output with analytical results for a constant applied electric field, and we have found very good quantitative agreement. We will continue this testing until we become very confident of the code results.

Also in Section IX we discuss the electron scattering module implemented in the particle-in-cell code REFLEX. It is shown, that a benchmark case, that

a simplified version of Moliere's scattering theory is sufficient in simulating electron small angle multiple scattering.

Other work that is being carried out on the Reflex Switch is described in Section X. It seeks to determine, through an evaluation of the charge exchange neutral fluxes, the gap breakdown times and rates of impedance collapse, and to incorporate, from the particle code, estimates of turbulent drag and ion sweepout rates.

Moreover, these effects on switch performance will be tested in a circuit model to gain insight into real switch operation, and to suggest future experiments. The circuit model will operate around the experimentally observed current and voltage traces - without benefit of any free parameters.

ADVANCED CONCEPTS THEORY ANNUAL REPORT 1988

I. SCALING Z-PINCH PLASMAS WITH ATOMIC NUMBER FOR A GIVEN K-SHELL YIELD

A major goal in utilizing z-pinch plasmas as high brightness laboratory sources of x-rays is to increase the radiation emission above about 1 keV through the use of moderate atomic number ($Z = 10$ to 36) materials. Two kinds of configuration, single wires and wire arrays or foils¹⁻⁸, have been investigated in the past. Gas puffs can also be used in either geometry though only crudely since the supersonic gas flow at best approximates these shapes. In both cases, it has been observed that optimal x-ray emission decreases on a given machine as the atomic number of the z-pinch material is increased^{2,9}.

Single wire dynamics consists of a complicated interplay between electrical, MHD, ionization, and radiation phenomena. The question, therefore, of how the x-ray emission of these materials will scale with atomic number is, in principle, a difficult one. Wire arrays, on the other hand, initially have a comparatively simple dynamics (to zeroth approximation). A large fraction of the electrical energy is first converted into the kinetic energy of implosion, which is then thermalized when the array collides with itself at the axis of the pinch. In this case, a force and a circuit equation suffice to describe the optimal electrical coupling of the z-pinch load to the pulse power machine¹⁰. In this section, we will summarize how the model of Ref. 10, once modified, provides predictions of how machine and diode designs must be scaled in order to maintain a given K-shell x-ray emission as the plasma atomic number increases in z-pinch array implosions.

II. THE MODEL

Let m denote the mass per unit length of the wire array or foil and let $r(t)$ be the outside radius of the circular array as a function of time. In response to the magnetic forces that are generated when a current $I(t)$ flows through the array, it accelerates inward:

Manuscript approved February 3, 1989.

$$m \frac{d^2 r}{dt^2} = \frac{1}{2} \frac{\partial L'}{\partial r} r^2 \quad (1)$$

where L' is the array inductance per unit length¹⁰. For an array consisting of N wires

$$\frac{\partial L'}{\partial r} = - \frac{N-1}{N} \frac{\mu_0}{2\pi} \frac{1}{r} \quad (2)$$

Following Ref. 10, we will utilize the dimensionless variables,

$$x = r/r_0, \quad \tau = t/t_0, \quad i = I/I_0, \quad (3)$$

where r_0 is the initial array radius and

$$t_0 = \frac{N-1}{N} \frac{\mu_0 \ell}{2\pi R_0} \approx \frac{L_0}{R_0} \quad (4)$$

I_0 is the maximum current that flows in the load, ℓ is the length of the array load, R_0 is the diode resistance, and $L_0 = \mu_0 \ell / (2\pi)$. In terms of these variables, Eq. (1) becomes

$$\frac{d^2 x}{d\tau^2} = - A \frac{i^2}{x} \quad (5)$$

where, for large N , the dimensionless constant A is given by

$$A = \frac{\frac{1}{2}(L_0/\ell)I_0^2}{m(r_0/t_0)^2} \quad (6)$$

For a wide variety of existing pulse power machines, the current pulse is adequately described by a linear ramp $I(t) = \overset{\circ}{I}_0 t$ during the main run-in phase of the array implosion. In pulse power machines that are designed as current sources, this should also be a useful description of the current pulse. From Eq. (6), one can derive an equation for the increase of kinetic energy with implosion distance:

$$\frac{1}{2} \left(\frac{dx}{d\tau} \right)^2 = A \int_x^1 \frac{i'^2}{x} dx' . \quad (7)$$

It is clear from Eq. (7) that maximum kinetic energy is generated in the implosion if the current is large in the final stages of the run-in. Thus, on both experimental and theoretical grounds, it is useful to investigate the scaling of z-pinch implosions for linearly rising current pulses. For this case, one can define a new dimensionless quantity q by

$$q = q_0 \tau , \quad (8)$$

where

$$q_0 \equiv A^{1/4} (I_0 t_0 / I_0)^{1/2} , \quad (9)$$

so that Eq. (5) simplifies to¹¹

$$x \frac{d^2 x}{dq^2} = - q^2 . \quad (10)$$

The picture of array implosions that is provided by Eq. (10) eventually breaks down when the plasma begins to collide on itself and to thermalize the kinetic energy generated prior to this collision. Experimental evidence¹⁰ on implosion times obtained from a number of machines suggests, in fact, that Eq. (10) is generally valid until the plasma has collapsed to about 10% of its initial radius, at which time further collapse is no longer discernible and the main radiation pulse commences. Thus, the solution to Eq. (10) is of interest only up to values of $x \sim 0.1$, subject to the boundary conditions that the implosion begins at rest $dx/d\tau = 0$ when $x = 1$.

Eq. (10) can be solved either analytically by power series or numerically. The solution information of interest is the final values of q and (dx/dq) , q_f and $(dx/dq)_f$ respectively, that are achieved when x reaches its final value x_f just prior to the thermalization process.

By assuming a linear rise in current, one guarantees that the time of array implosion t_f will coincide with the time of peak current. What one needs to require, in addition, is that during the implosion, the array acquires enough kinetic energy to ignite the K-shell and contains enough

mass to produce the K-shell emission rates that are required of a high yield super-kilovolt x-ray source. In the process, one needs to determine how these requirements scale with atomic number, Z , from $Z = 10$ (neon) to $Z = 36$ (krypton). For this purpose, we used some slightly amended versions of the scaling relations that are found in Ref. 11.

For a given yield and initial array radius, one can then find expressions for the mass per length, m , the time of implosion, t_f , and the I-dot, \dot{I}_0 , as a function atomic number, Z , that are required to achieve the given yield (assuming that conventional wisdom is correct and back EMF's and plasma pressure forces will stop the 1-d implosion and begin to thermalize the kinetic energy at or around a value of $x_f \sim 0.1$ (see Ref. 10)

Graphs of m , t_f , and \dot{I}_0 that illustrate these scaling relations are shown in Figures 1-3 for two cases. In case I, we took the initial radius of the array to be 1 cm, and assumed $x_f=0.1$, so that $r_f=0.1$ cm. The desired yield was taken to be 2kJ/cm. In case II, these values were taken to be: $r_0=2$ cm, $x_f=0.07$, $r_f=0.14$ cm, and $y=15$ kJ/cm. A detailed description of how these scaling relations are derived is given in a paper that has been submitted for publication.

It is clear from Figs. 1-3 that array implosions must start at a large radius and implode to a fairly tight cylinder on axis in order to produce high K-shell yields with long implosion times and small I-dots. A good efficiency for converting kinetic energy to thermal energy is also useful in this regard. Moreover, for a given machine, with given I-dot and current capabilities, the optimum choice of element depends on the yield-per-length and spectrum requirements. It is also clear, however, that the pulse power machine must be redesigned as the load element or yield requirement is changed.

The basic idea underlying the scaling relations of Figs. 1 - 3 is that if z-pinch x-ray sources with a given yield and successively higher kilovolt energies are to be developed, then one must redesign the pulse power machine as the atomic number of the plasma is increased in order to implode the required higher plasma mass with a higher power input and a shorter implosion time (for a given plasma load geometry). It follows, conversely, that if the machine is not redesigned or reconfigured to the plasma, that one can expect the yield of K-shell x-rays to fall as the

atomic number of the plasma is increased in conformity with experimental observations.⁹ It also follows that the theoretical convenience of a linearly rising current pulse should not be strictly required experimentally, provided the required mass can be imploded to the required final kinetic energy by an appropriate circuit design.

The scaling relations contain what need to be regarded as empirical constants to be determined ultimately, either from experimental data or from 1-d hydrodynamic computer simulations of the array or foil implosion process. Simulations are needed, in particular, in order to determine (1) the thermalization efficiency, of foil implosions and (2) whether or not this efficiency itself is a scalable function of Z and/or a function of yield. We carried out some preliminary 1-d calculations for a titanium foil. They suggest that thermalization efficiencies of the magnitude used in the scaling relations of Figs. 1 - 3 do occur for a certain class of implosions. One major limitation of these calculations is that they do not describe the instability growth that is known to occur experimentally, and that undoubtedly plays a role in limiting the application of the above theory and the extent of the implosion (i.e. the size of x_f) and, thus, the thermalization efficiency. However, it should also be noted that experiments conducted to date, in which instability growth was observed and in which the implosion was limited, were generally non-optimally designed (as described by the scaling relations) for radiation production in the K-shell. Another factor that may limit the range of validity of these scaling relations is the tendency of z-pinchs to undergo radiative collapse.^{15,16} If the mass loading is sufficiently high or if instabilities form, the plasma will implode to radii much smaller than $0.1 r_0$.

Finally, important experimental evidence of non-optimum performance is frequently provided by filtered pinhole pictures of the z-pinch emission region.^{2,3} It is generally observed that as the energy of the photons increases, the size of the corresponding emission region decreases. Depending on the pulse power machine, this generally means that as Z increases, the fraction of the foil mass that participates in the K-shell emission decreases. In this sense, Z-pinch plasmas, like vacuum sparks, are remarkably accommodating. When more plasma than can be ionized to the K-shell is imploded, only an appropriate fraction, matched to the power

capabilities of the circuit, is heated to produce the K-shell emission. This experimental behavior contrasts with one of the basic assumptions of the model calculations of this paper that all of the foil mass that is accelerated inward participates in the subsequent thermalization and K-shell emission. Any experiments that are conducted to test the scaling relations proposed in this paper should carefully examine the validity of this mass participation assumption.¹⁷

References

1. D. Mosher, S. J. Stephanakis, I. M. Vitkovitsky, C. M. Dozier, L. S. Levine, and D. J. Nagel, Appl. Phys. Lett. 23, 429 (1973).
2. P.G. Burkhalter, C. M. Dozier, and D. J. Nagel, Phys. Rev. A 15, 700 (1977).
3. P. G. Burkhalter, J. Davis, J. Rauch, W. Clark, G. Dahlbacka, and R. Schneider, J. appl. Phys. 50, 705 (1979).
4. P. J. Turchi, and W. L. Baker, J. Appl. Phys. 44, 4936 (1973).
5. C. Stallings, C. K. Nielsen, and R. Schneider, Appl. Phys. Lett. 29, 404 (1976).
6. W. Clark, M. Wilkinson, J. Rauch, and J. LePage, J. Appl. Phys. 53, 1426 (1982).
7. W. Clark, M. Gersten, J. Katzenstein, J. Rauch, R. Richardson, and M. Wilkinson, J. Appl. Phys. 53, 4099 (1982).
8. S. M. Zakharov, G. V. Ivanenkov, A. A. Kolomenskii, S. A. Pikuz, and A. I. Samokhin, Fiz. Plazmy 13, 206 (Sov. J. Plasma Phys. 13, 115) (1987).
9. W. Clark, M. Gersten, D. Tanimoto, A. Kolb, J. Pearlman, J. Rauch, R. Richardson, J. Riordan, and M. Wilkinson, "Imploding Plasma Pinches Driven by High Power Generators," in Proceedings of Fifth International Conference on High Power Particle Beams 1983, University of California, San Francisco, California, (1983), p.236-241.
10. J. Katzenstein, J. Appl. Phys. 52, 676 (1981).
11. J. P. Apruzese and J. Davis, "K-shell Yield Scaling Law for Conventional PRS Loads," NRL Memorandum Report 5406 (1984).

12. M. J. Seaton, in "Atomic and Molecular Processes", ed. by D. R. Bates, Academic Press, New York, (1962), p. 374.
13. T. A. Carlson, C. W. Nestor, Jr., N. Wasserman, and J. D. McDowell, Atomic Data 2 63 (1970).
14. S. J. Stephanakis, J. P. Apruzese, P. G. Burkhalter, J. Davis, R. A. Meger, S. W. McDonald, G. Mehlman, P. F. Ottinger, and F. C. Young, Appl. Phys. Lett., 48 (13), 829 (1986).
15. J. W. Shearer, Phys. of Fluids 19, 1426 (1976).
16. V. V. Vikhrev, V. V. Ivanov, and K. N. Koshelev, Fiz. Plazmy 8, 1211 (1982). (Sov. J. Plasma Phys. 8(6), 688 (1982).)
17. M. C. Coulter, and K. G. Whitney, "Procedures for Analyzing Z-pinch X-ray Data," Bull. Amer. Phys. Soc. 33(9), paper 2W9 (1988).

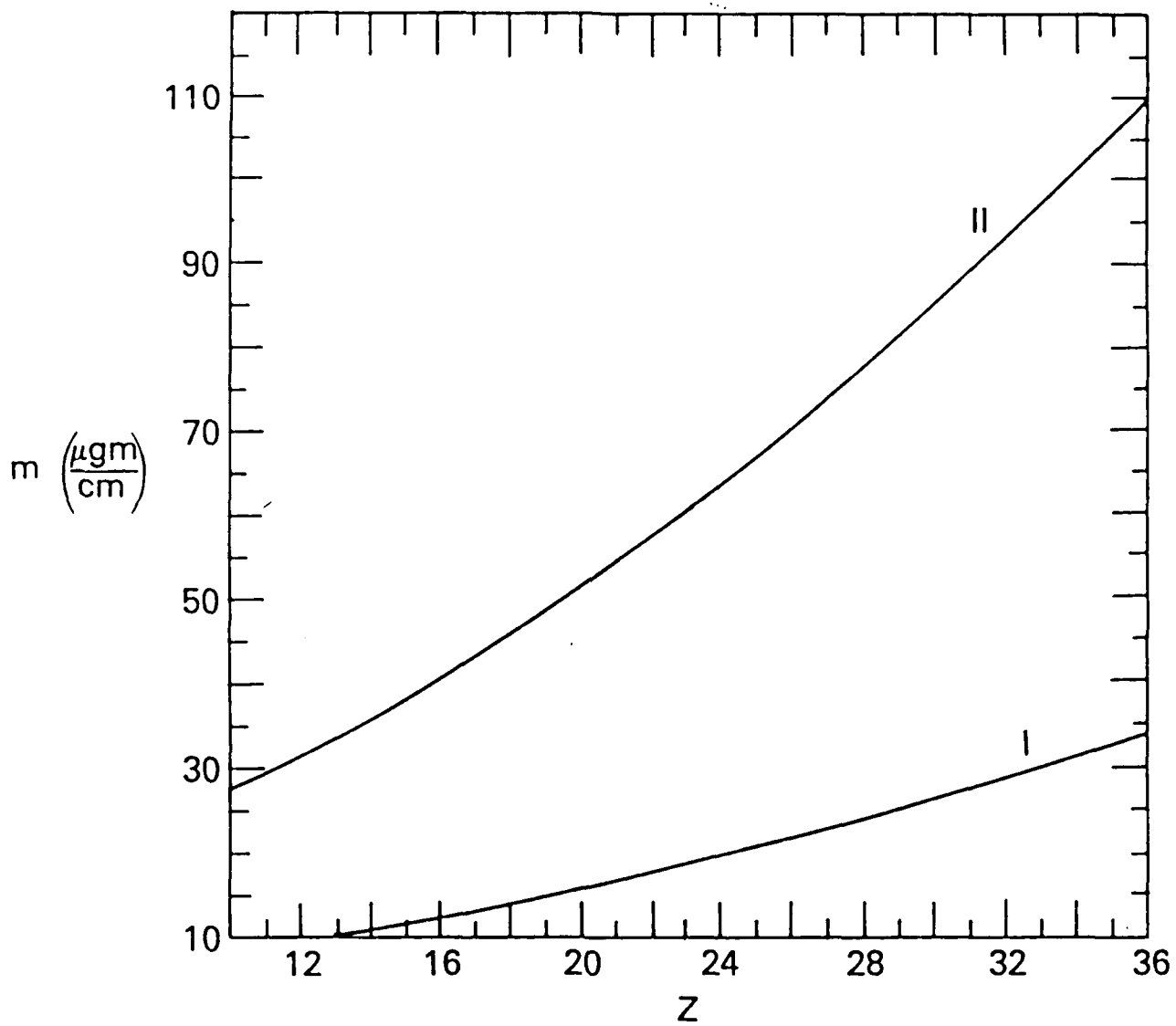


Figure 1

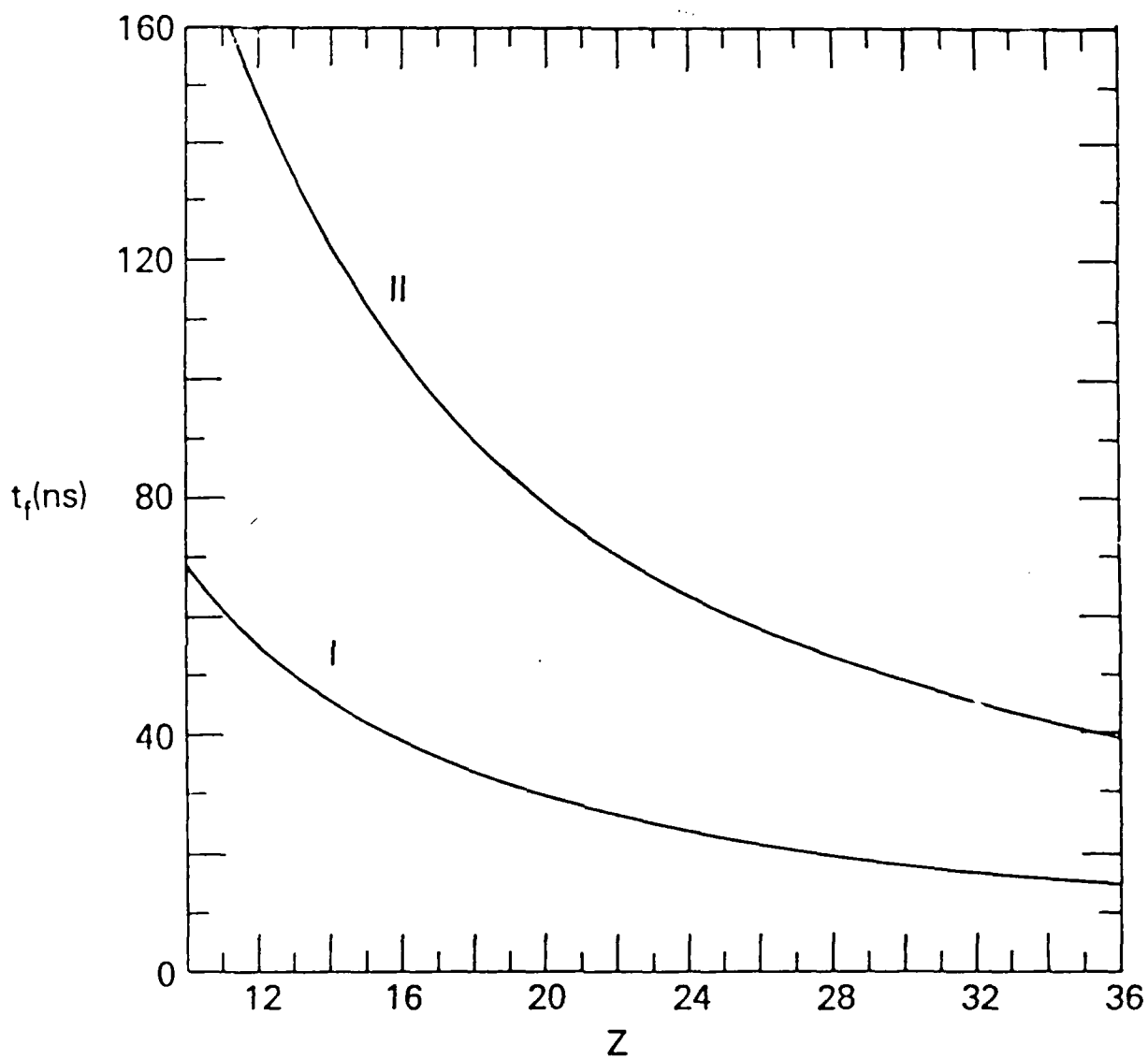


Figure 2

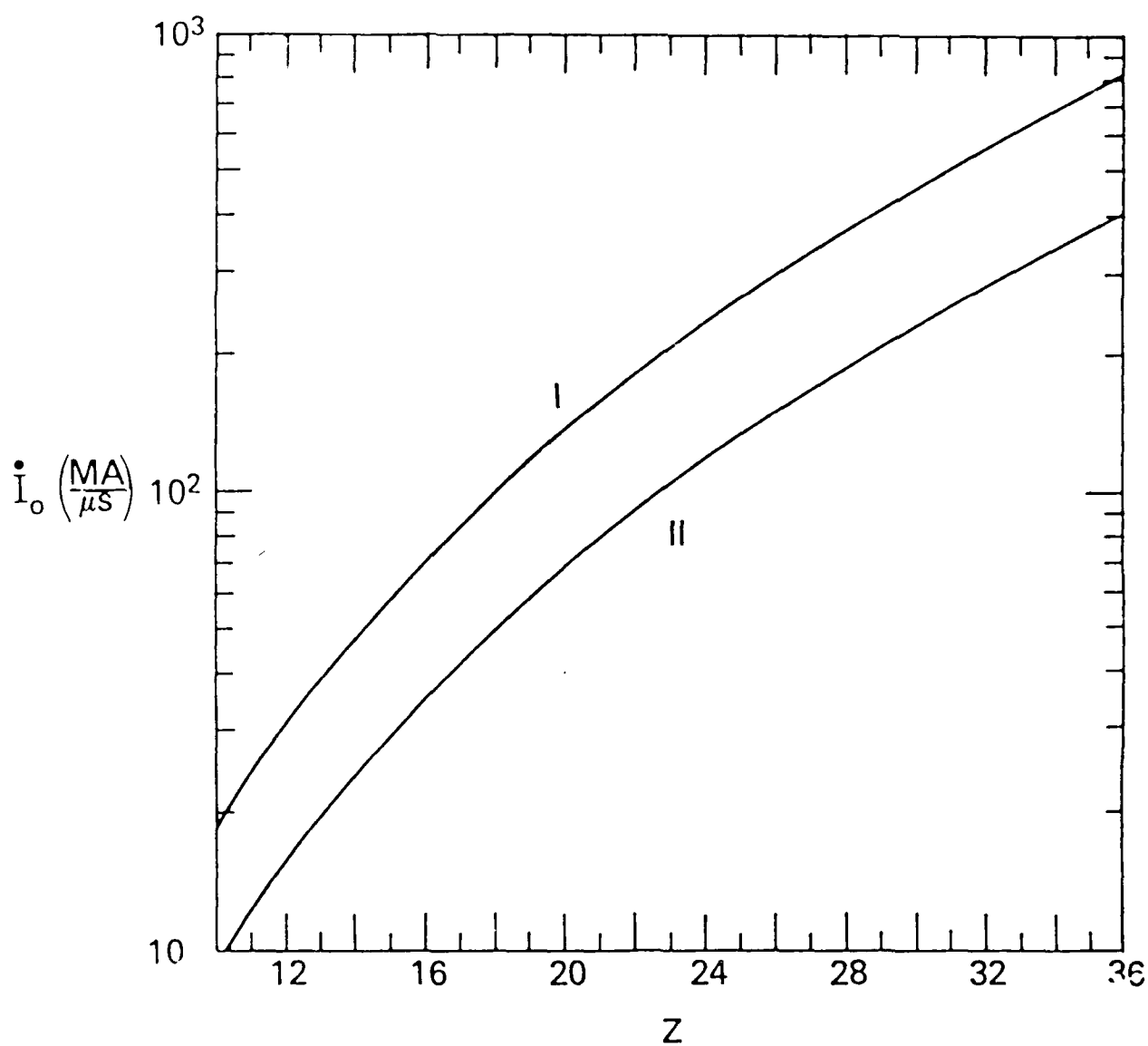


Figure 3

II. THEORETICAL AND EXPERIMENTAL COMPARISONS OF GAMBLE II ARGON GAS PUFF EXPERIMENTS

This work compares 1-D theory and experiment for a series of argon gas puff experiments that were done using the NRL Gamble II generator. We will first give a brief description of both the experimental arrangement and the 1-D theoretical model and then we compare the calculated results with experiment for: (1) K and L-shell x-ray emission and (2) energy coupling between the machine and load.

Before getting started we would like to emphasize that we do not expect the results of the 1-D simulations to agree with experiment for all cases. There is no calculation (0-D, 1-D, 2-D, or 3-D) that claims to accurately solve the plasma dynamics of a pinch at small radii, especially in the presence of instabilities and inhomogeneities. Rather, the intent of this work is to compare two key areas where the theory and experimental measurements overlap and at the same time show that there are experimental benefits to be reaped if the experimental plasmas could be made to behave in a 1-D snowplow fashion.

EXPERIMENTAL ARRANGEMENT

The experimental arrangement (Fig. 1) is as follows. A hollow cylindrical argon puff is injected across the anode-cathode gap using a high mach number nozzle. The nozzle is mounted on the center conductor. The anode is a wire mesh which provides a current path to ground through the current-return rods and which allows gas to flow away from the diode region. The voltage is measured in the water just before the ins. interface. Current in the diode is measured with a Rogowski monitor located where the current I is shown. The $(j \times B)$ force from this current drives the plasma radially inward so that the implosion occurs on axis. X-ray diagnostics view this implosion through gaps in the current-return posts as illustrated in the end view. A schematic diagram of the nozzle region is shown in Fig. 2. The return current rods are 4 cm in length and they are at a radius of 3.5 cm from the axis of the diode. The nozzle has an outside radius of 1.9 cm and an inner radius of .6 cm.

A complete summary of the experimental setup and results can be found in references 1 and 2.

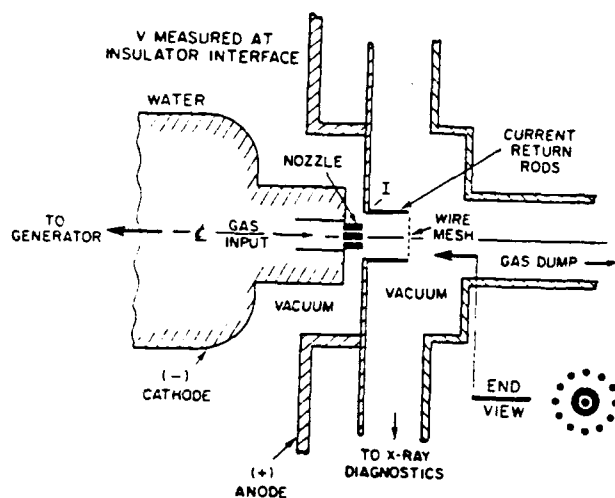


Fig. 1 - Gamble II experimental arrangement.

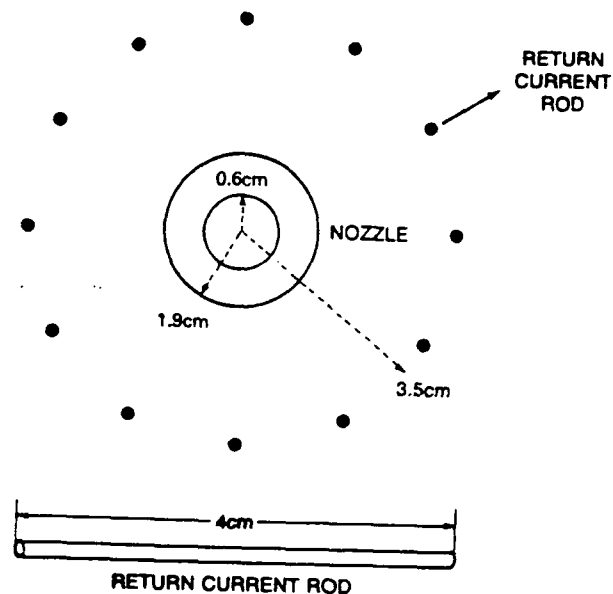


Fig. 2 - Schematic diagram of the nozzle region.

THEORETICAL MODEL

The one-dimensional model numerically solves the continuity, momentum and energy equations in a Lagrangian reference frame with cylindrical geometry (30 radial zones) and axial symmetry. It solves separately for both the ion and electron temperatures. The current density profile is calculated assuming that magnetic diffusion is a valid approximation. Once the current distribution is known, the local values for $(j \times B)$ force and ohmic heating can be calculated.

The ionization and radiation dynamics is treated self-consistently using a time dependent collisional radiative (CR) model. This model is a modified version of the collisional radiative equilibrium (CRE) models developed by the Plasma Radiation Branch at NRL³. The atomic states that provide the basis for the argon atomic physics model are all 19 ground states and 44 selected excited levels. Radiation transport is handled by a

probabilistic scheme^{4,5} which forms angle and frequency averaged escape probabilities for each line emission and recombination process.

Fig. 3 displays a typical initial radial ion density distribution of an argon gas puff that is used in the calculation. It is based on the radial pressure profiles that were measured at various axial distances from the cathode. This is the distribution that is used in the theoretical calculations. The units of the ion density are dimensionless so as to show only the relative value of the radial dependence. Note, the density out in the wings of this distribution corresponds to a background gas that is artificially added in order to insure numerical stability. Its presence does not significantly affect the numerical results.

The current I is calculated by solving a circuit equation that is appropriate for Gamble II, see Fig. 4. The impedance of the plasma load is assumed to be in series with the machine inductance and resistance. Once the current is obtained, it provides a boundary condition for the magnetic field B at the outer edge of the gas puff. The machine inductance L_0 is 58 nh and the resistance R_0 is 2 ohms. The circuit is driven by the Gamble II open circuit voltage profile V_{oc} . The voltage that is measured in the experiment is V_{meas} . $L(t)$ and $R(t)$ are the time dependent inductance and resistance of the plasma load.

The open circuit voltage profile that drives the above circuit is shown along with a calculated short circuit current profile in Fig. 5. This current profile is obtained by replacing the plasma load with a short circuit. The purpose of displaying it is to show the general shape of a typical Gamble II current profile.

RESULTS

Before describing the details of the comparisons between experiment and theory, the theoretical results need to be normalized to the experimental results. This is because the loads that are used in the experiment are measured in terms of plenum pressure, whereas in the calculation we want to measure in terms of mass per unit length. The normalization is accomplished by looking at implosion time, which is defined to be the time at which the peak in the L-shell x-ray emission occurs. Plotting this time for both the experiment and the theoretical calculation, see Fig. 6, reveals that a two to one correspondence between plenum pressure

(psi A) and mass per unit length ($\mu\text{g}/\text{cm}$) is a good approximation for this normalization. This result is also in accordance with some earlier work done at NRL⁶.

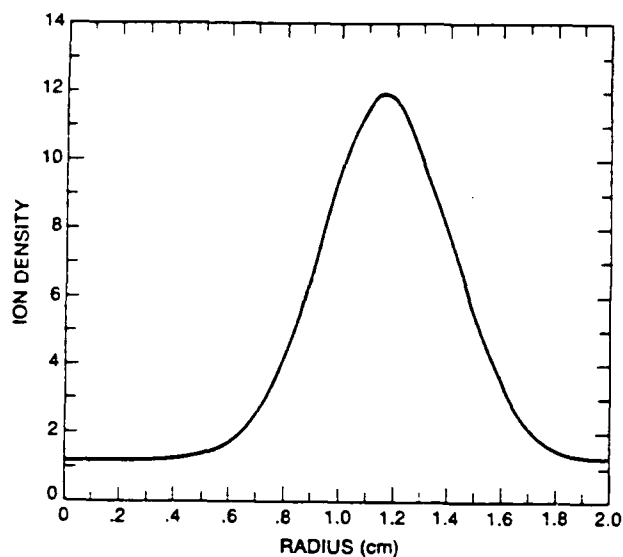
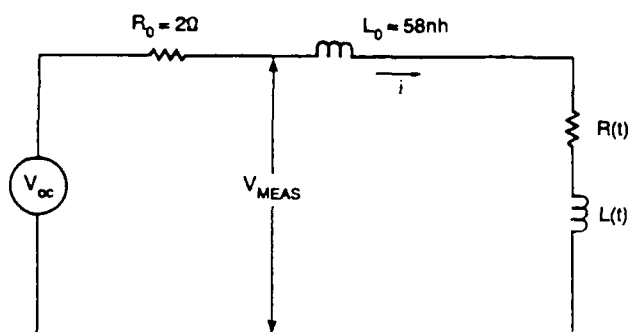


Fig. 3 - Assumed relative initial radial ion density distribution.



V_{oc} - OPEN CIRCUIT VOLTAGE
 R_0 - MACHINE RESISTANCE
 L_0 - MACHINE INDUCTANCE
 $R(t)$ - TIME DEPENDENT LOAD RESISTANCE
 $L(t)$ - TIME DEPENDENT LOAD INDUCTANCE
 V_{MEAS} - MEASURED VOLTAGE

Fig. 4 - Circuit equation used to model Gamble II circuit.

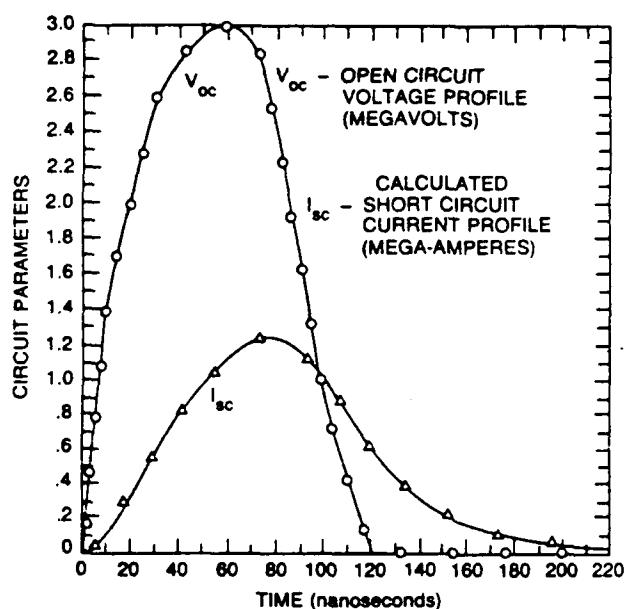


Fig. 5 - Open circuit voltage and short circuit current profile.

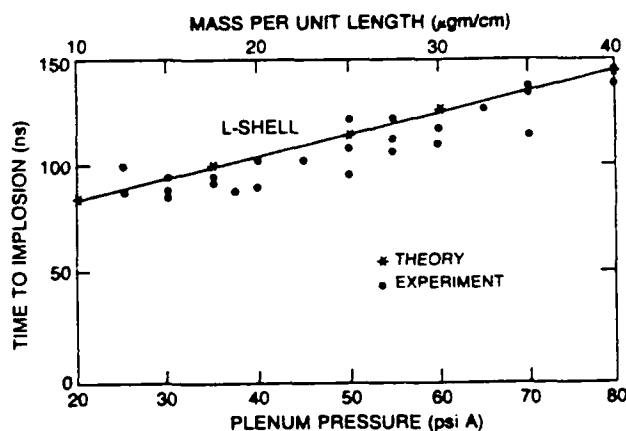


Fig. 6 - Implosion time versus mass loading and plenum pressure.

I. Comparison of L and K-shell emissions

The experiments only measured those L-shell x-rays with energies between about 250 to 460 eV (Ti filter K-edge). We find that theoretical calculations for x-ray emission in this same energy range are consistently lower than experiment (Fig. 7). One cannot be too critical of this difference because there is probably not enough atomic structure in our models to calculate the emission to better than factors of two or three for this narrow energy region. The more significant observation is that the shape of the L-shell emission curve is different in theory than experiment.

A comparison of K-shell emission (Fig. 8) shows that the theoretical implosion consistently produces more emission than the experiment does at the low mass loadings, by as much as a factor of 5 for the 18 $\mu\text{g}/\text{cm}$ load. However, the 1-D calculation and experimental measurements begin to agree at the largest mass loadings. The overall shape of the emission curves are the same and experiment and theory agree that maximum K-shell emission occur for a loading of 18 $\mu\text{g}/\text{cm}$. The fact that the two curves peak at the same load supports the idea that the K-shell emission is of a thermal origin. Since the temperature at which small amounts of K-shell emission are observed in Z-pinches is approximately given by⁷ $T = 1300 (Z/18)^2$, regions of the plasma would have had to reach temperatures in excess of 1 keV. This temperature is well within the model predictions of 150 eV for the largest mass loadings and 1600 eV for the smallest loads. It should also be mentioned that there is some experimental evidence which supports the idea that the K-shell emission is produced by non-thermal processes². The question of origin of the K-shell emission is still not resolved at this time.

II. Comparison of energy coupling

The three curves shown in Fig. 9 pertain to the machine energy that is coupled to the plasma. Experimentally the attempt to measure the amount of coupled energy is made by integrating the product of the current (I) and voltage (V_{meas}), obtained from current and voltage traces, from time $t = 0$ to time $t = \tau_{\text{end}}$, where $I(\tau_{\text{end}}) = I(0) = 0$. If all the current passes through the load, this value should physically represent the sum of the

kinetic and internal energies at time $t = \tau_{\text{end}}$ plus the total energy radiated from the plasma up until $t = \tau_{\text{end}}$. The second curve displays what the theory calculates the coupled energy to be, again assuming that all the current passes through the load, up until the time $t = \tau_{\text{end}}$. The third curve displays theoretical maximum values for the sum of internal, kinetic and radiated energies at any time during the plasma evolution. In all cases, the maximum values occurred at the time of peak implosion $t = \tau_{\text{imp}}$. The value for coupled energy is always lower at the time $t = \tau_{\text{end}}$ because the 1-D plasma does work against the magnetic field during expansion after the bounce. Some of the more massive loads implode late enough in time that there is not much magnetic field present at implosion. Therefore, their coupled energy is about the same at the end of the current pulse as it is at peak implosion. This is also partially due to the fact that the more massive loads tend to be good radiators. Thus, they radiate a significant amount of their energy away at implosion time and there is not as much energy available to do work against the magnetic field after the bounce.

A comparison between the first two curves shows that the experiment and theory are in agreement for the 40 $\mu\text{g}/\text{cm}$ loading, but, for mass loadings less than this, the agreement is poor. Even if the plasma behaves inelastically at implosion, which means that all the energy shown in curve 3 remains coupled, there are still differences of about 10 kJ of energy for the 18 $\mu\text{g}/\text{cm}$ load.

From simple 0-dimensional analysis⁸, one can show that the maximum amount of energy that can be inductively coupled to the load, in the absence of significant ohmic heating, is less than $1/2 \Delta L I_p^2$, where ΔL is the change in the inductance and I_p is the peak current. The change in inductance for a 4 cm length plasma is equal to $8 \times 10^{-9} \times \ln(R_i/R_f)$ henrys, where R_i and R_f are the initial and final radii of the pinch. Substituting the experimentally measured value for peak current, $I_p = 1.1$ mega-amperes, into the above expression for inductive energy reveals that the energy coupling is 11 kJ for a typical radial compression of $R_i/R_f = 10$. In order to couple 23 kJ of energy into the load as observed for the 18 $\mu\text{g}/\text{cm}$ load it would require a radial compression of 100 (ion densities $\sim 10^{21} \text{ cm}^{-3}$ assuming that the plasma remains axially uniform). It is not likely that such high densities are achieved, except possibly in a few isolated spots. The largest density achieved in the theoretical calculation was of the order 10^{19} cm^{-3} .

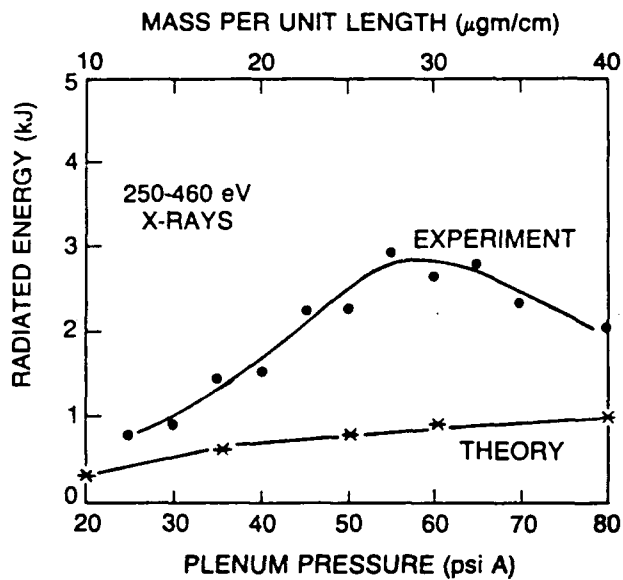


Fig. 7 - Comparison between theory and experiment for L-shell emission as a function of mass loading.

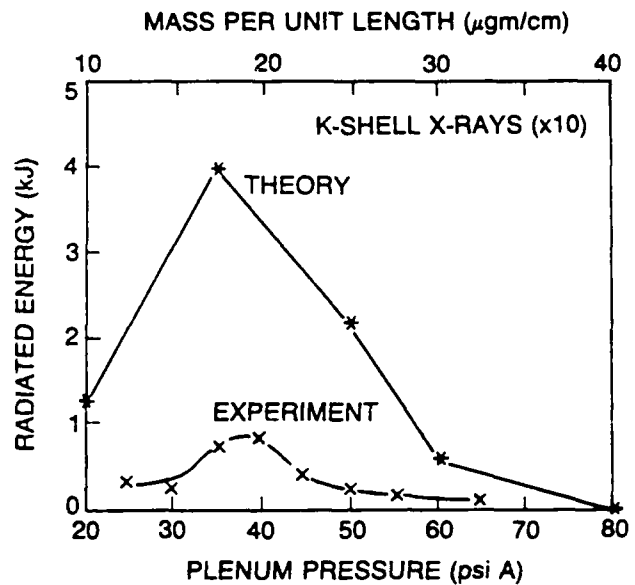


Fig. 8 - Comparison between theory and experiment for K-shell emission as a function of mass loading.

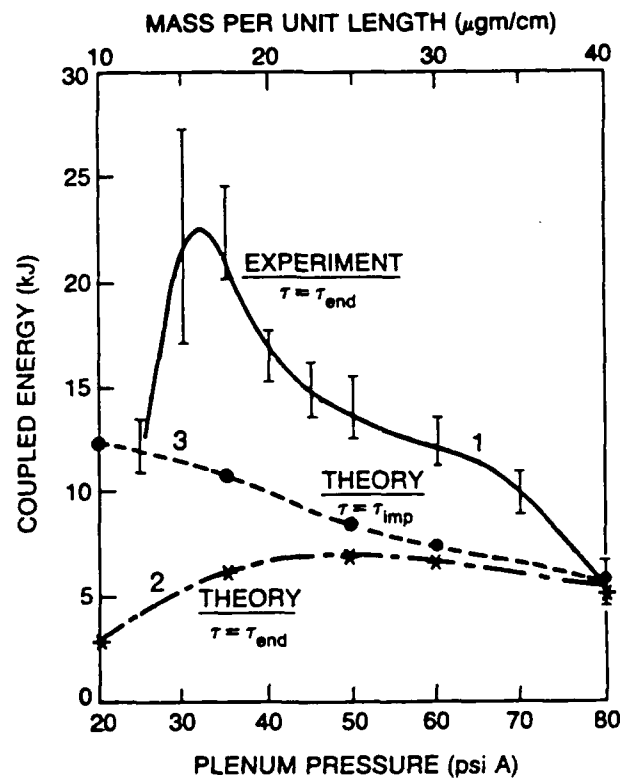


Fig. 9 - Comparison between experiment and theory for energy coupling to the load as a function of mass loading.

Note, typical theoretical values for ohmic heating (assuming Spitzer resistivity) are on the order of 5 percent of the energy coupling. The resistivity was artificially raised by a factor of 50 in one simulation to see if it would enhance the energy coupling. The net effect was that there was not any substantial increase in energy coupling. We found that the increase in ohmic heating energy made it more difficult to compress the hotter plasma. Thus, effectively lowering the inductive energy.

COMMENTS AND CONCLUSIONS

We find a number of very interesting findings from this comparison between experiment and 1-d hydrodynamic theory.

There are findings in good agreement with the experimental data:

- 1) For the larger mass experiments ($\sim 40\mu\text{g}/\text{cm}$) measured and calculated x-ray emission and energy coupling to the PRS load are in close agreement. Thus, it appears that the more massive loads are adequately modeled by 1-d calculations.
- 2) K-shell emission curves peak near the same mass loading. This is one point in favor of the possibility that the experimentally measured K-shell emission is of thermal origin.

There are findings that are not:

- 1) Theoretical K-shell emissions are a factor of 5 larger than experimentally measured for the low mass loadings. ----- This suggests that there is more thermalization of kinetic energy occurring in the 1-d calculation.
- 2) The consistently larger L-shell emissions of the experiment when viewed in conjunction with the lower experimental K-shell emission suggests that the theoretical plasmas burn through to the K-shell more rapidly. ----- Again, this implies that there is more thermalization of kinetic energy occurring in the 1-D

Note, typical theoretical values for ohmic heating (assuming Spitzer resistivity) are on the order of 5 percent of the energy coupling. The resistivity was artificially raised by a factor of 50 in one simulation to see if it would enhance the energy coupling. The net effect was that there was not any substantial increase in energy coupling. We found that the increase in ohmic heating energy made it more difficult to compress the hotter plasma. Thus, effectively lowering the inductive energy.

COMMENTS AND CONCLUSIONS

We find a number of very interesting findings from this comparison between experiment and 1-D hydrodynamic theory.

There are findings in good agreement with the experimental data:

- 1) For the larger mass experiments ($\sim 40\mu\text{g}/\text{cm}$) measured and calculated x-ray emission and energy coupling to the PRS load are in close agreement. Thus, it appears that the more massive loads are adequately modeled by 1-D calculations. If it is true that instabilities and inhomogeneities are the primary reason for deviations from 1-D theory, then this agreement can be partially explained by the fact that there is less kinetic energy and magnetic field energy available at the time of implosion to drive instabilities for the more massive loads.
- 2) K-shell emission curves peak near the same mass loading. This is one point in favor of the possibility that the experimentally measured K-shell emission is of thermal origin.

There are findings that are not in good agreement with the experimental data:

- 1) Theoretical K-shell emissions are a factor of 5 larger than experimentally measured for the low mass loadings. ----- This suggests that there is more thermalization of kinetic energy occurring in the 1-D calculation.

- 2) The consistently larger L-shell emissions of the experiment when viewed in conjunction with the lower experimental K-shell emission suggests that the theoretical plasmas burn through to the K-shell more rapidly. ----- Again, this implies that there is more thermalization of kinetic energy occurring in the 1-D calculation. However, we need to emphasize again that the atomic structure of the theoretical model limits the accuracy of the prediction of L-shell emission to factors of two or three.
- 3) Except for the largest mass loadings, the amount of energy experimentally measured to be coupled into the diode region is much larger than the theoretical value found to be coupled to the load, by as large as a factor of about 4 for the 18 $\mu\text{g}/\text{cm}$ load.

Some comments:

Perhaps the most interesting result obtained by doing this comparison is the rather large difference between theory and experiment in regards to the amount of energy coupled to the plasma load. One can argue that instabilities and inhomogeneities are responsible for this difference. If we included these mechanisms in the theory, then curve 2 should begin to look like curve 3 (Fig. 9) because the plasma would no longer behave as a perfect piston, i.e. the radially directed kinetic energy would no longer be efficiently converted into thermal energy. This in turn would drastically reduce the amount of work the plasma is capable of doing against the magnetic field as the plasma expands after the implosion. Instead, this work would remain coupled to the plasma as either internal energy or kinetic energy, not necessarily directed in the radial direction, or else it would be radiated away.

However, unless one can show that the presence of inhomogeneities and instabilities can somehow further enhance the energy coupling to the load, it is very difficult to explain the energy difference between curves 1 and 3. Regardless of the atomic or hydrodynamic models used, the energy coupling should be limited to $\approx 1/2 \Delta L I_p^2$, which is about 11 kJ for a plasma compression of $R_i/R_f \approx 10$.

References

- 1) F.C. Young, S.J. Stephanakis, and V.E. Scherrer, Rev. Sci. Instrum. 57 (8), August (1986).
- 2) P.G. Burkhalter, G. Mehlman, F.C. Young, S.J. Stephanakis, V.E. Scherrer, and D.A. Newman, Journal De Physique 47 Oct. (1986).
- 3) See references contained in D. Duston, R.W. Clark, J. Davis, and J.P. Apruzese, Phys. Rev. A 27, 1441 (1983).
- 4) J.P. Apruzese, J. Davis, D. Duston, and R.W. Clark, Phys. Rev. A 29, 246 (1984).
- 5) J.P. Apruzese, J. Davis, D. Duston, and K.G. Whitney, J. Quant. Spectrosc. Rad. Trans. 23, 479 (1980).
- 6) F.C. Young, private communication NRL.
- 7) J.P. Apruzese and J. Davis, NRL Memo. Report 5406, Aug. 31 (1984).
- 8) D. Mosher, private communication NRL.
- 9) J.D. Hares, R.E. Marrs, and R.J. Fortner, J. Phys. D. Appl. Phys., 18, 627 (1985).

III. ANALYSIS PROCEDURES FOR PLASMA RADIATION SOURCE WIRE EXPERIMENTS

Experiment - Theory Comparison

Three different plasma radiation source (PRS) load geometries using titanium wires were recently tested at Maxwell Laboratories. The goal of these experiments was to determine whether K-shell emission could be concentrated into small volume elements. In principle, concentrated energy production is needed to increase the yield in 10 kilovolt photons since it is then possible to maintain the power flow from K-shell emission below the level of the electrical power flow in a 100 TW or smaller pulse power machine. For a better understanding of how the different loads adjust their mass and current distributions to the electrical and radiative power flows in the diode, it is important to theoretically estimate and compare the plasma conditions giving rise to the K-shell emission in the different experiments. A general theoretical technique, using all of the experimentally determined properties of the plasmas, was used to determine average plasma conditions of the K-shell emission region for the three optimal (highest yield) titanium wire experiments.

The x-ray measurements made during the experiments included (1) the total yield of K-shell x-rays, (2) their pulsewidth and pulseshape, (3) pinhole camera pictures that showed the time-integrated maximum size of the emission region, and (4) K-shell spectrum data (from 4.5 to 5.75 keV for titanium). From these measurements, it is possible to estimate an average K-shell energy production rate, the time integrated radial extent of the emission region, and the relative strength of helium-like to hydrogen-like K-shell emission. Section II of NRL Memo No. 6389 describes in detail how these three values are obtained from the rough data. Using these three experimentally determined values and theoretical CRE calculations of the K-shell spectrum, one can determine the temporally and spatially averaged temperature and density of the emission region during peak compression.

From the size of the emission region and from the experimentally determined radiated-power-per-unit-length, one can calculate the dependence

of the electron temperature on ion density. One can calculate a second fit for the electron temperature versus ion density from the experimental value of the He- β to Ly- α line ratio. The intersection of these two different curves provides a unique average temperature and density. If there is experimental, or theoretical, uncertainty, one will find a range of possible temperatures and densities. Experimental uncertainty leads to upper and lower bounds on the radiated-power-per-unit-length and on the line ratios. This means that instead of having only two intersecting curves and, therefore, a unique solution, one has set of curves. Their intersection leads to a range of possible solutions. This is illustrated in Figure 1 which shows the fits obtained from the upper and lower bounds on the radiated-power-per-unit-length and the He- α to Ly- α line ratio for the optimum single titanium wire shot, shot 2022. Figures 2 and 3 compare the experimental and theoretical spectra for this same shot.

An in-depth analysis of three of the titanium shots (one for each geometry: single wire, X-pinch and wire arrays) is described in Section III of NRL Memo No. 6389. The initial conditions and the experimental data are summarized in Tables 1 and 2 respectively. The results of the analysis are summarized in Table 3. Both the single wire and the X-pinch geometries produced denser, more concentrated emission region than the wire the X-pinch K-shell emission, which is concentrated at the intersection of the wires, offers an added advantage that it can also be more readily focused and further concentrated on test objects. The single wire load on axis has the advantage that the emission region achieves the highest densities and produces the highest radiated intensities albeit in a series of tiny spots distributed along the axis. Note that single wire and X-pinch concepts are combinable in a double Y geometry to conceivably achieve some advantages of both concepts.

In addition to the three titanium PRS experiments, an earlier single wire copper experiment was analyzed. It is described in Section IV. Since no Ly- α was measured in the copper wire experiment, the temperature and density can not be pinpointed. Table 4 summarizes the results of the copper wire experiment.

Theory - Theory Experiment

As an additional verification of the above method of determining the average temperature and density reached during peak compression, we have analyzed a theoretical experiment. For the theoretical experiment, detailed hydrodynamics data was obtained from a 1D Lagrangian code with ionization dynamics calculated by a time-dependent collisional radiative model. The 1D code used to simulate the 'experimental' data is different from the 2D radiative CRE code used to analyze the data.

The advantage of using a theoretical experiment is that it provides time-dependent profiles of the ion density and electron temperature throughout the plasma. The average ion density and average electron temperature determined from the homogeneous and steady-state analysis can then be compared directly to these detailed 'experimental' time-dependent profiles. The agreement, or lack thereof, between the average values and the actual time-dependent values provides an indication of the accuracy and usefulness of the analysis technique described in Section II of NRL Memo No. 6389.

Using the 'experimental' spectrum (see Figure 4), the He- α to Ly- α line ratio was found to be around 1.9. There is some uncertainty since there is considerable overlap between the He- α and He-intercombination lines. The radiated-power-per-unit-length was found to be 2100 J/ns/cm. From the time-dependent profile of the radius, the size of the emission region was found to be around 0.1 cm. The pulsewidth (FWHM) was 2 ns.

By comparing the 'experimental' radiated-power-per-unit-length with the steady-state calculation, the average electron temperature can be determined as a function of average ion density. Furthermore, by comparing the 'experimental' and steady-state (or theoretical) line ratios, a second fit of the average electron temperature versus average ion density can be found. The intersection of these two different curves, shown in Figure 5, gives an average electron temperature and ion density which best model the 'experimental' data. As in the titanium and copper wire analyses, any uncertainty in the 'experimental' data will lead to a range of possible temperatures and densities. This is indicated in Figure 5 by additional curves flanking the two which correspond to the 'experimentally' observed values.

In this particular experiment, the best fit is with an average electron temperature around 4100 eV (somewhat uncertain since the theoretical database does not extend to large enough temperatures) and an average ion density around $3 \times 10^{19} \text{ cm}^{-3}$. Figures 6 and 7 show how the average values compare with the time-dependent values during the Z-pinch. Peak power output occurs at around 52 ns. From Figures 6 and 7, one can see that the average electron temperature and ion density obtained from the analysis agree fairly well with the actual temperatures and densities reaches during peak compression.

Conclusions

It would appear from the Maxwell experiments and from z-pinch behavior in general that there are two fundamentally different problems in PRS load design, one dealing with load coupling to the machine, the other dealing with radiation loss rates and K-shell yields. Coupling is defined in terms of the long time behavior of the pinch ($\sim 100\text{-}200 \text{ nsec}$), while yield behavior must be understood over the much shorter time scale of the x-ray bursts ($\sim 5\text{-}10 \text{ nsec}$). A large initial wire mass loading appears to be needed to achieve good machine coupling; however, only a much smaller amount of the original mass participates in the super-kilovolt x-ray conversion that occurs at later times. In the Maxwell experiments, this mass fraction varied by two orders of magnitude in the different geometries.

The use of mixed element loads would improve the diagnostic capabilities for z-pinches. By observing when spectral features from elements placed at different locations in the load turn on, one could learn more about how loads are heated, where and when the current channels are formed, and how the load is ionized in time. On the theoretical side, it is clear that a better understanding of optically thick, L- and M-shell, radiation loss rates in transient plasmas is needed to be able to calculate how a PRS load adjusts itself to the electrical power flow and to the atomic structure of the load. Then, it will be possible to derive the scaling relations that are needed to be able to channel energy into greater K-shell yields.

It should be noted that some of the assumptions that were made in this analysis will need to be investigated both theoretically and experimentally. For example, recent time resolved pinhole data taken at PI has shown that the observed time integrated emission region does in fact not emit at the same time. This is especially the case of the hot spots observed in the single wire experiments. Hence, the estimates of the radiated-power-per-unit-length that we made in this report could be much higher than we took them to be and the temperatures and densities that we inferred could be much smaller than were actually achieved in the experiments. Nevertheless, if these inferred quantities could be used to identify trends in the K- and L-shell emission behavior of z-pinches, one will learn to better design them.

TABLE 1. DESCRIPTION OF INITIAL CONDITIONS IN THE TITANIUM SHOTS

SHOT INITIAL MASS ($\mu\text{gr/cm}$)	MATERIAL OF USED	NUMBER OF WIRES	WIRE RADIUS (μm)	WIRE LENGTH (cm)
2022 - single wire 1460	96% Ti 4% V	1	101.6	2.2
2027 - wire array [*] 88	100% Ti	6	10.16	3.0
2020 - X-pinch ⁺ 2190	96% Ti 4% V	6	50.8	3.0

* on 1.5 cm array diameter

+ on 2.5 cm array diameter

TABLE 2. EXPERIMENTALLY DETERMINED PROPERTIES OF THE TITANIUM PLASMAS

SHOT $\beta/\text{Ly-}\alpha$	RADIUS (cm)	LENGTH (cm)	TIME (ns)	YIELD (Joules)	He- $\alpha/\text{Ly-}\alpha$	He-
2022 0.77	$5-7 \times 10^{-3}$	0.4	7	410	15.80	
2027 1.90	0.10	3.0	10	290	31.00	
2020 1.33	0.15	0.5	7	300	10.50	

TABLE 3. RESULTS OF THEORETICAL ANALYSIS OF THE TITANIUM SHOTS

SHOT	YIELD (J/ns/cm)	MASS FRACTION	ION DENSITY (cm ⁻³)	ELECTRON TEMPERATURE (eV)	RADIUS (cm)
2022	150	0.002	1×10^{20}	2300	0.01
2027	8	0.09	3×10^{18}	2000	0.10
2020	60	0.01	6×10^{18}	2400	0.10

TABLE 4. COMPARISON OF THE RESULTS OF THE SINGLE WIRE COPPER ANALYSIS WITH THE TITANIUM ANALYSIS.

TITANIUM MASS TEMPERATURE FRACTION	COPPER TEMPERATURE (EV)	COPPER NEON-LIKE FRACTION	TITANIUM TEMPERATURE (EV)
<u>* (29/22)²</u>			
CYLINDER:			
1.000	860	0.18	400
0.100	950	0.10	410
0.010	1130	0.03	500
0.001	1610	0.0002	900
0.15(total)	965	0.10	

* The experimental K-shell power radiated per length was estimated at the time of this early analysis assuming a 3 cm emitting length, i.e., the full length of the Z-pinch was emitting. The actual K-shell emission length, however, was closer to 0.6 cm (40 x diameter of the hot spot plasma). If we examine the effect of this difference on a cylindrical Ti plasma, we find that for an emitting to initial mass fraction of 10^{-3} , the Ti electron temperature will increase from 900 eV for a 3 cm long cylinder to 1600 eV for 0.6 cm. For a larger mass fractions, the temperature increase is less.

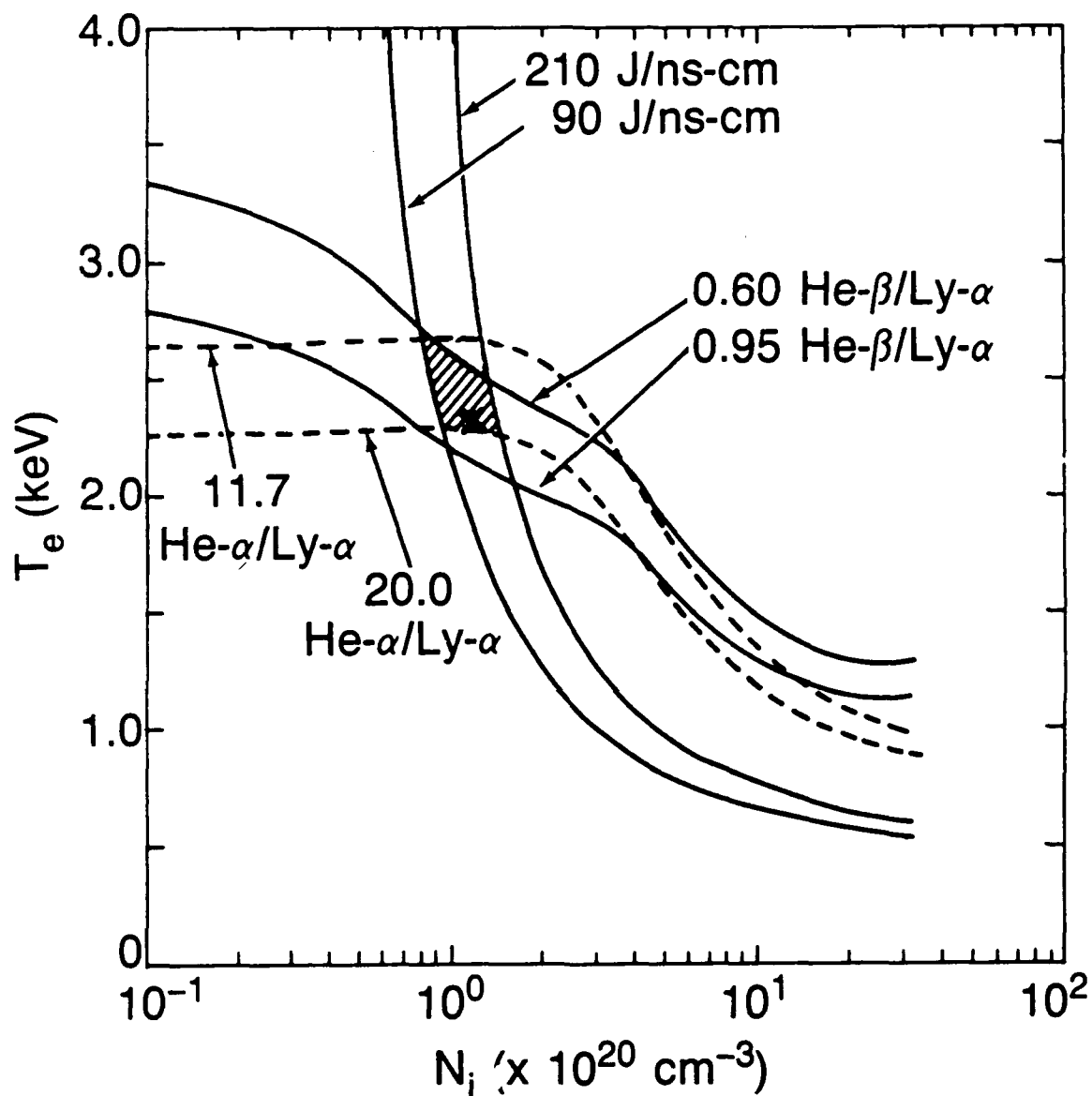


Figure 1. Range of values the radiated-power-per-centimeter and line ratios can have in the single wire shot. The intersection of the curves, shown as the shaded area, will best fit the experimentally observed values. The 'x' indicates where the observed J/ns/cm crosses the observed He- β to Ly- α line ratio. Plasma diameter is 200 μm .

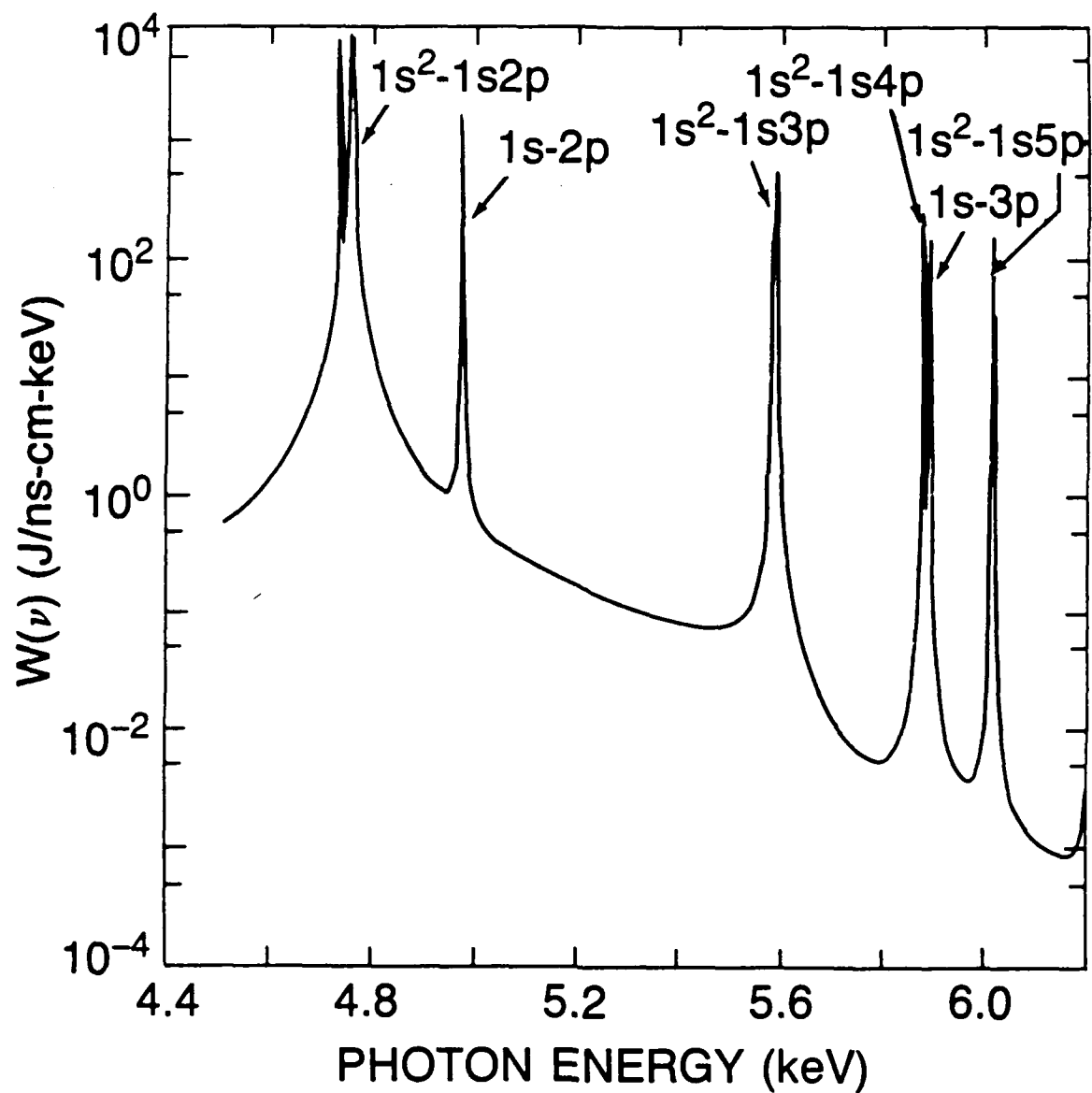


Figure 2. Theoretical spectrum for a diameter of 200 μm , ion density of 10^{20} cm^{-3} and electron temperature of 2300 eV.

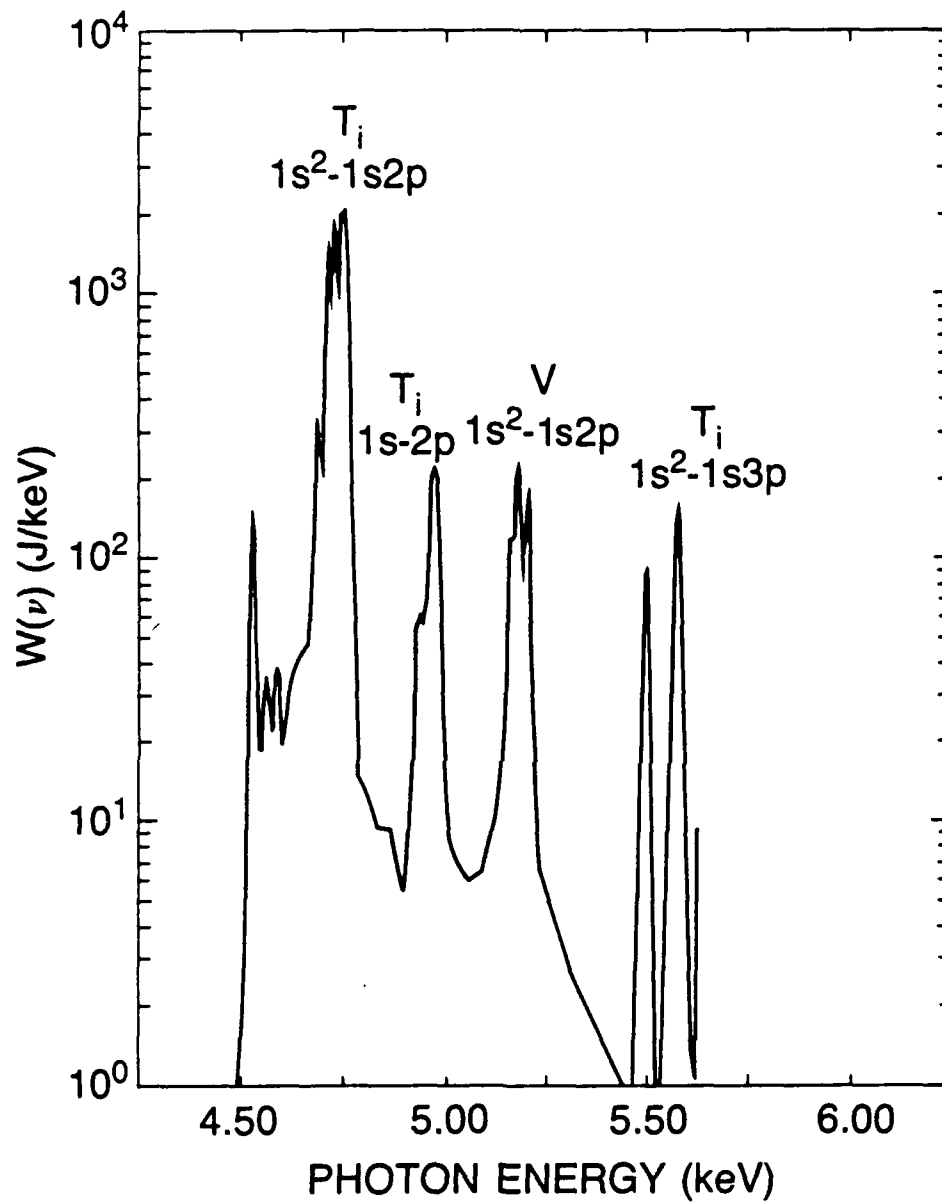


Figure 3. Experimental spectrum from the single wire shot, shot 2022.

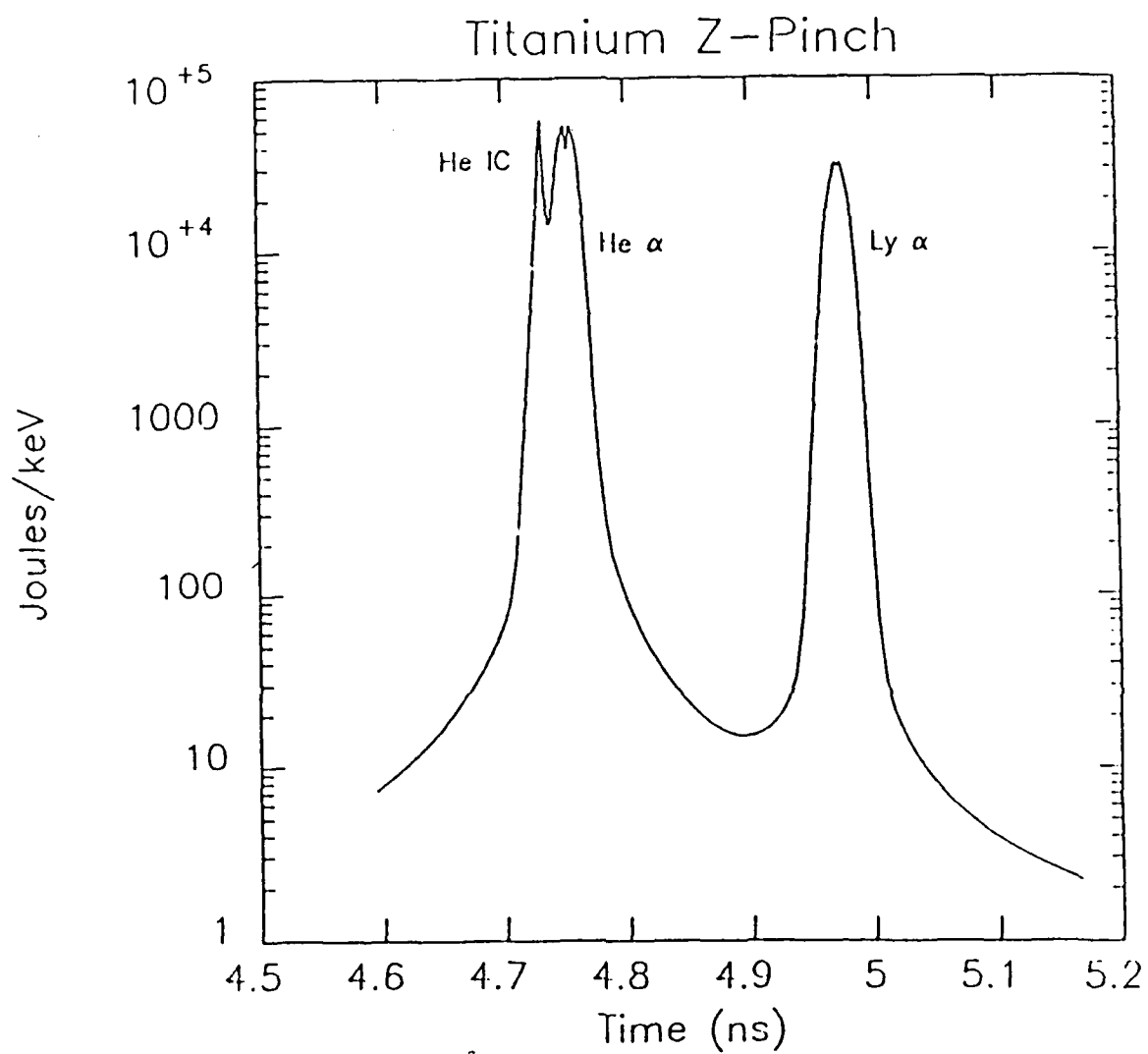


Figure 4. 'Experimental' spectrum.

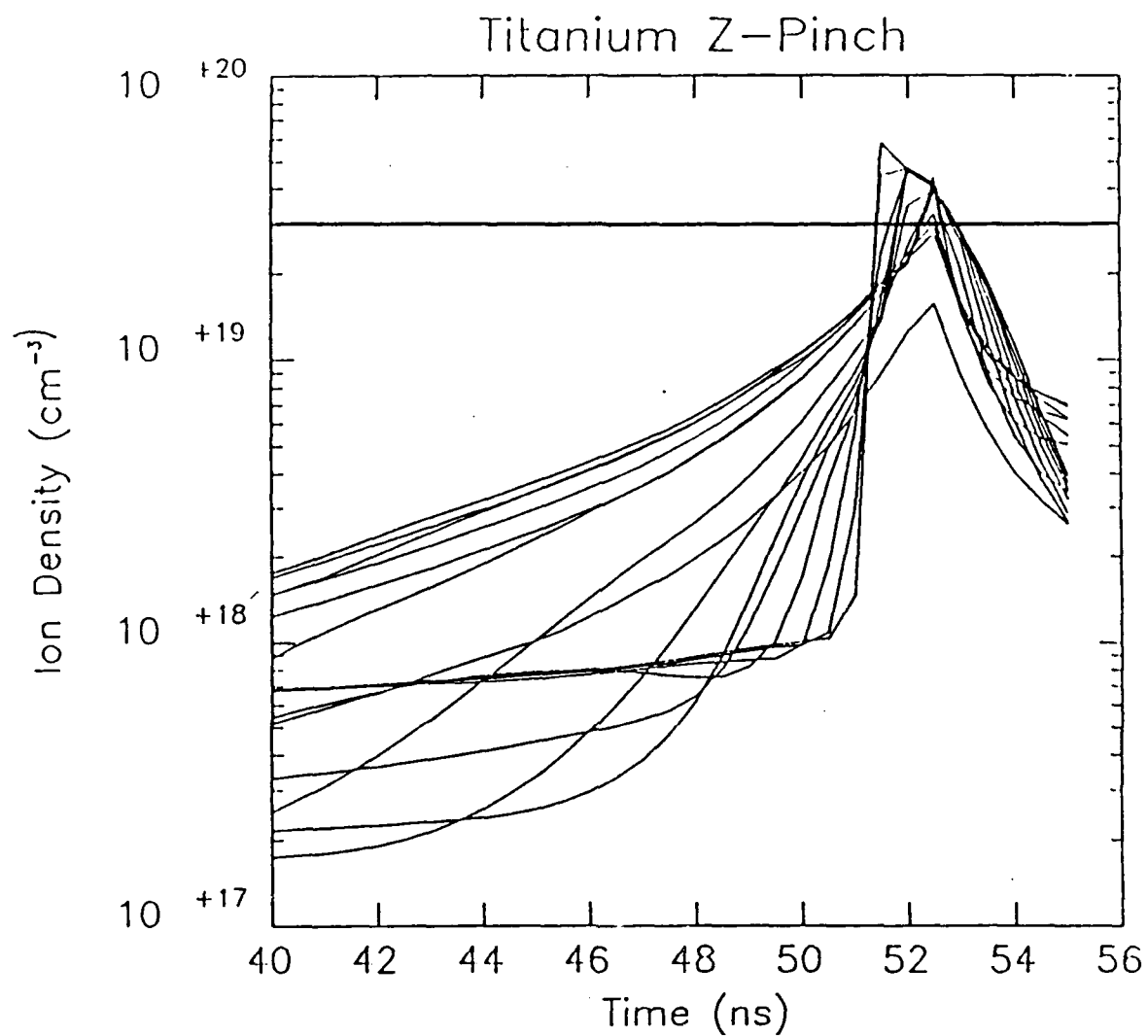


Figure 5. Contours of the logarithm of the radiated-power-per-centimeter (solid) and of the He- α line ratio (dashed) for a 0.1 cm homogeneous, steady-state cylindrical plasma.

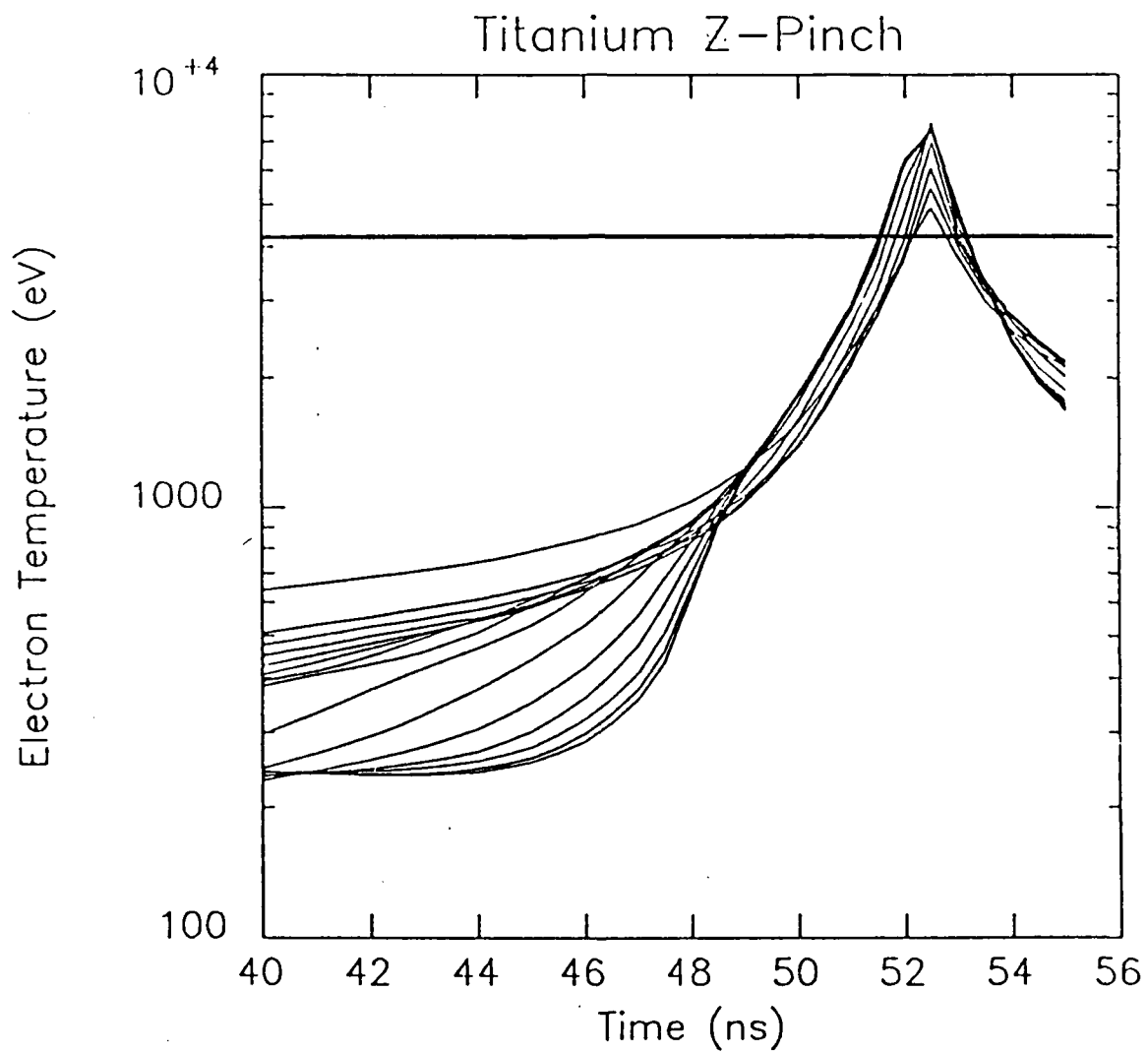


Figure 6. Comparison of the 'experimental' electron temperature as a function of time (different contours are for different zones) with the average electron temperature obtained from Figure 5.

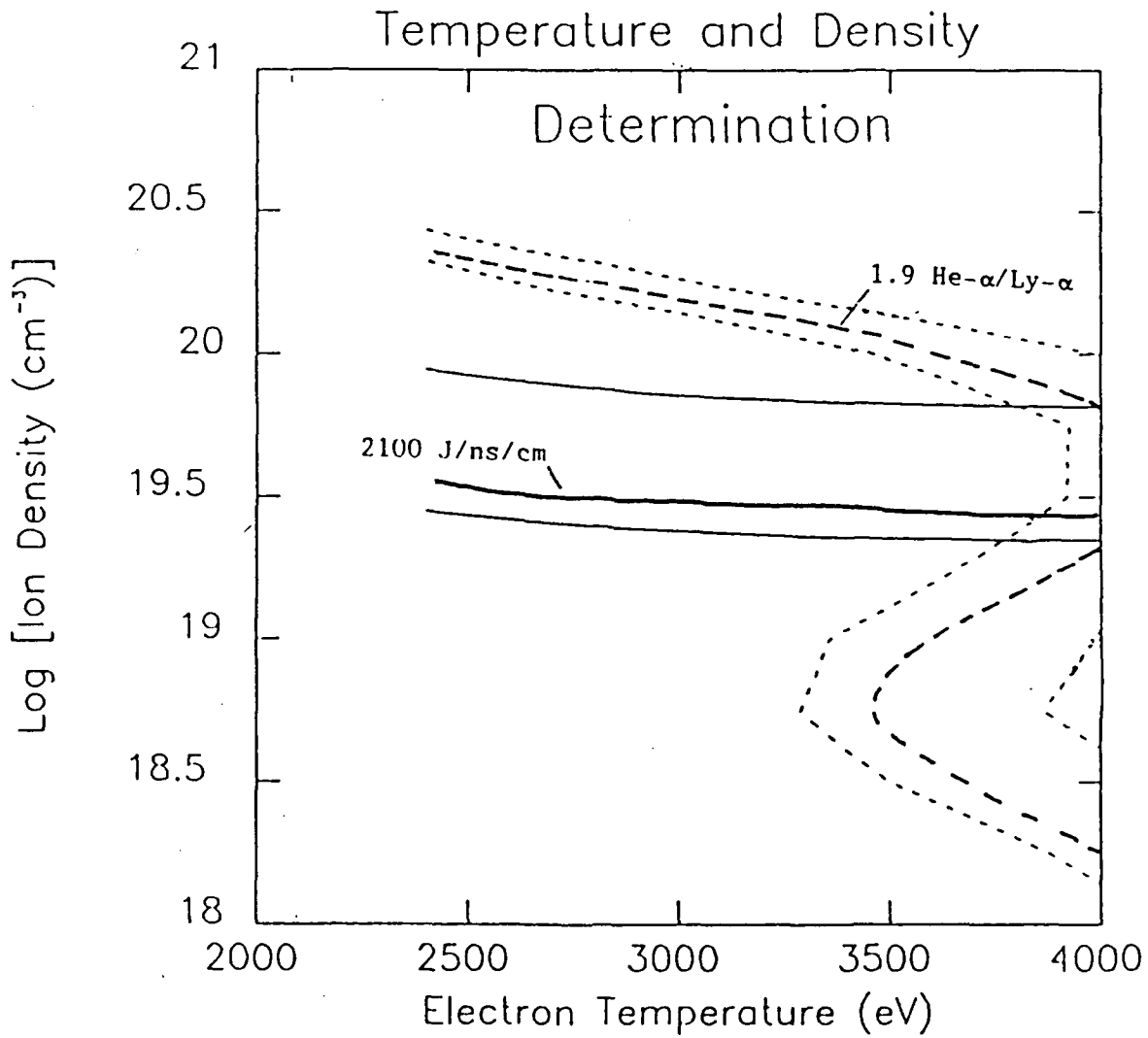


Figure 7 . Comparison of the 'experimental' ion density as a function of time (different contours are for different zones) with the average ion density obtained from Figure 5 .

IV. Electron Thermalization and Runaway Studies

PURPOSE:

In a static thermal equilibrium, particles satisfy a Maxwell-Boltzmann distribution function. There are certainly deviations from a Maxwell-Boltzmann equilibrium in a collapsing z-pinch, which affect the degree of ionization and atomic radiation rates as well as collision dynamics. Very high velocity electrons can become runaways, whose population and effects are still subject to conjecture. These could cause non-thermal behavior such as bright spots. The goal of these studies is to investigate changes in the distribution due to electric and magnetic fields, compressional heating and radiation cooling such as are present in a z-pinch implosion. An accurate model of the distribution function will:

- improve calculation of radiation losses and spectra;
- improve estimation of non-thermal phenomena like runaways;
- allow more efficient heating of plasmas, with maximization or minimization of runaways;
- improve existing MHD calculations, which assume Maxwell-Boltzmann distributions.

A previous study related to this one was a numerical investigation of equilibrium solutions to the Fokker-Planck equation for a z-pinch¹. In this earlier work, a slight depression of the distribution function tail was seen as a result of inelastic electron-ion collisions, as long as a strong magnetic field was present to constrain runaways. The present time-dependent study is a significant improvement over the earlier one because a z-pinch is far from being in equilibrium. Instead of being in equilibrium, electrons can

¹ N.R. Pereira and K.G. Whitney, Phys. Rev. A38:319 (1988)

under some circumstances experience a self-similar heating, as has already been studied with laser-heated plasmas,^{2,3} resulting in a depressed distribution function tail. Under different circumstances, the pinch can experience strong ohmic heating, which enhances the tail sharply and may result in a large number of runaways. Very important in determining the amount of ohmic heating is the magnetic field strength.

MHD DIAGNOSTICS

The solution developed here was used to post-analyze the output of a Lagrangian one-dimensional MHD z-pinch simulation.⁴ This solution can be obtained at any time, given the values of ionization Z , fields E and B , fluid velocity v_e and population fractions f_a at that time (assuming, of course, that the time variation of these quantities is sufficiently slow);⁵ here these quantities came from the MHD output. The velocity distribution function could thus be obtained at each point in space and time.

Z-Pinch Model:

The MHD code used⁴ assumed that the pinch was cylindrically symmetric, varying only in the r direction. The radial variation was given on a grid of 30 concentric cells, each of which was assumed to be spatially uniform. Within each cell, electrons have velocity components in both the r and z directions; the Fokker-Planck solution is obtained in the

² A.B. Langdon, Phys. Rev. Lett. 44:575 (1979)

³ P. Alaterre, J.-P. Matte and M. Lamoureux, Phys. Rev. A34:1578 (1986).

⁴ "TRIHYD", cf. J.W. Thornhill, J.L. Giuliani and J.P. Apruzese, Bull. Am. Phys. Soc. 33:1920 (1988)

⁵ Relaxation times were slightly faster for the Fokker-Planck solution than for the pinch, so the procedure was reasonable but did not require excessive computer time.

reference frame moving at the fluid velocity in the r direction, so only the z variation remains.

Procedure:

The procedure for using the Fokker-Planck calculation as a diagnostic was to:

- (1) Conduct a Lagrangian 1D MHD simulation of a titanium z-pinch implosion;
- (2) From this calculation, obtain time histories of the degree of ionization Z , the magnetic and electric field strengths, and the spatial dependence of the implosion velocity;
- (3) Use these quantities as input to a Fokker-Planck calculation which solves for the (nearly-isotropic) electron distribution function at each point in time; and
- (4) Calculate moments of the distribution function at each time as a check on the procedure, and estimate runaway production by calculating the conductivity.

FOKKER-PLANCK EQUATION:

There are two types of particles in the system, electrons (with density n_e) and ions (with density n_i). Typically the ions are approximately ten-times ionized ($Z_i = n_e/n_i \approx 10$). This investigation studied the electron distribution function only, assuming that the ions were in Maxwell-Boltzmann equilibrium. If there is only one axis of symmetry in the system, then the electron distribution function $f(\vec{x}, \vec{v}, t)$ can be expanded as follows:

$$f(\vec{v}, t) \approx f_0(v) + \frac{1}{v} \left[\vec{v} \cdot \vec{f}_1(v) \right]$$

With this expansion, the average value of a scalar quantity (e.g., the density) is determined by f_0 alone, while the average of a vector quantity (e.g., the current) is given by \vec{f}_1 alone.

The Fokker-Planck solution has no spatial dependence; the spatial variation of the electron distribution is inferred from the MHD results.

Inelastic electron-ion collisions, which cool the system through subsequent radiation, are included in the model. Only excitation collisions are considered; no ionization or recombination reactions, and no inverse Bremsstrahlung are included. Thus, the number of free electrons is conserved in inelastic collisions.

A collision by an electron with energy ϵ causing a transition from level a to level b has an excitation energy ϵ_{ab} and cross section given by a semi-empirical collision strength $\Omega_{ab}(\epsilon)$, of order one. The ratio of the inelastic collision frequency $\nu_{ab}^*(\epsilon)$ to the Rutherford electron-electron collision frequency $\nu_{ee}(\epsilon)$ is

$$\frac{\nu_{ab}^*}{\nu_{ee}} \approx \frac{\Omega_{ab}\epsilon}{4Z \log \Lambda} \theta(\epsilon - \epsilon_{ab}).$$

Considering that $\log \Lambda \sim 10$ and $Z \sim 10$, an effect of perhaps a few percent might be anticipated from inelastic collisions.

The Fokker-Planck equation, including terms for small-angle collisions, compressional heating or cooling, electric-field (ohmic) heating, and inelastic electron-ion collisions, can be written:

$$\frac{df_0}{dt} = C_{ee} + C_C + C_{EB} + C^*$$

where the time derivative following the fluid motion is given by

$$\frac{d}{dt} \equiv \frac{\partial}{\partial t} + \vec{v}_e \cdot \vec{\nabla};$$

elastic electron-electron collisions are described by

$$C_{ee} = \frac{4\pi Y_{ee}}{v^2} \frac{\partial}{\partial v} \left\{ f_0 \int_0^v f_0(v') v'^2 dv' + \frac{v}{3} \frac{\partial f_0}{\partial v} \left(\frac{1}{v^2} \int_0^v f_0(v') v'^4 dv' + v \int_v^\infty f_0(v') v' dv' \right) \right\};$$

the compressional term is given by

$$C_C = \vec{\nabla} \cdot \vec{v}_e \frac{v}{3} \frac{\partial f_0}{\partial v};$$

the Ohmic heating term is

$$C_{EB} = \frac{1}{3v^2} \frac{\partial}{\partial v} \left[v^2 \frac{(eE/m_e)^2}{\nu_{ei}(1 + \omega^2/\nu_{ei}^2)} \frac{\partial f_0}{\partial v} \right];$$

and the inelastic collision term is

$$C^* = \sum_j \left[-\nu_j^*(v) f_0(v) + \left(\frac{v + \delta v}{v} \right)^2 \nu_j^*(v + \delta v) f_0(v + \delta v) \right]$$

with the definitions

$$Y_{\alpha\beta} = 4\pi (Z_\alpha Z_\beta e^2 / m_e)^2 \log \Lambda,$$

m_e = electron mass,

$\log \Lambda$ = Coulomb logarithm,

$$\nu_{\alpha\beta} = \frac{Y_{\alpha\beta} n_\beta}{v_\alpha^3},$$

v_e = local electron fluid velocity,

$\omega = (eB/m_e c)$ = electron cyclotron frequency,

ν_j^* = inelastic collision frequency for process j .

ENERGY BALANCE

The Fokker-Planck term C_{ee} does not change the free electron energy in time. The rate of change of the total free-electron energy comes from the remaining terms:

$$\left(\frac{d\langle E \rangle}{d\tau} \right)_{tot} = \left(\frac{d\langle E \rangle}{d\tau} \right)_C + \left(\frac{d\langle E \rangle}{d\tau} \right)_{EB} + \left(\frac{d\langle E \rangle}{d\tau} \right)^*$$

where the compressional heating is

$$\left(\frac{d\langle E \rangle}{d\tau} \right)_C = \frac{2}{3\nu_R} \left(-\frac{\partial v_e}{\partial r} \right) \langle E \rangle,$$

ohmic heating is given by

$$\left(\frac{d\langle E \rangle}{d\tau} \right)_{EB} = 16\pi \sqrt{\frac{2}{3}} \frac{\mathcal{E}^2}{Z} \int_0^\infty \left(\frac{\epsilon}{1 + (\Omega/Z)^2 (2\epsilon/3)^3} \right)^2 f(\epsilon) d\epsilon,$$

and cooling from inelastic collisions is given by (remembering that $\nu_j(\epsilon < \epsilon_j) = 0$)

$$\left(\frac{d\langle E \rangle}{d\tau} \right)^* = -4\pi \sum_j \epsilon_j \int_0^\infty \sqrt{\epsilon} \nu_j^*(\epsilon) f_0(\epsilon) d\epsilon$$

Dimensionless parameters have been defined to characterize the electric and magnetic fields in terms of the electron thermal velocity v_{th} and the electron-electron collision frequency at the thermal velocity $\nu_R = \nu_{ee}(v_{th})$. \mathcal{E} is the ratio of the electric field with the Dreicer field, which is the critical field for runaways with no magnetic field:

$$\mathcal{E} \equiv eE/mv_{th}\nu_R.$$

The scaled magnetic field is

$$\Omega \equiv \omega/\nu_R.$$

The compressional heating term, acting alone, would cause an exponential increase (for compression) or decrease (for expansion) in the temperature.

The rate of ohmic heating in a z-pinch depends strongly on the magnetic and electric fields, and less strongly on the temperature. In the low magnetic field limit ($\Omega \ll 2Z$), ohmic heating is proportional to

$$\lim_{B \rightarrow 0} \left(\frac{d\langle E \rangle}{d\tau} \right)_{EB} \propto \frac{\mathcal{E}^2}{Z} \epsilon^3.$$

In this limit, there is strong ohmic heating, no self-similar solution, and a greatly enhanced distribution function tail. When ohmic heating is dominant (because of a large electric field, $\mathcal{E} > 1$), it results in a heating of the distribution tail. A large number of runaways are generated in this case.

In the high magnetic field limit ($\Omega > 2Z$), ohmic heating is proportional to

$$\lim_{B \rightarrow \infty} \left(\frac{d\langle E \rangle}{d\tau} \right)_{EB} \propto \frac{Z\mathcal{E}^2}{\Omega^2}.$$

In this limit, there is very little heating unless

$$\mathcal{E}^2 \gg \frac{\Omega^2}{2Z} > 2Z$$

which is much larger than the electric field needed for significant heating when $B = 0$. With a large magnetic field, the heating is more in the body of the distribution, and the tail tends to be depleted. This strong-field case resembles that of plasma heating by lasers, and there is a self-similar solution for the distribution function in this case.

The reduction in the rate of ohmic heating due to an increased magnetic field is indicated in fig. (1), which shows the rate of ohmic heating with a Maxwell-Boltzmann electron distribution, as a function of Ω .

Post-analysis results

The diagnostic output from the titanium z-pinch simulation is shown in figs. (2)-(9). As discussed earlier, the pinch region was divided into radial cells. The implosion process is shown in figs. (2) and (3), which give the positions and temperatures, respectively, at each cell as a function of time. The calculated distribution function is shown here for one illustrative cell, cell 26, which is near the outer edge. This cell develops large electric and magnetic fields (figs. (4) and (5), respectively) and as well as large currents. Ohmic heating during the course of the implosion is shown in fig. (6), and compressional heating is given in fig. (7), in arbitrary units. Cooling from inelastic collisions was negligible in this case. The total energy input to the plasma from these processes is shown in fig. (8).

The distribution function sometimes varied widely from a Maxwellian during the implosion. Figs. (9) show "snapshots" of the distribution function at different times. The solid line is the actual distribution function, while the dashed line is the ratio of the distribution function to a Maxwell-Boltzmann function at the same temperature. Note that when the ohmic heating is at a maximum (around 19 ns) the tail of the distribution function is very much enhanced, but as the magnetic field increases, ohmic heating both decreases rapidly and changes character, so that by 45 ns it is the bulk of the distribution which is heated, and the tail is in fact depleted.

Runaway electrons should be maximized when the distribution tail is enhanced, and so the number of runaways should be a sensitive function of the magnetic field strength. Based on these results, a large number of runaways would be expected prior to the "bounce" point of the implosion; at the peak density, there should be few new runaways.

Self-similar Solutions

Langdon² found a self-similar solution for the electron distribution function in laser-heated plasmas when only ohmic heating applied ($C_{ee} = C_C = C'' = 0$). The same ohmic heating term is found in z-pinch plasmas as in laser-heated plasmas, but the self-similar solution applies only when both magnetic field and electric field are large. Though it occurs, this is an unusual parameter regime for a z-pinch. It is a much more common situation with laser-heated plasmas, where the laser frequency and intensity are both very high. The self-similar solution is of the form:

$$f_{SS}(\epsilon, t) = \frac{a}{y(t)^{3/2}} e^{(-\epsilon/y(t))^{m/2}}.$$

where $m = 5$ for Langdon's case, when laser heating is the only significant factor determining the evolution of the distribution. Since the ohmic heating term C_{EB} has the same form for the z-pinch as for laser heating, this solution can apply to z-pinch plasmas. When the C_{ee} term describing elastic collisions is included, Alaterre et. al.³ used numerical simulations to find:

$$m(\alpha) = 2 + \frac{3}{1 + 1.66/\alpha^{0.724}}$$

where $\alpha = Z\mathcal{E}^2$ gives the relative strength of the ohmic heating to the elastic scattering terms. Note that the Maxwell-Boltzmann distribution is the special case with $\alpha = 0$, $m = 2$ and y independent of time. The self-similar solution with $m > 2$ has a depressed tail compared to the Maxwell-Boltzmann function. Small-angle collisions tend to repopulate the tail, which is why m becomes smaller as the elastic collision term becomes more important.

The compressional term C_C also has self-similar solutions of the same form as f_{SS} ; the inelastic collision term does not seem at this time to have self-similar solutions. Further investigation of the behavior of self-similar solutions in the presence of these terms would be very useful.

The normalization and kinetic energy integrals determine

$$a = \frac{m}{8\pi\Gamma(3/m)}$$

$$y = \frac{3}{2}kT \frac{\Gamma(3/m)}{\Gamma(5/m)}$$

For the $m = 5$ case only, the Fokker-Planck equation can be solved for the time-dependence of y , which is the heating rate:

$$y(t) = 3.503 \left[\frac{Z\mathcal{E}^2}{\Omega^2} t \right]^{2/5}$$

CONCLUSIONS

- A numerical solution has been obtained to the time-dependent Fokker-Planck equation for the first-order Cartesian tensor expansion of the distribution function. It includes ohmic heating, compressional heating and inelastic cooling. Generated solutions agree with known results in special cases such as collisional equilibrium and strong ohmic heating.

- The equivalence between ohmic heating in a z-pinch and laser heating in an underdense plasma has been established. Thus, results for the latter case can be adapted to the different parameter regime of the former. In particular, a self-similar solution for the laser-heated distribution function will apply in some cases to the z-pinch.

- Ohmic heating can significantly affect the shape of the distribution function. It can greatly elevate the tail of the distribution under small magnetic field, and can decrease the distribution tail under large magnetic fields and high electric fields.

- When ohmic heating dominates at large magnetic field, a self-similar non-Maxwellian solution exists for the distribution function, which maintains its shape while absorbing energy.

- The Fokker-Planck code developed here has been used as a diagnostic to determine actual electron distributions at various positions and times during a titanium z-pinch implosion.

- For the case under study, compressional heating was significant in magnitude, but is not as important in producing non-Maxwellian distributions as ohmic heating was.

- Conditions for the self-similar solution did not occur in the z-pinch implosion under study.

- In the z-pinch implosion studied, significant production of runaways for the implosions studied is predicted well *before* the peak compression. At the peak compression of this implosion, generation of runaways is negligible.

FUTURE RESEARCH

- Further investigate behavior of compressional term C_C .
- Use solution as diagnostic for other z-pinch implosion codes, and for other materials
- Look for self-similar solutions in other parameter ranges
- Do quantitative calculations of runaway production

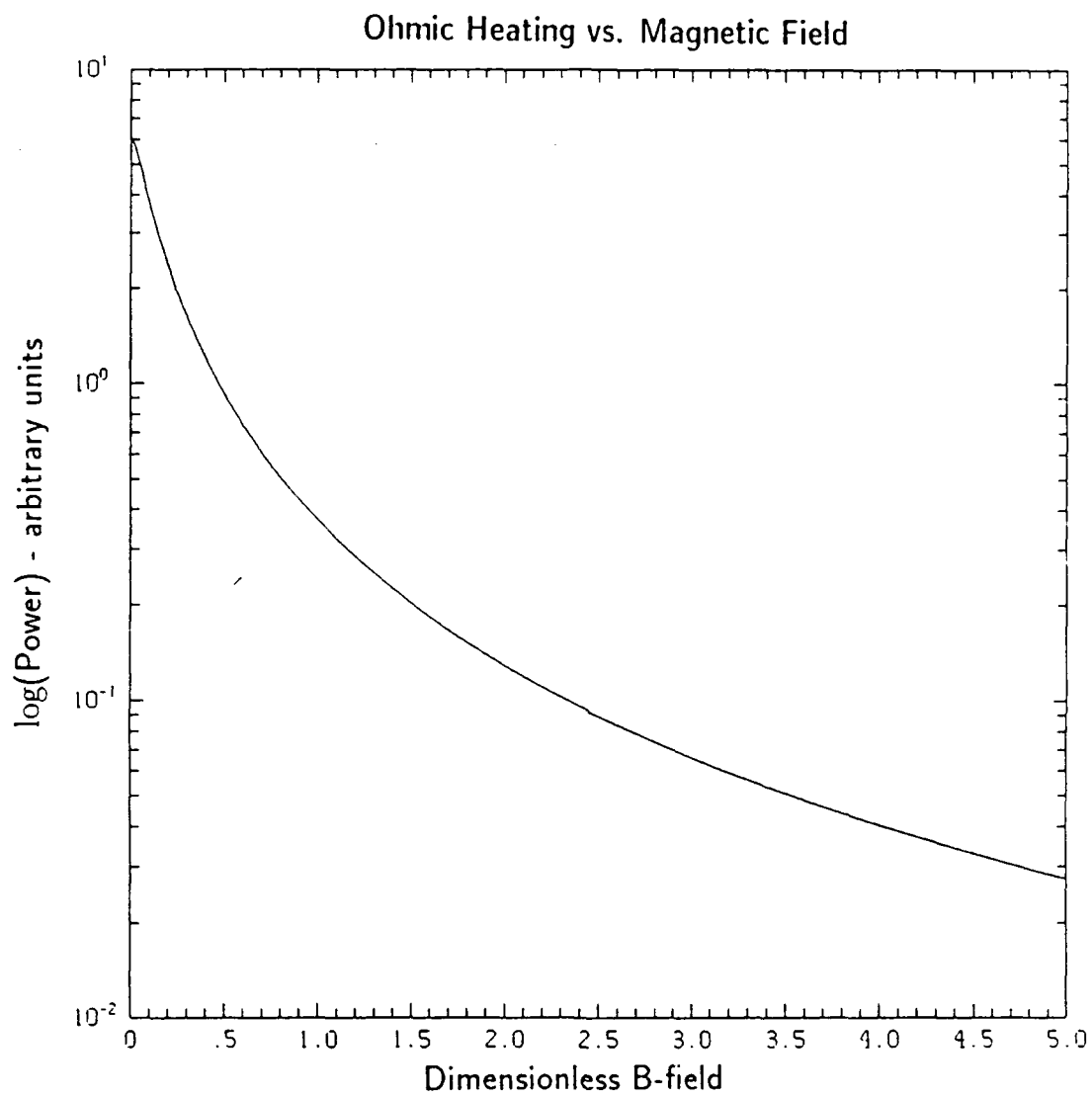


Figure 1

CELL RADII VS TIME

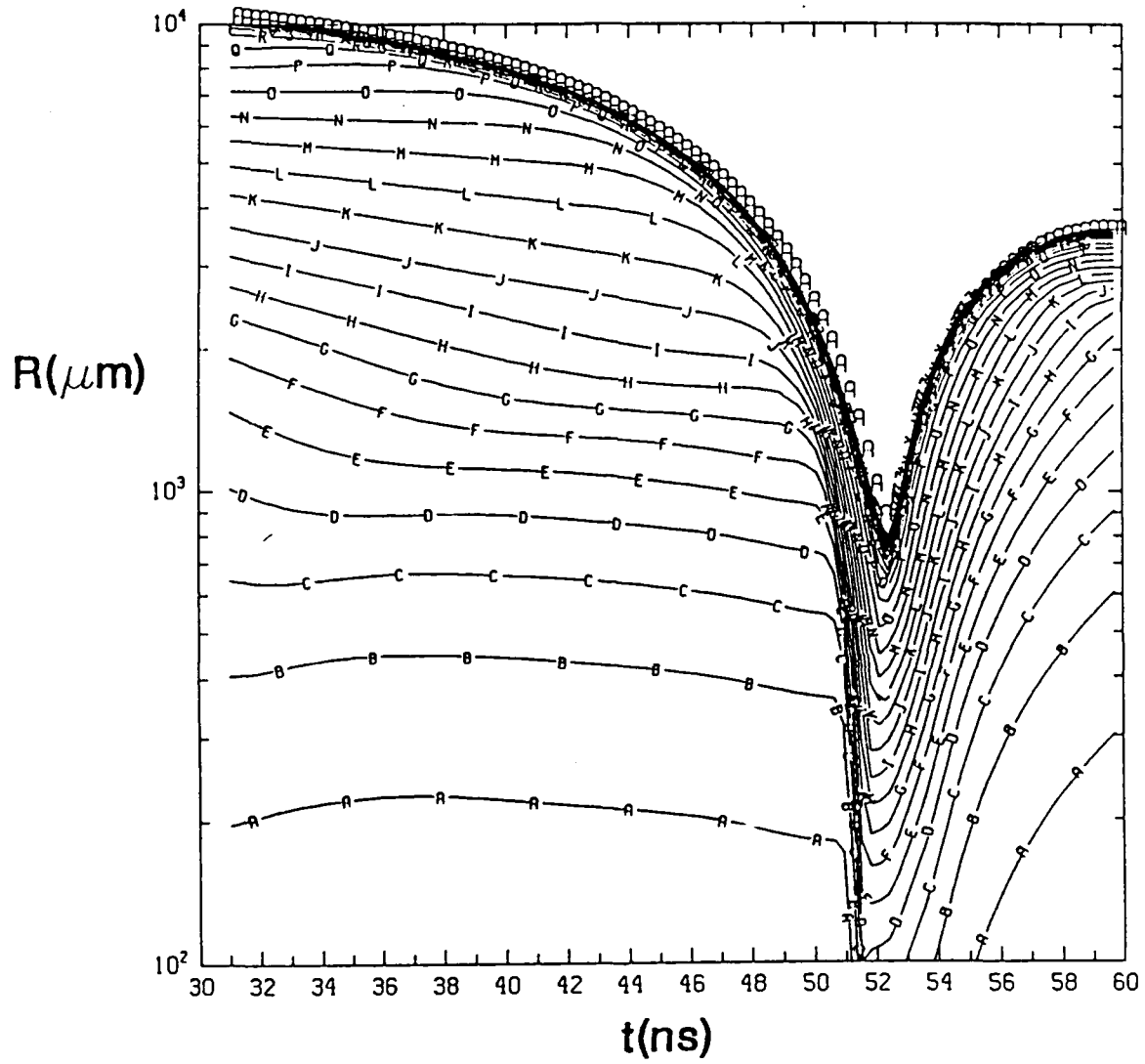


Figure 2

CELL TEMPERATURES VS TIME

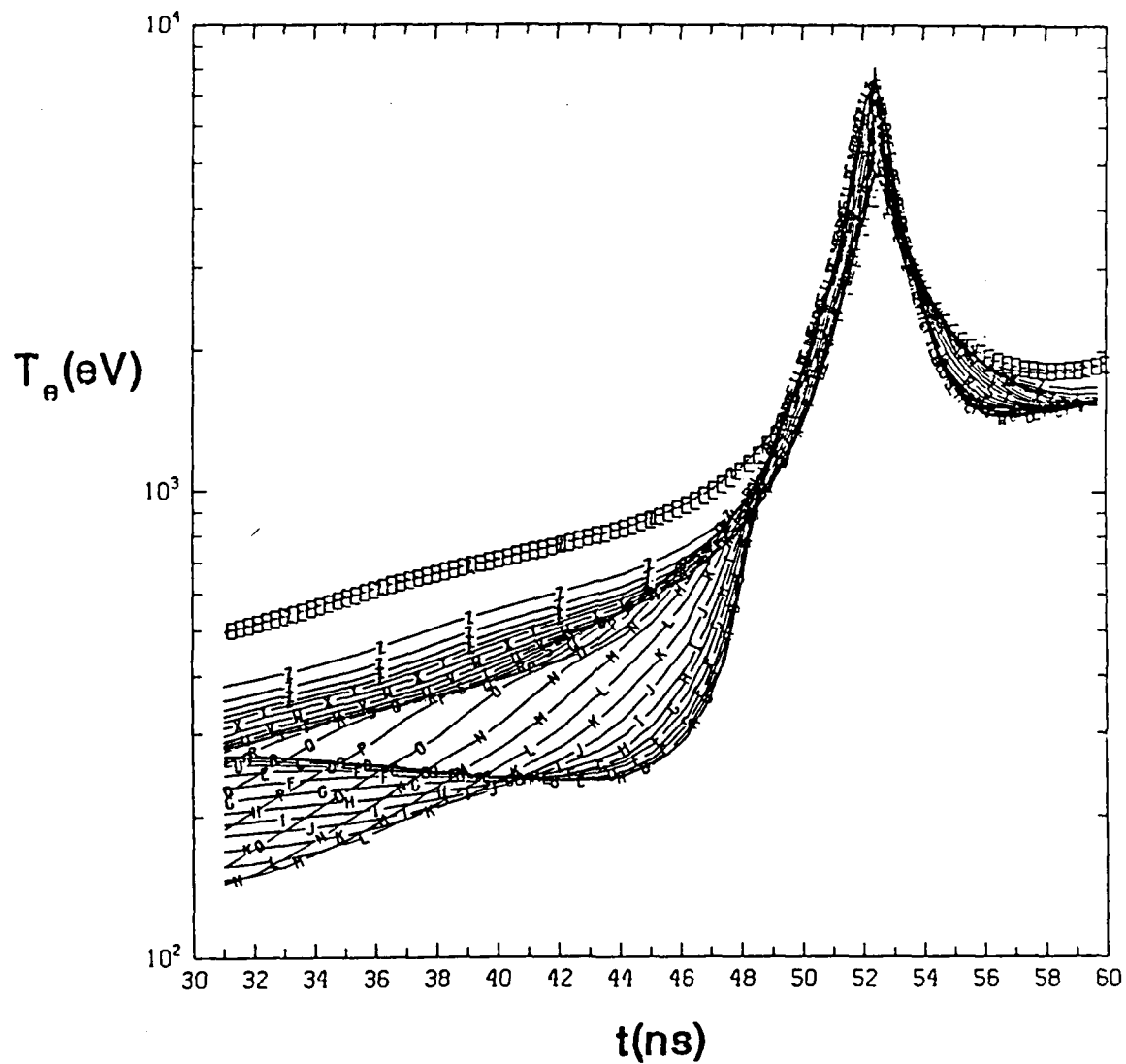


Figure 3

MAGNETIC FIELD - Cell 26

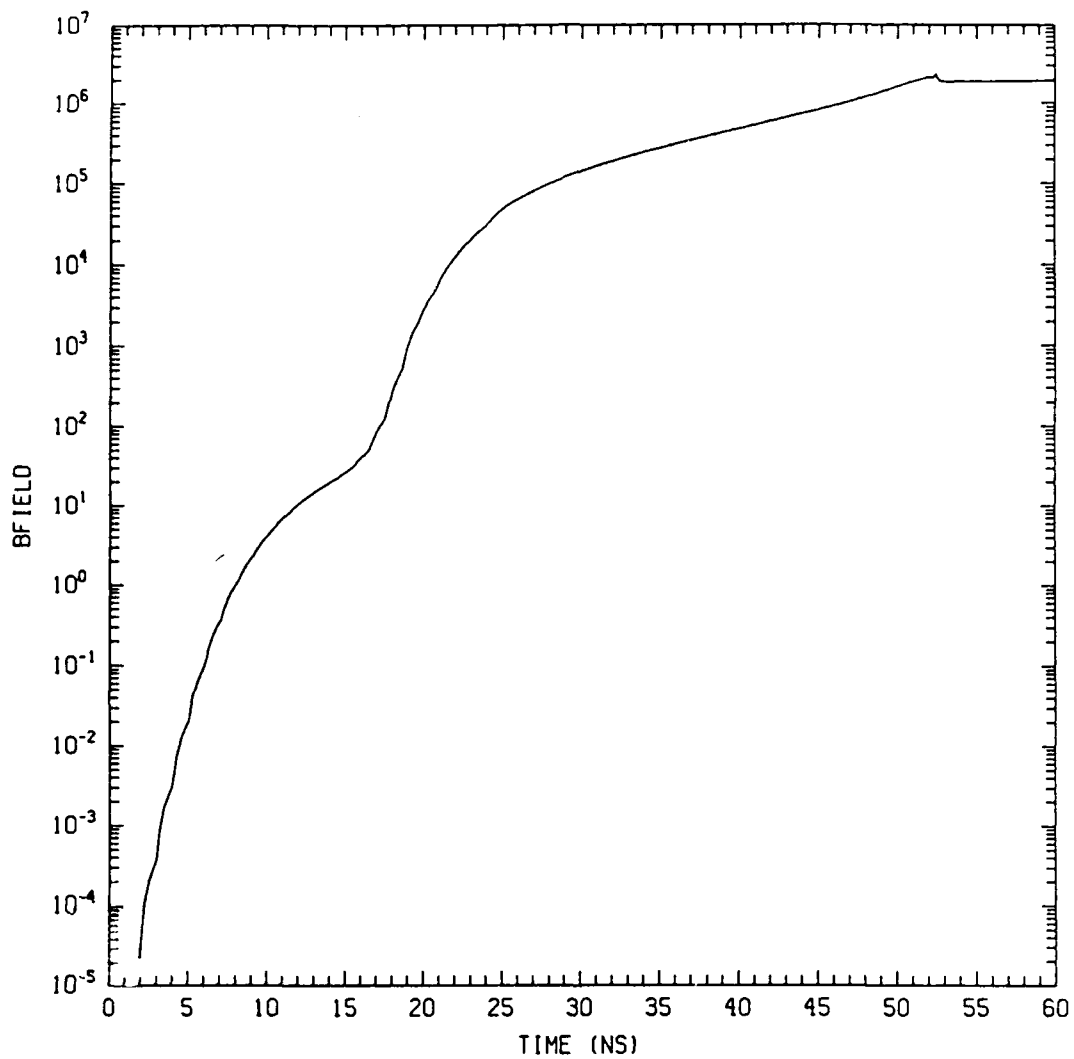


Figure 4

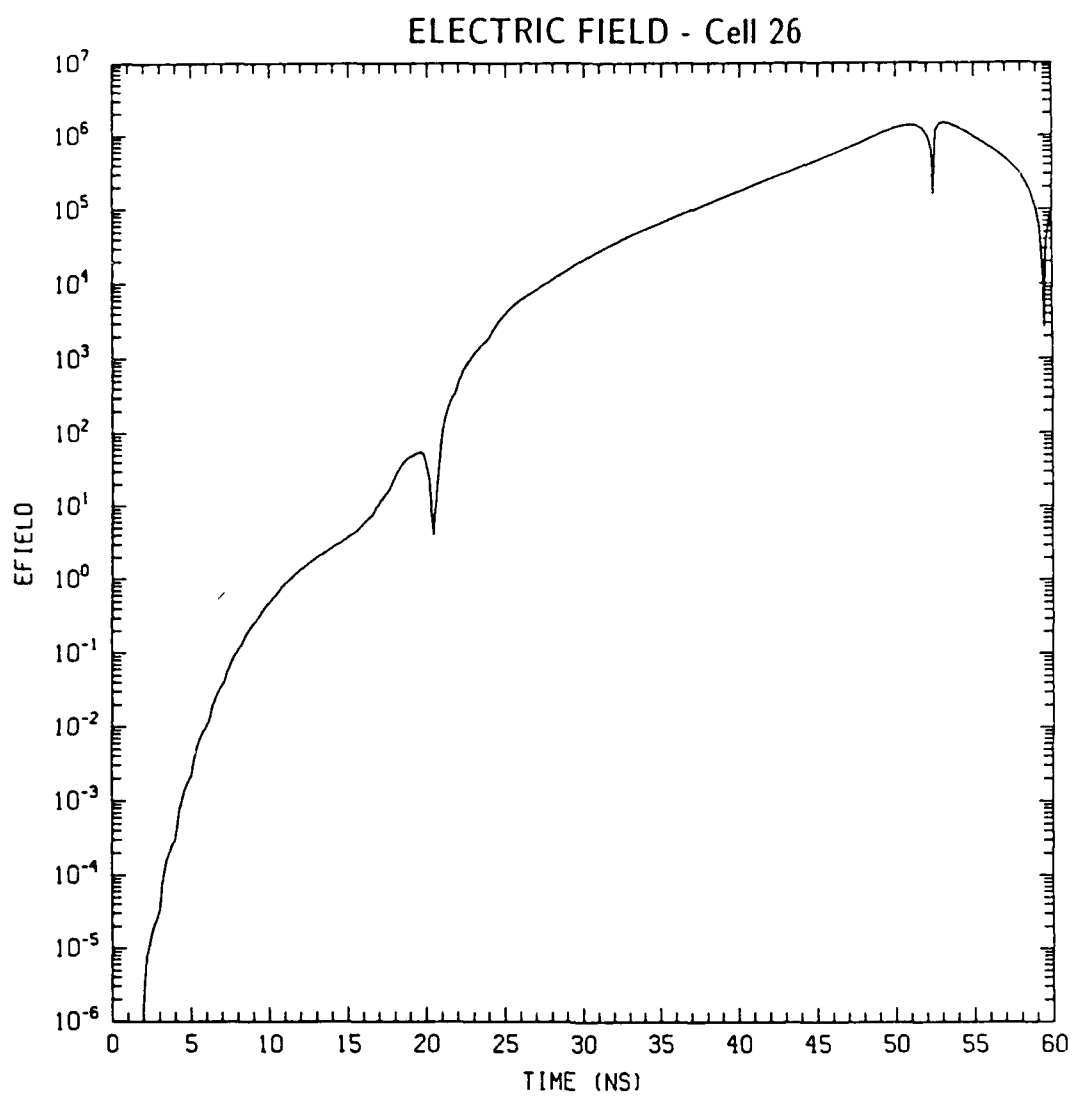


Figure 5

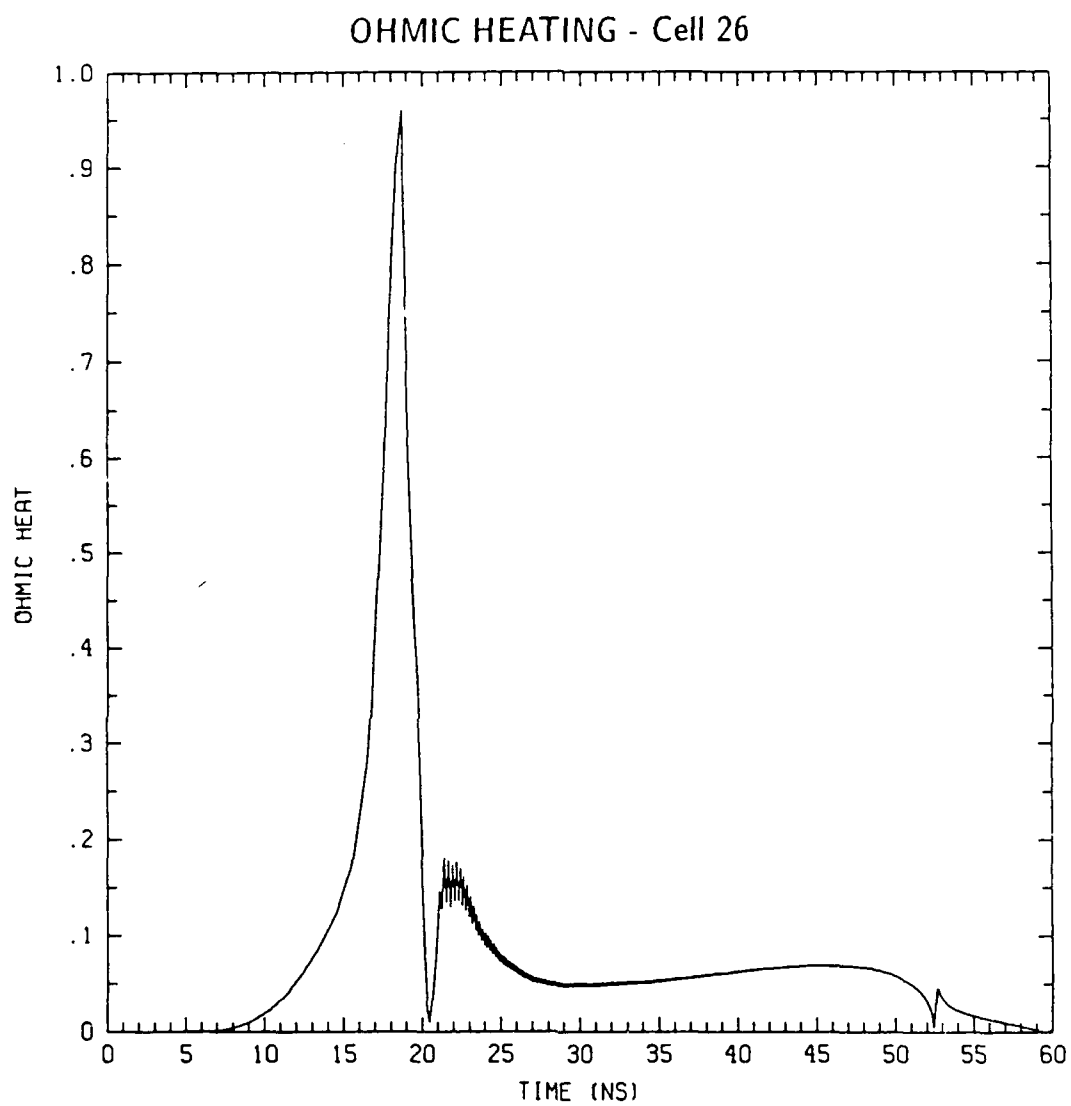


Figure 6

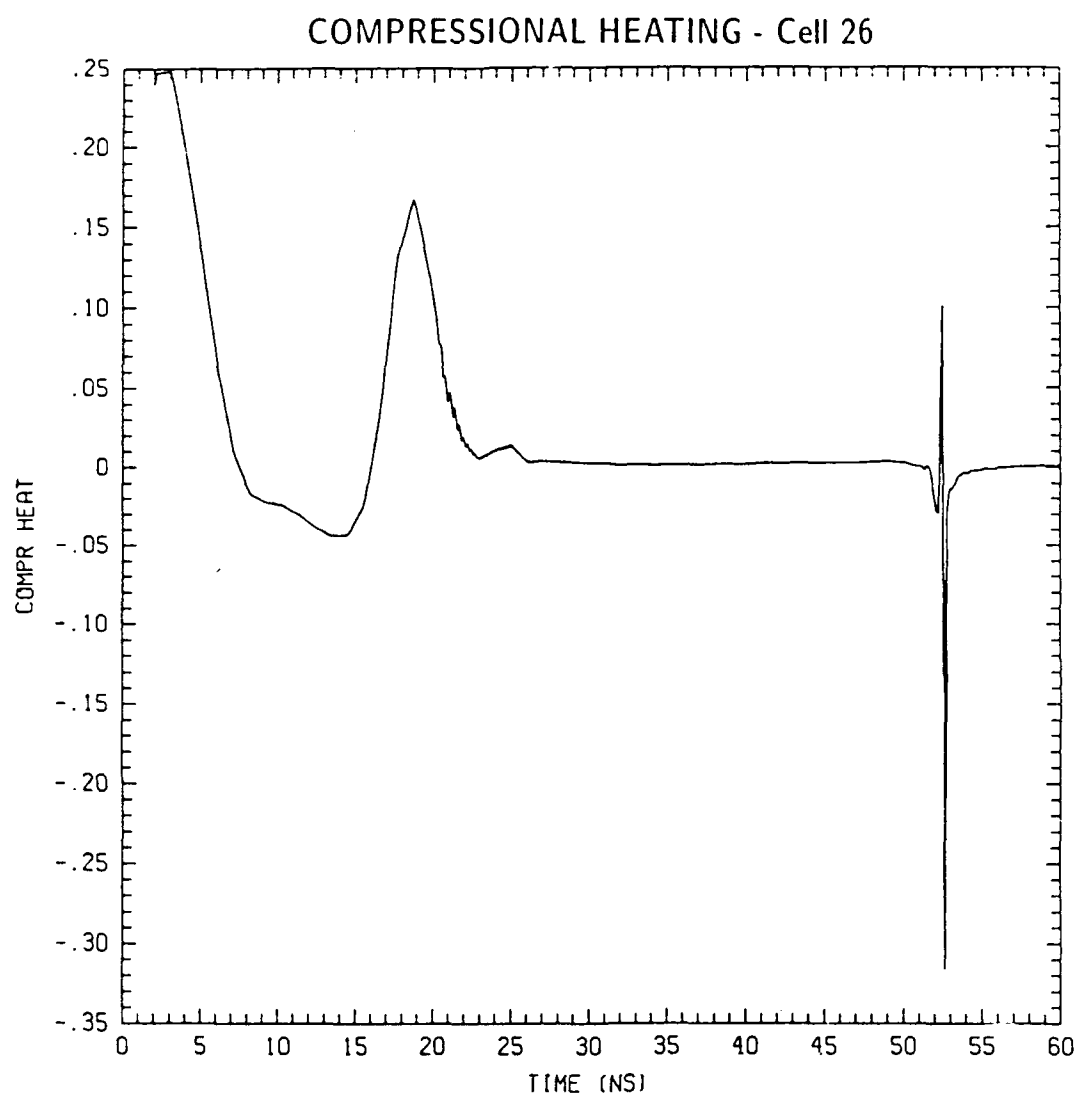


Figure 7

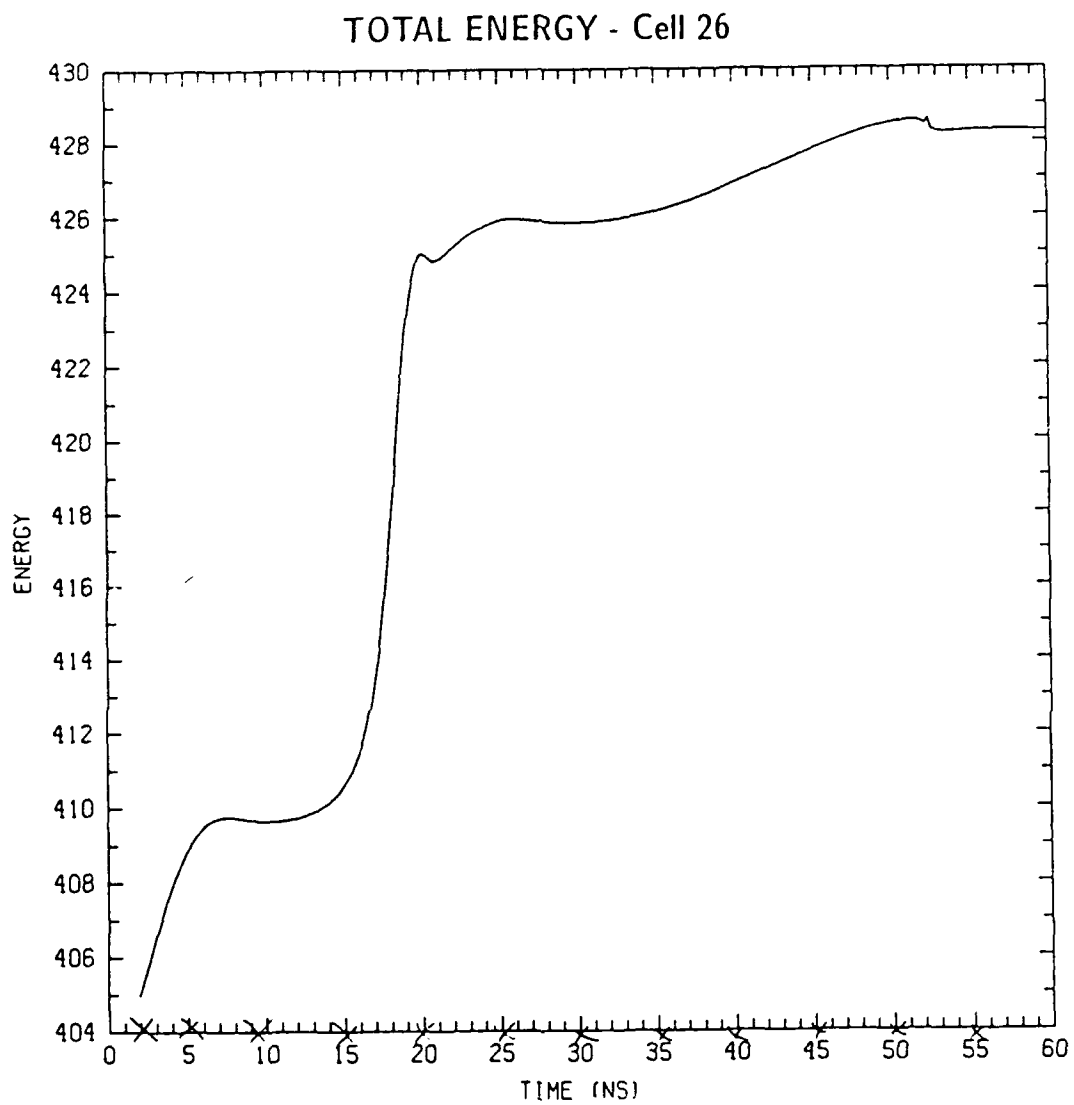


Figure 8

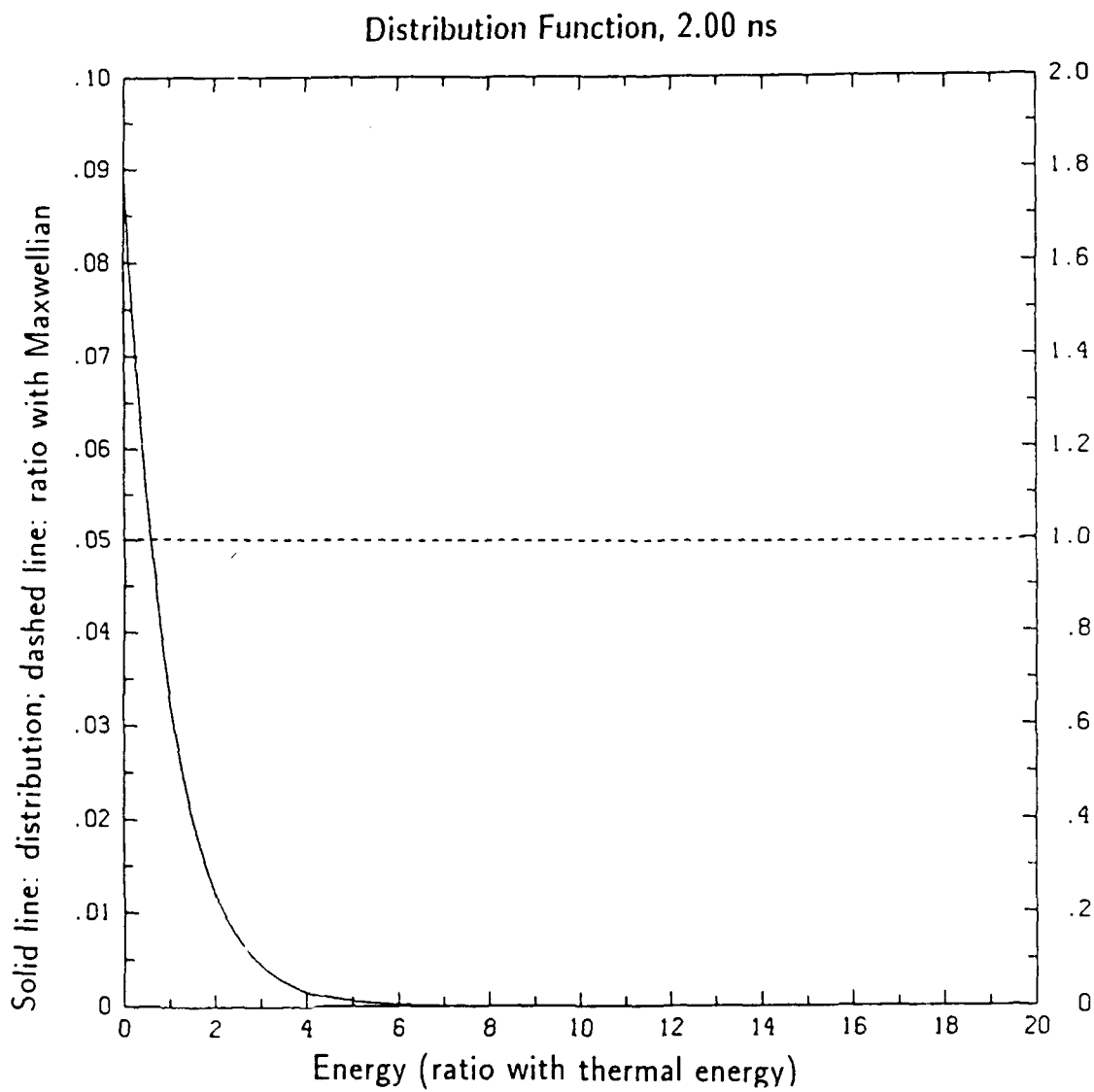


Figure 9A

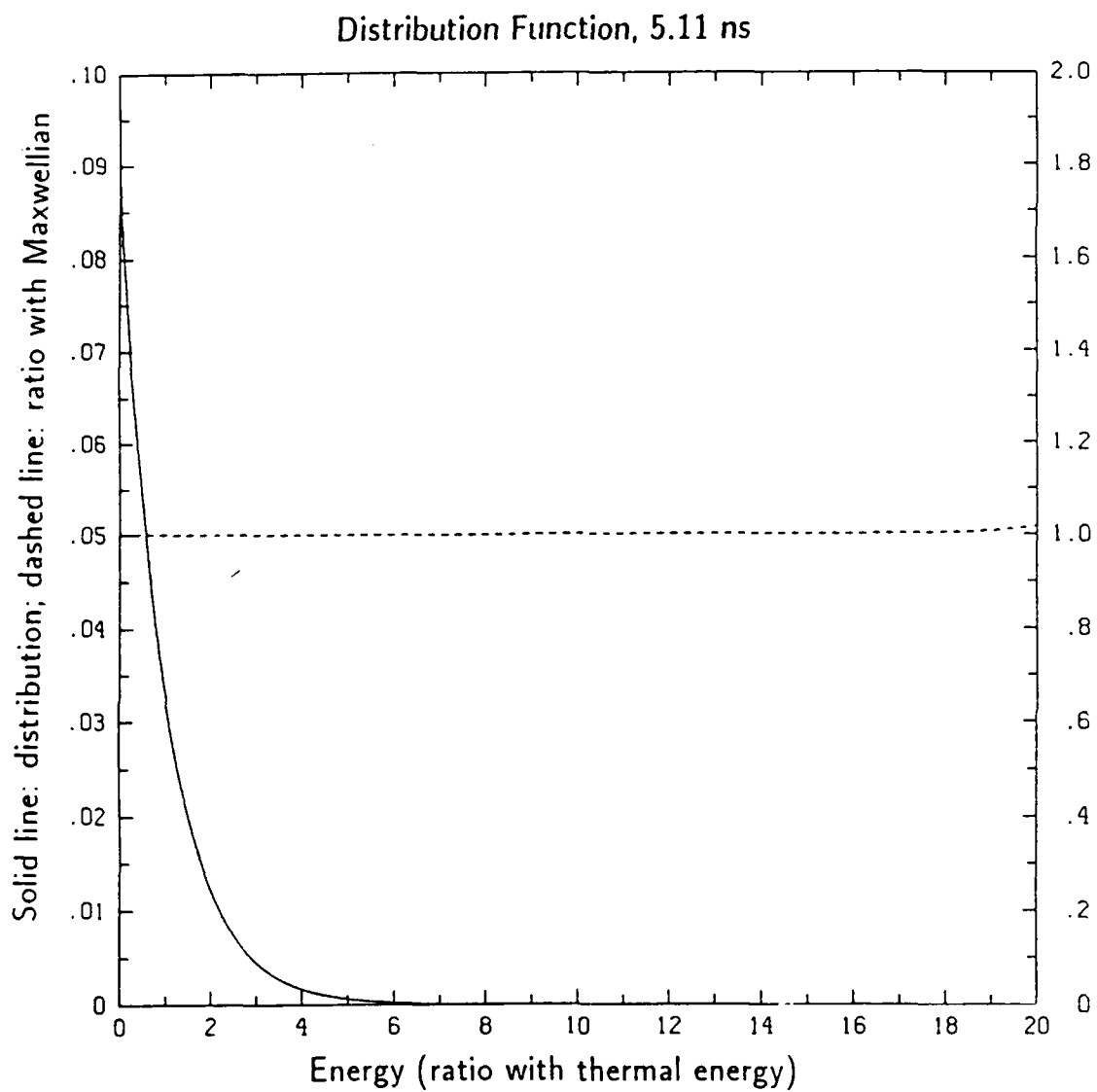


Figure 9B

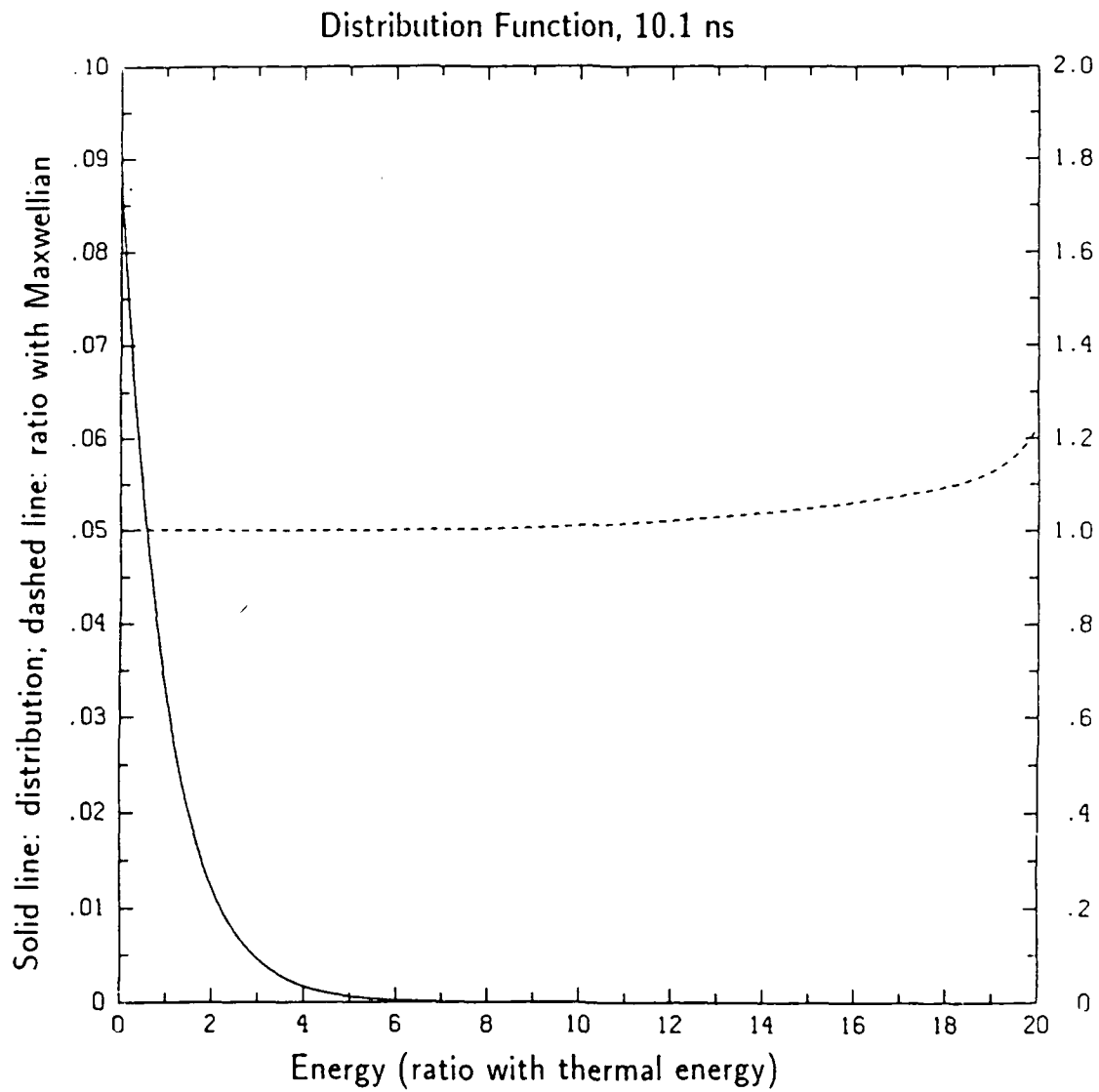


Figure 9C

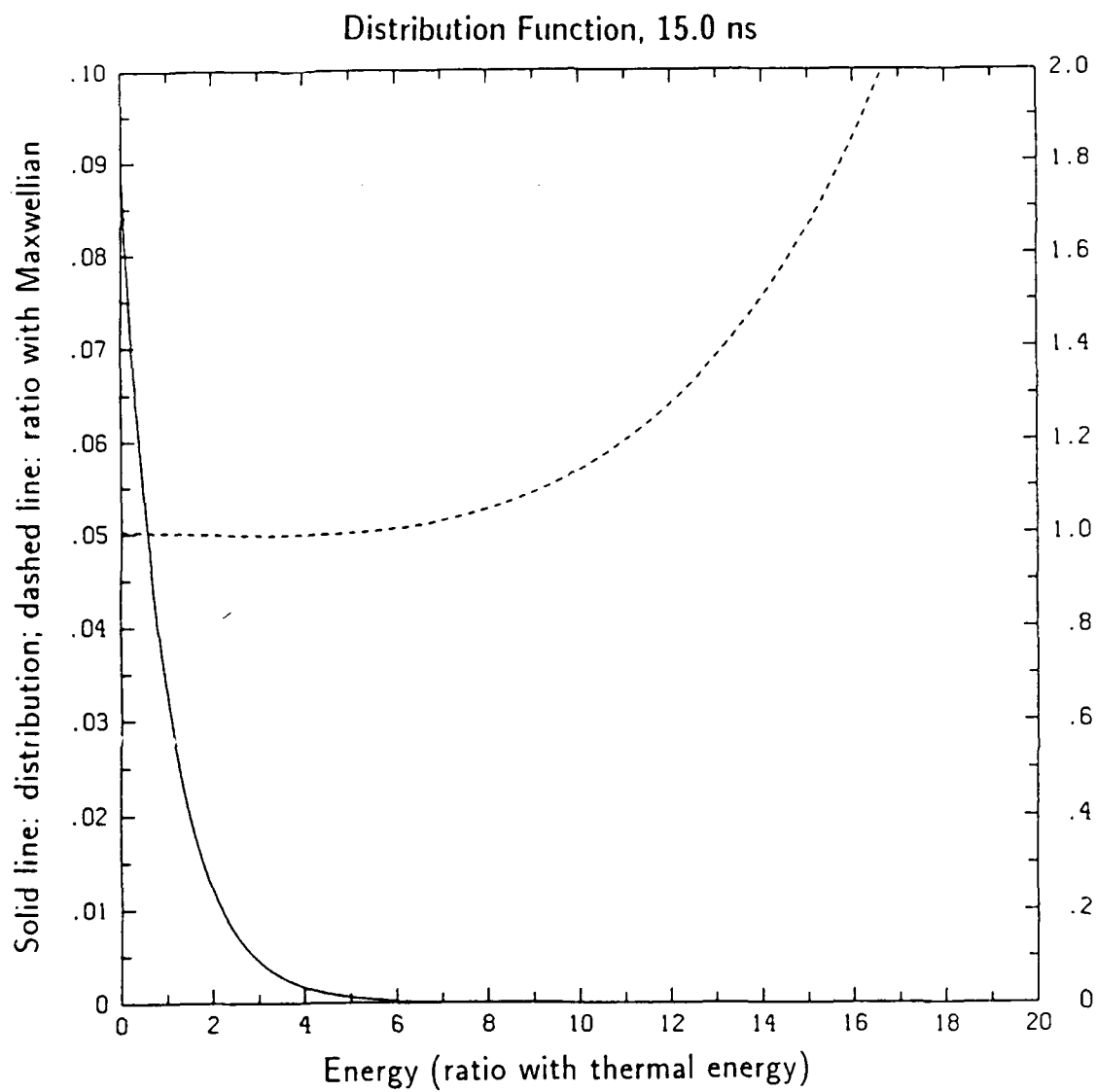


Figure 9D

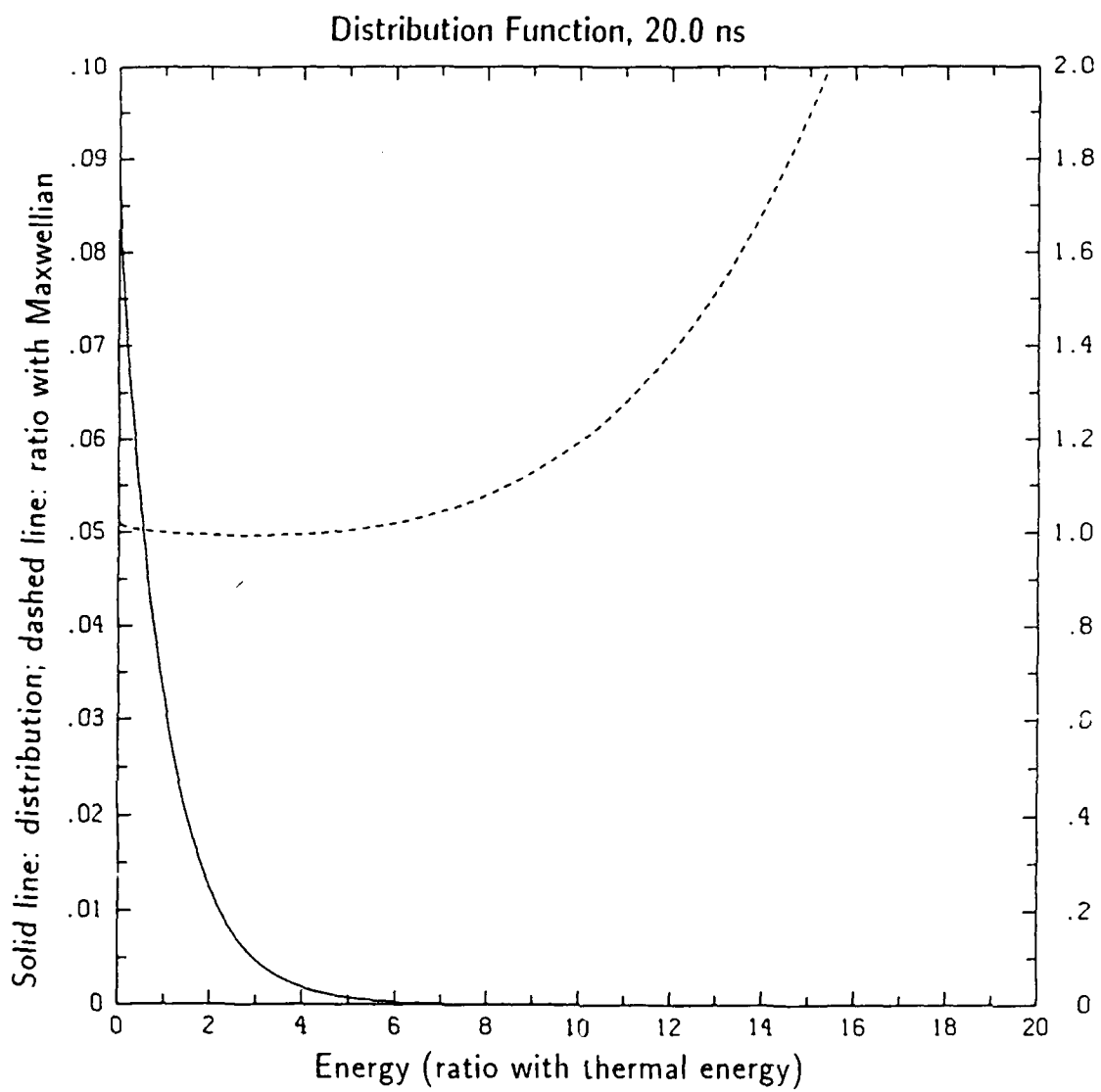


Figure 9E

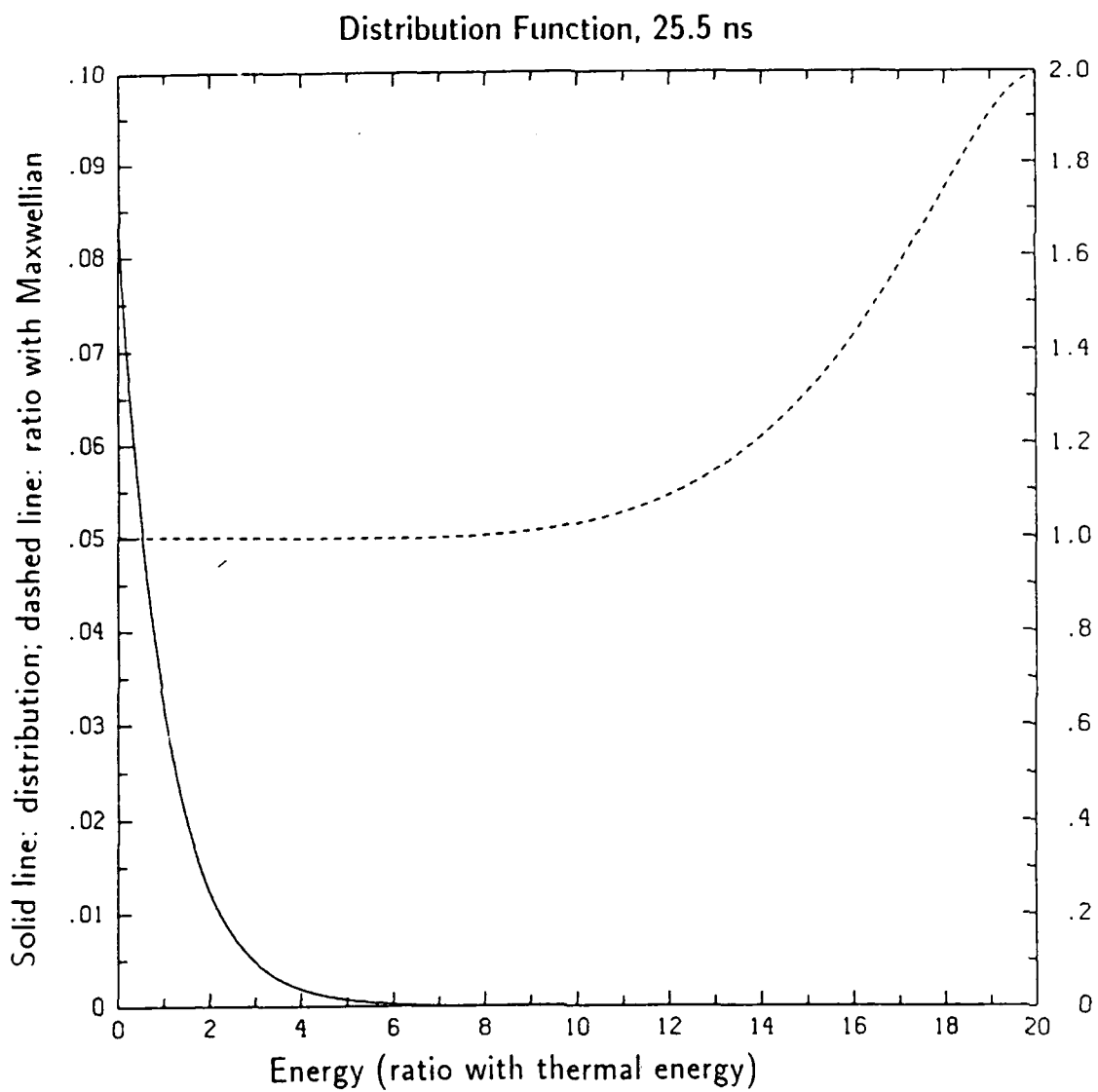


Figure 9F

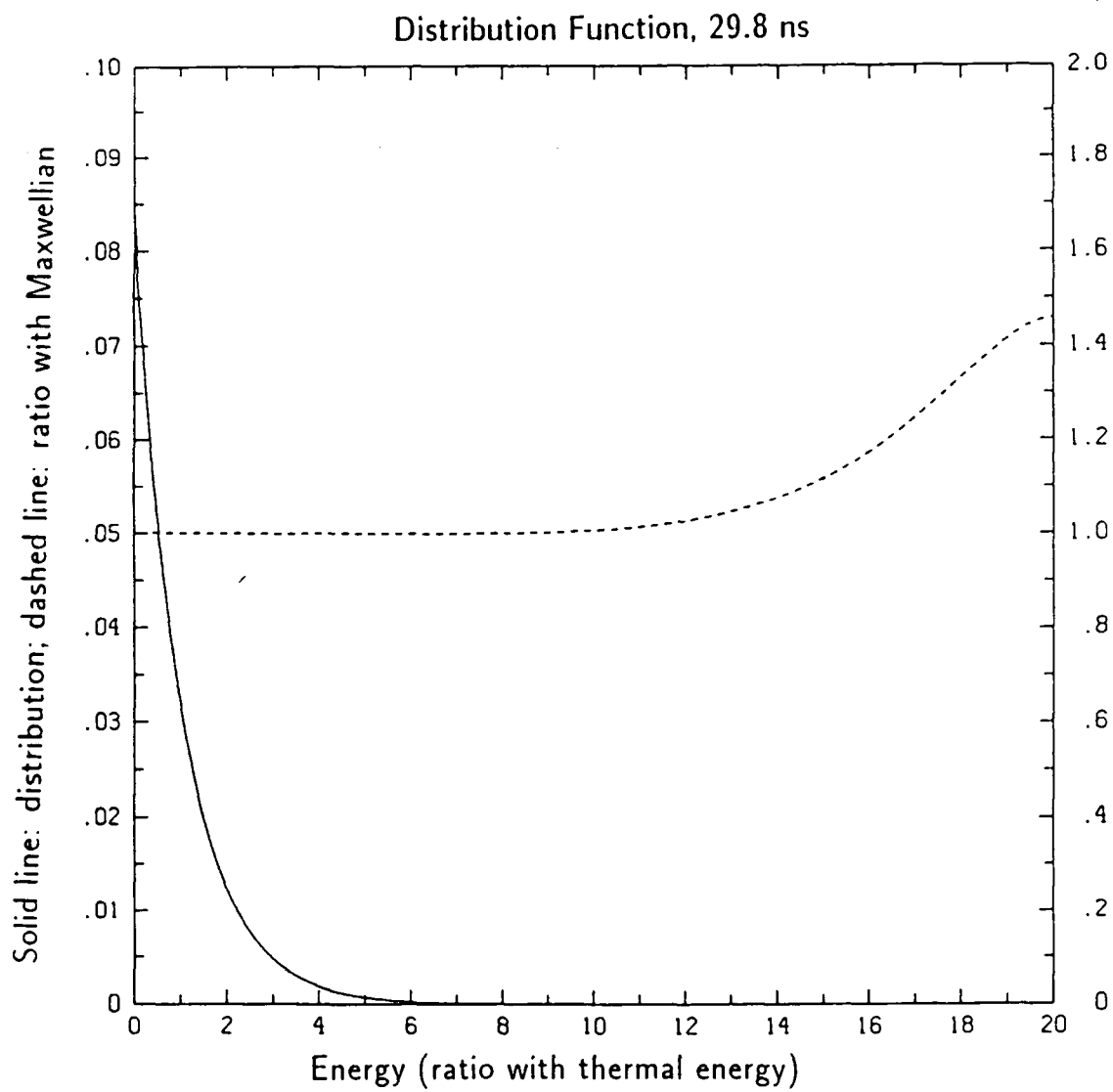


Figure 9G

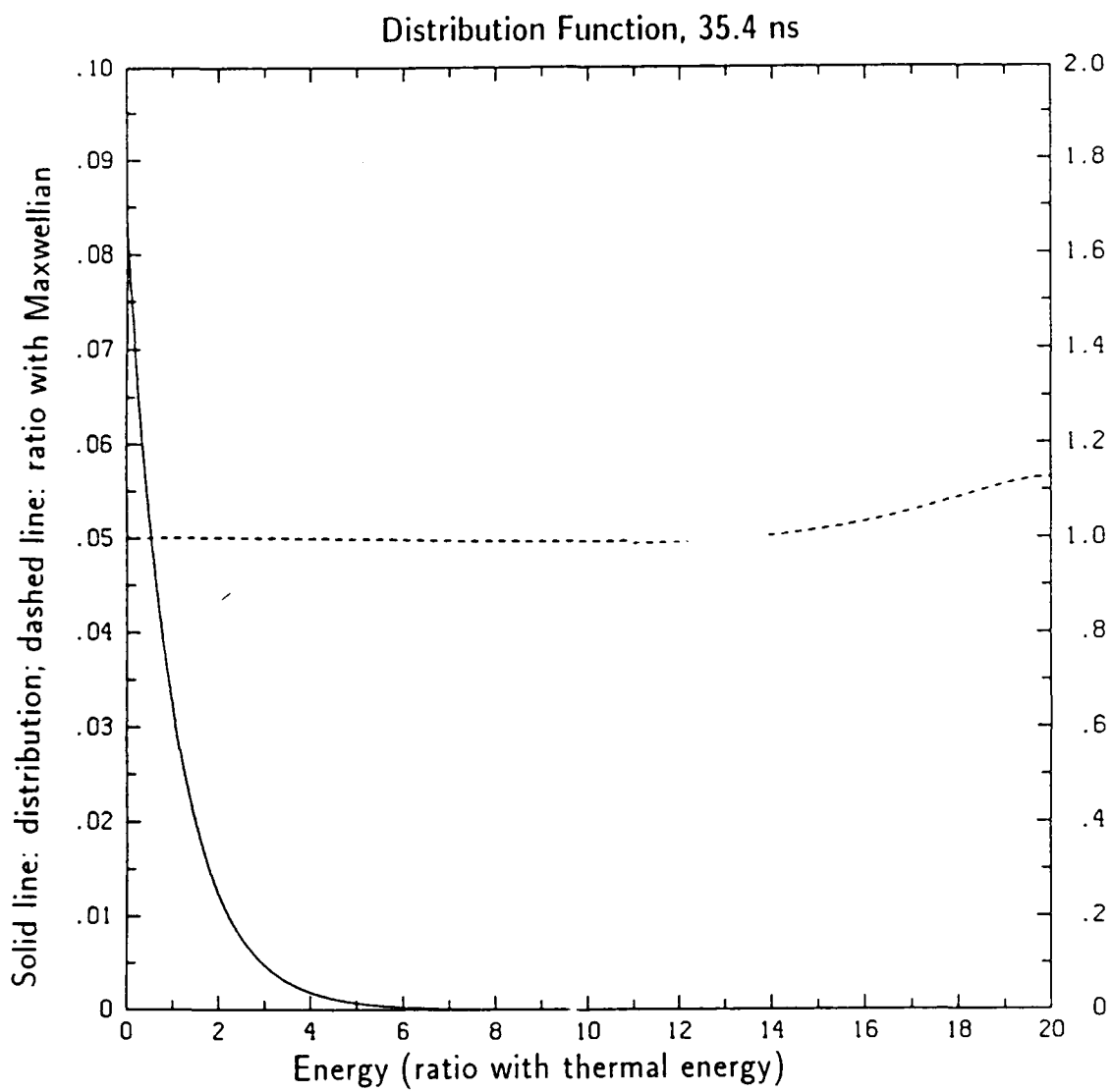


Figure 9H

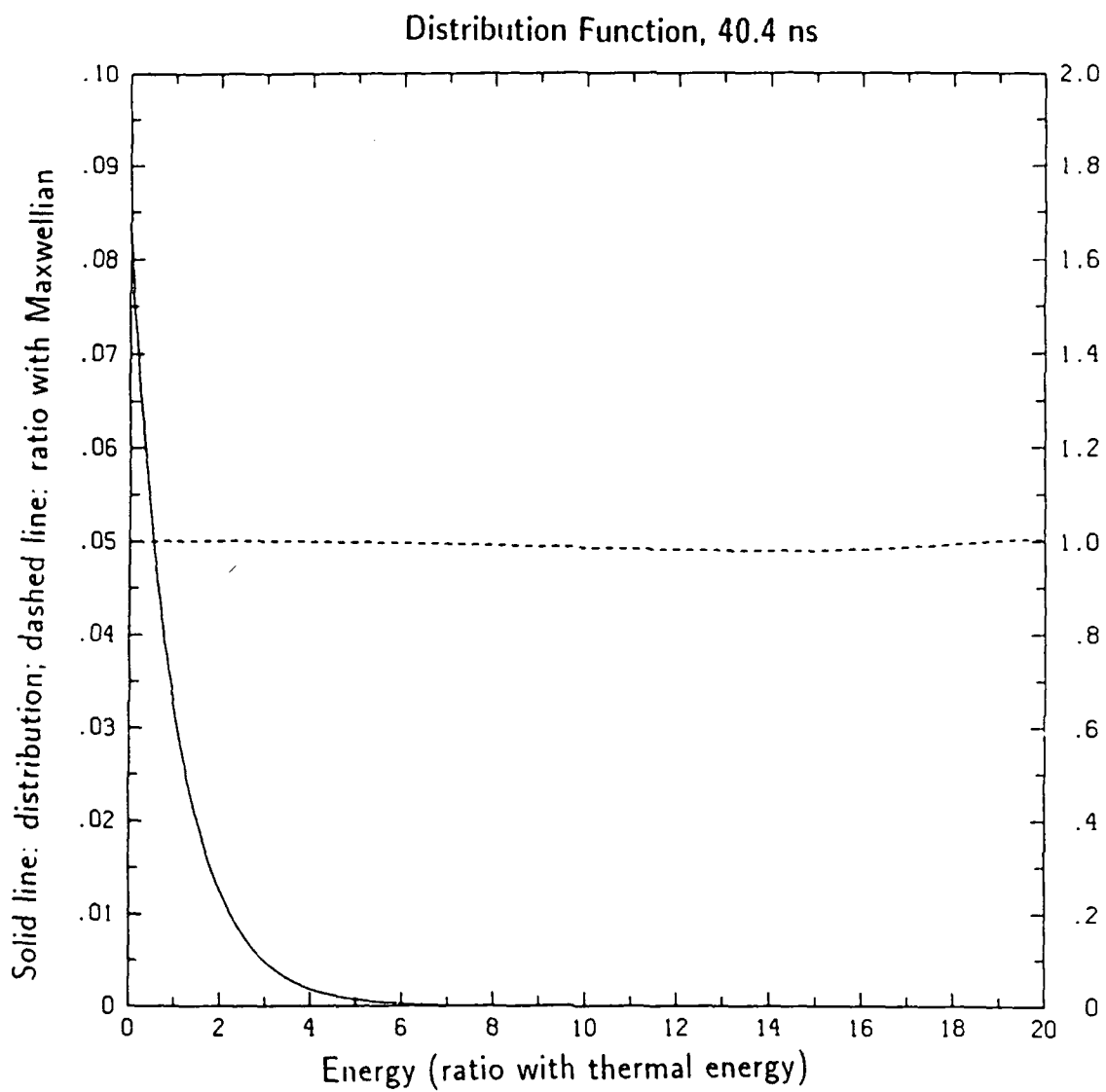


Figure 9I

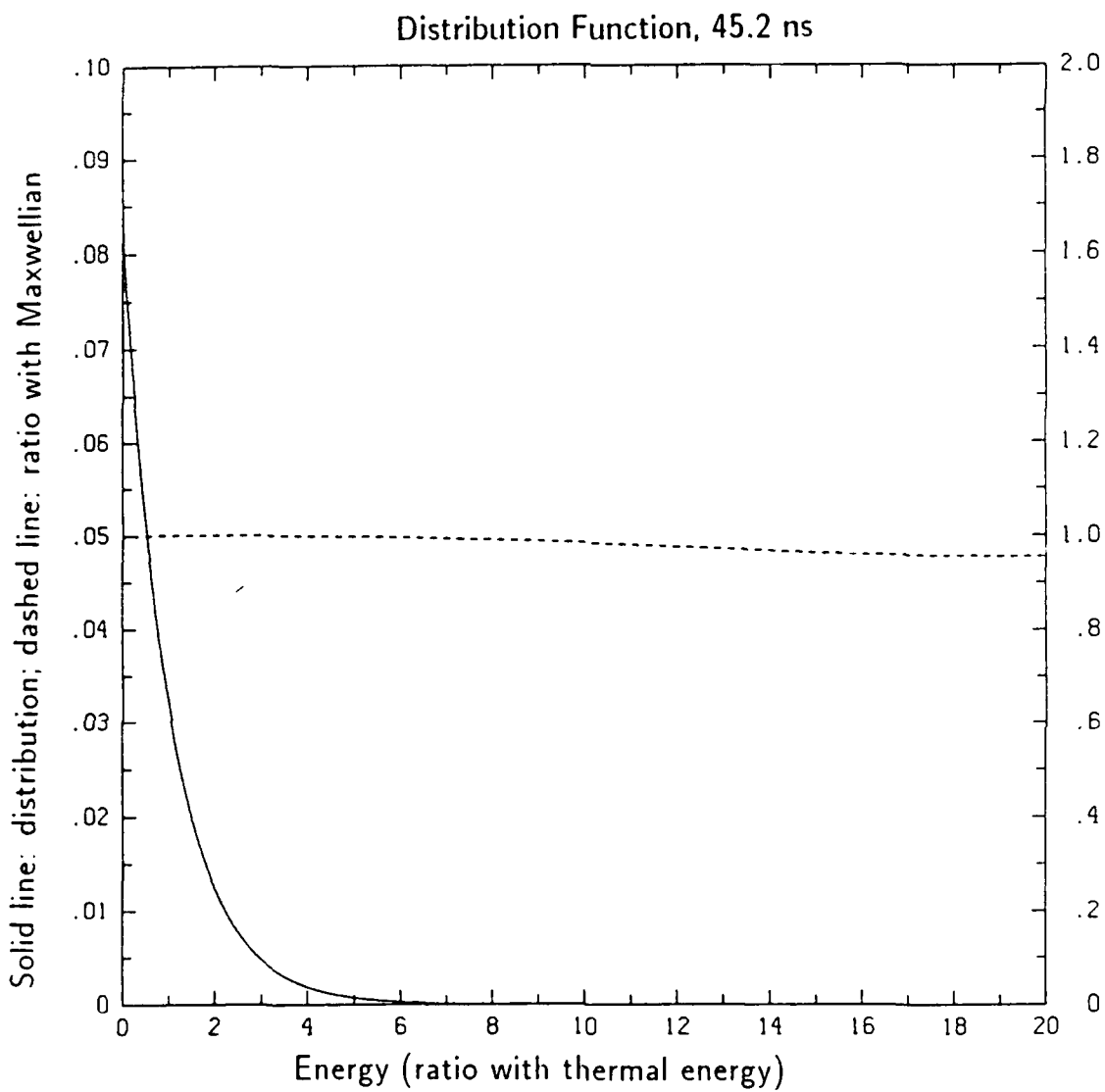


Figure 9J

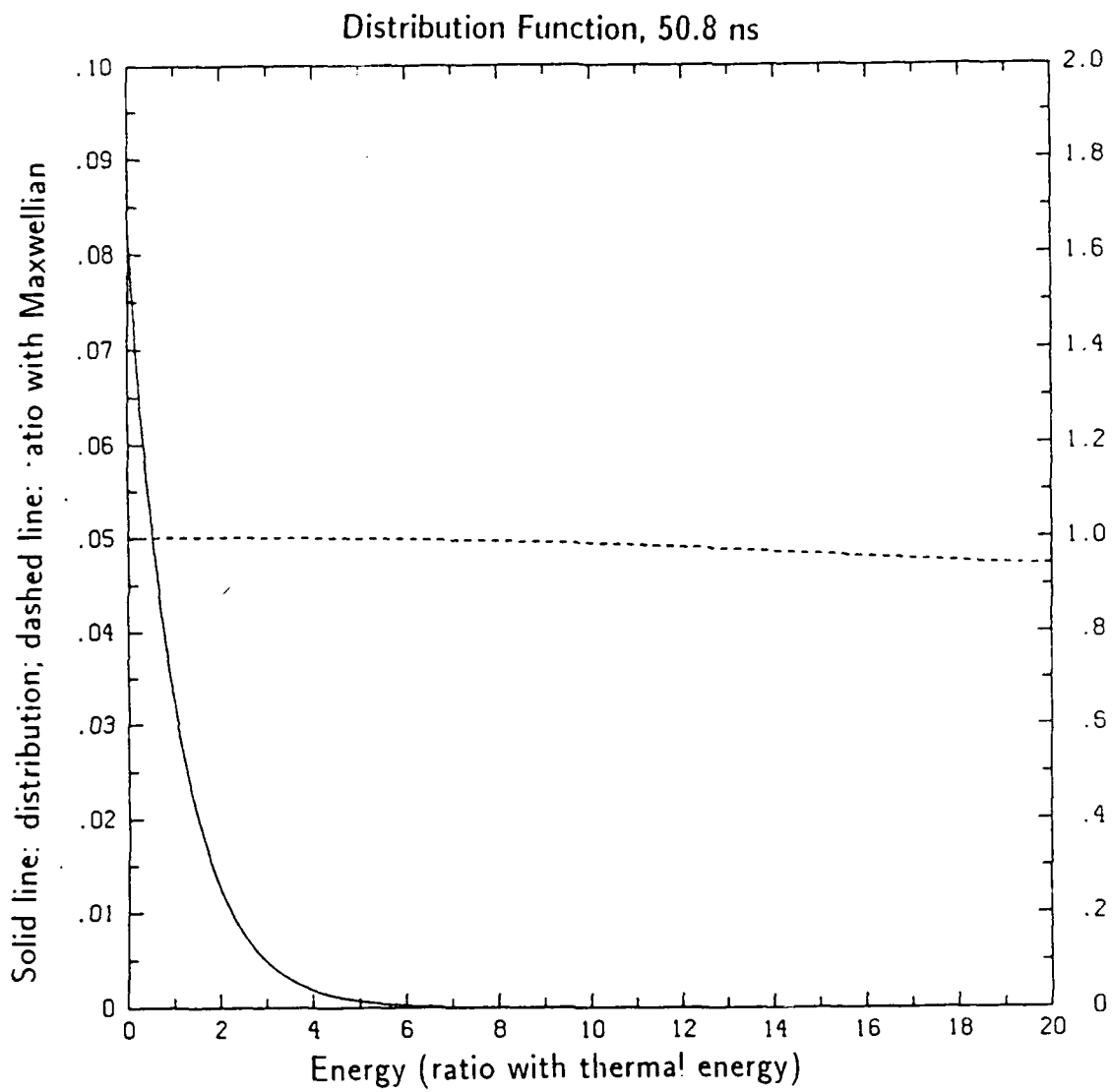


Figure 9K

V. DIELECTRONIC RECOMBINATION FROM FI-LIKE IONS

Dielectronic recombination (DR) is an essential tool for plasma diagnostics of atomic processes in high temperature and moderate density laboratory plasmas. The DR process involves the initial capture of a free electron by an ion X^{+Z} into a doubly excited state which stabilizes by subsequent radiative decay to singly excited states of $(X^{+(Z-1)})^*$ or by autoionization to the initial state X^{+Z} or any excited states $(X^{+Z})^*$ of this initial ion. The calculation of DR rate coefficients involve several different rate coefficients. For a specific doubly excited state configuration, one has to calculate autoionization rates to the ground state and all energetically possible excited states of the initial recombining ion, and also calculate stabilizing radiative decay rates to all dipole allowed singly excited states of the recombined ion. Depending on the complexity of each of these configurations, there are many different levels and this amounts to calculating a large number of both autoionization and radiative transition rates.

The DR rate coefficient α^{DR} from an initial state $|i\rangle$ into a specific stabilizing bound state $|k\rangle$ through a particular autoionization state $|j\rangle$ is given by :

$$\alpha^{DR}(i,j,k) = \left(\frac{4\pi}{kT}\right)^{3/2} a_o^3 \frac{e^{-2\epsilon_j/kT}}{2g_i} \frac{g_j A_{ji}^a A_{jk}^r}{\sum_i A_{ji}^a + \sum_k A_{jk}^r}$$

for a Maxwellian distribution of electrons, where g_i and g_j are the statistical weights of the initial and doubly excited states respectively,

T is the electron temperature and ϵ_j is the energy of the free recombining electron in Rydbergs. A_{ji}^a and A_{jk}^r are the autoionization and radiative rates from state $|j\rangle$ to states $|i\rangle$ and $|k\rangle$ respectively.

Most published works report only the total dielectronic recombination rates $\sum_{m,j,k} \alpha_{j,k}^{DR}(m,j,k)$, where the summation over m extends over all levels of the ground configuration $|i\rangle$ of the ion, as a function of temperature and the sum extends over all the singly excited bound final states as well. However, separate bookkeeping and presentation of partial atomic data such as the autoionization rates A_{ji}^a from state $|j\rangle$ to state $|i\rangle$, radiative rates A_{jk}^r from state $|j\rangle$ to all singly excited levels $|k\rangle$ below the ionization limit and dielectronic recombination rates $\sum_j \alpha_{j,k}^{DR}(i,j,k)$ from initial state $|i\rangle$ to specific final state $|k\rangle$ are extremely important for various reasons. With only the total rate coefficients, it is not possible to study density effects on these rates and to calculate DR rates accurately at densities of PRS (Plasma Radiation Source) interest; dielectronic recombination rates to these specific singly excited bound states are needed. Therefore, considerable effort was expended this year to set up the computer bookkeeping to isolate these rates and to define and calculate the necessary data files to make this data available to other of the ionization calculations that are to be carried out in this DNA program.

We have already finished calculating the partial as well as the total dielectronic recombination rate coefficients for Fl-like selenium and the partial dielectronic recombination rates for Fl-like iron. Since the autoionization and radiative rates are also very important atomic rates and are needed as well for CRE calculations, we treat them not as hidden by-

products of our DR rate calculations, but isolate and store the configuration averaged autoionization rates $A_j^a = 1/G_j \sum g_{j'} A_{j',i}^a$, where j' 's are the distinct levels for the particular doubly excited state $|j\rangle$ and the configuration averaged radiative rates $A_j^r = 1/G_j \sum g_{j'} A_{j',k}^r$ as well as we calculate and store the branching ratio

$$A^{DR}(i,j,k) = \sum g_{j'} \frac{\sum_m A_{j',m}^a A_{j',k}^r}{\sum_m A_{j',m}^a + \sum_k A_{j',k}^r}.$$

We have calculated these partial as well as the total rate coefficient for several different plasma temperatures of interest. Moreover, in calculating configuration averaged rates we had to calculate hundreds of autoionization rates and radiative rates for several doubly excited states and final states. For the case of recombination from fluorine-like to neon like ions, the averaged initial states consist of two electronic configurations, $1s^2 2s^2 2p^5(^2P)$ and $1s^2 2s^1 2p^6(^2S)$. The doubly excited states of the recombining ion however are based upon the following much larger set of configurations: $1s^2 2s^2 2p^4 3\ell n\ell'$, $1s^2 2s 2p^5 3\ell n\ell'$ and $1s^2 2p^6 3\ell n\ell'$, where n represents the principal quantum number of the Rydberg electron. Moreover, each of these configurations consists of a large number of multiplet structures over which these calculation must be averaged. The bound final states are based upon $1s^2 2s^2 2p^5 n\ell$ and $1s^2 2s^1 2p^6 n'\ell'$ or the ground state of neon-like ion $1s^2 2s^2 2p^6$. Additional autoionization to excited states of the recombined ion included $1s^2 2s^2 2p^4 3\ell$ and $1s^2 2s 2p^5 3\ell$ whenever they were energetically possible. For $1s^2 2s^2 2p^5$, DR involves not only $\Delta n \neq 0$ transitions but also $\Delta n = 0$ transitions. Here Δn refers to the change of principal quantum number of the jumping electron for radiative transitions.

The $\Delta n=0$ transitions become energetically possible for high Rydberg states, specifically for high-Z ions such as selenium. However, the contributions from these states to the rate is not that significant except at low temperatures. The autoionization and the radiative rates were calculated up to a certain n and ℓ values of the captured electron. To calculate the total rate, these rates were then extrapolated for higher n values, for both $\Delta n=0$ and $\Delta n \neq 0$ cases.

These rates were calculated and new bookkeeping procedures were set up using the atomic structure code of Robert Cowan.⁽¹⁾ The calculations were done in the Hartree-Fock approximation. Relativistic terms were included in the differential equation to give relativistic correction to the radial wave functions as well as to obtain improved energies. The continuum wave functions were calculated in the distorted wave approximation. All calculations were carried out in intermediate coupling and single configuration approximation. For each doubly excited state, all possible autoionization channels including autoionization to excited states of the initial state were considered. Similarly all possible dipole stabilizing radiative transitions for each doubly excited state were included in the calculations.

The DR-rate coefficient for Fe-like iron were presented to the American Physical Society meeting held in Hollywood, Florida on October 31-November 4, 1988. In that calculation, recombination rates for recombination through only the $3\ell 3\ell'$ and $3\ell 4\ell'$ manifold were considered. In calculating the DR-rates, partial recombination rates to each $n=3$ singly excited Ne-like states were obtained. To compare with other theoretical calculations, the total DR-rates for recombination to all final states for the doubly excited states considered were also calculated.

The autoionization and radiative rates calculated were obtained in such a way that DR rate coefficients to the $n=3$ states of Ne-like iron could be calculated for the first time for both Maxwellian and non-Maxwellian distributions. Moreover, these rates were coupled to a full CRE calculation of iron ionization and excited state abundances. They were found to have a significant impact on the degree of population and on the x-ray emission from the excited states of neon-like iron.

Figures 1-4 show results of the calculation for DR-rate coefficients for Fe-like iron. As mentioned before the DR-rates for this calculation include only $3l3l'$ and $3l4l'$ doubly excited states. Thus intermediate states with the captured electron in high Rydberg states have been neglected. They will be calculated to complete the rate coefficient calculations. When compared to total DR-rates of Ref. 2 for Se^{+24} of 2.55×10^{-11} and $2.59 \times 10^{-11} \text{ cm}^3/\text{sec}$ for 2S and 2P initial states at a temperature of 300 eV, our values of 2.55×10^{-11} and $1.69 \times 10^{-11} \text{ cm}^3/\text{s}$ are consistent. However, most theoretical calculations present only the total Dr-rates, and the contribution from higher autoionization states ($3lnl'$ with $n>5$, and $nlnl'$ with $n,n'>4$) are estimated to be approximately 30% - 40% of the total rate. Our maximum DR-rates of 1.69×10^{-11} and $2.55 \times 10^{-11} \text{ cm}^3/\text{s}$ at approximately 300 eV are 62% and close to 100% of Roszman's⁽³⁾ value for the 2P and 2S initial states respectively. When compared to a relativistic calculation of M. H. Chen⁽⁴⁾ our maximum rates at 300 eV are 44% and 76% of the total DR-rates for the 2P and 2S initial states.

Because of strong heating of a plasma, the distribution of atoms among the various ionization stages is no longer best represented by the Maxwellian electron distribution function. When the excitation and ionization rate coefficients are integrated over non-Maxwellian rather than

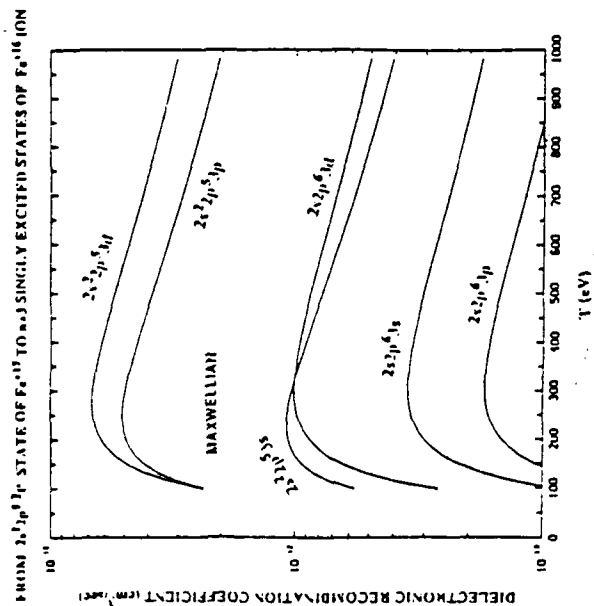


Figure 1

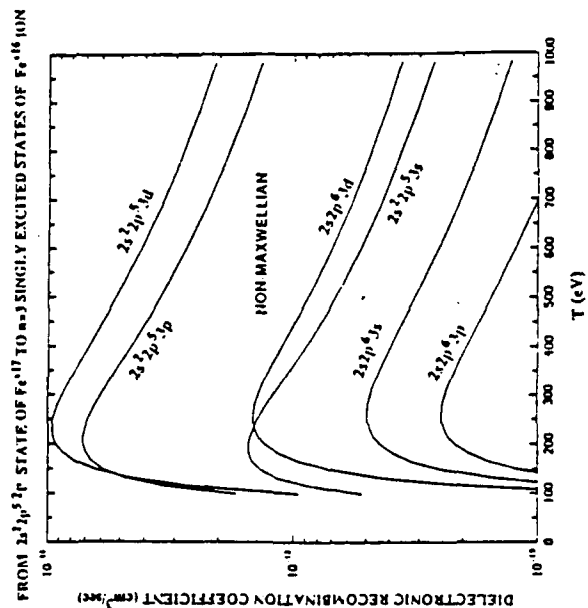


Figure 3

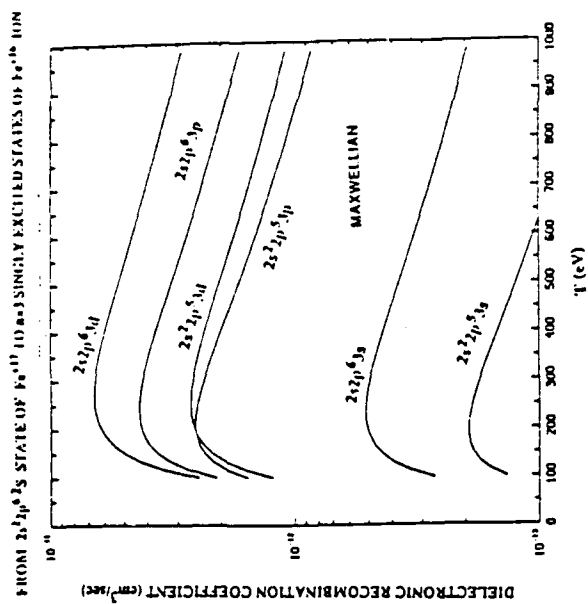


Figure 2

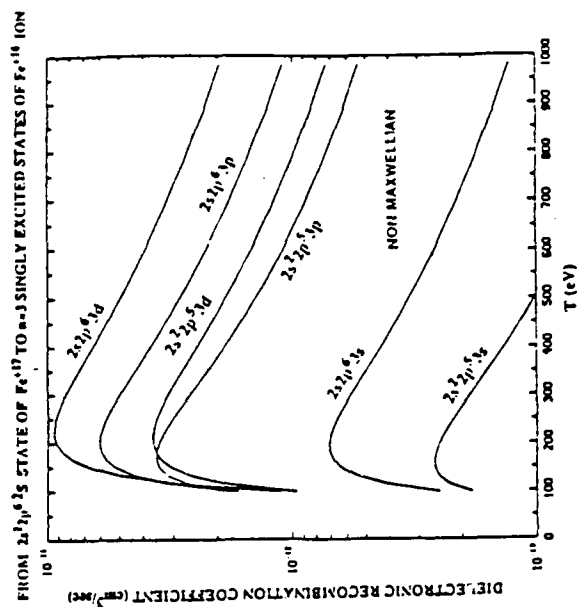


Figure 4.

the usual Maxwellian electron distribution function, they do not detail balance with the deexcitation and recombination(including dielectronic recombination) rate coefficients. This leads to significant shifts in ionization abundances as a function of temperature and in the excited state population distribution. Thus using the branching ratio A^{DR} obtained for this Fl-like iron calculation and integrating it over Maxwellian as well as non-Maxwellian distribution function, we found important effects of these rates on the excited state population of Fe XVI.

We will soon complete all the calculations for Fl-like iron and obtain the configuration averaged autoionization, radiative and dielectronic recombination rates as well as the partial and total dielectronic recombination rates. Next, we intend to carry out a similar calculation for Argon in the isoelectronic sequence. Once we have these three sets of data, we can proceed to obtain Z-scaling laws for the autoionization and dielectronic recombination rate coefficients. With the use of such scaling laws, it will be possible to carry out more accurate analyses of the feasibility of different elements in the isoelectronic sequence as plasma sources for Z-pinches. Equally important, scaling will allow us to obtain these rates throughout the portion of the periodic table of interest to DNA z-pinches with a great saving in the amount of theoretical effort expended than would otherwise be needed if they were calculated directly as was done with Se and Fe.

References

1. Atomic Structure Code of Robert D. Cowan following his book, "The Theory of Atomic Structure and Spectra," (University of California Press, Berkeley, 1981).
2. B. L. Whitten, et al., Phys. Rev. A 33, 2171 (1988).
3. L. J. Roszman, Phys. Rev. A 35, 2138 (1987).
4. M. H. Chen, Phys. Rev. A 38, 2332 (1988).

A number of new concepts are currently being investigated to improve the performance of the Plasma Radiation Source (PRS). Some of these concepts have been investigated and discussed fully in Ref. (1). By way of an introduction to this work a brief summary is presented below. The work describes a novel PRS that is potentially capable of producing significant amounts of radiation in the 3 - 15 keV range using moderate amounts of current, i.e., 1 - 2 MA. This source is similar to those being used in the dense z-pinch experiments being undertaken at the Naval Research Laboratory⁽²⁾ and Los Alamos National Laboratory⁽³⁾. Because of its connection with the DZP work, we will refer to this source as a Dense Z-pinch Plasma Radiation Source (DZPRS). The DZPRS is a solid fiber of deuterium, although other materials can be used, that is heated and compressed using a long rise time current pulse. The long rise time allows the plasma to be slowly heated and compressed as compared to the impulsive heating and compression that occurs in a normal PRS. We show that there are advantages in terms of radiative power and yields to heating and compressing in this manner. We employ Bennett hydrostatic equilibrium⁽⁴⁾ in our model to simulate the DZPRS. The Bennett equilibrium approximately includes electron degeneracy effects on the pressure. Furthermore, the model is self-consistently coupled to a circuit describing the pulse power machine.

In a conventional PRS scheme the load begins imploding at some distance from the axis, on the order of centimeters, and the current rise is fast, 10 - 100 kA/nsec. The kinetic energy rises with the current as the increasing $J \times B$ force does work on the plasma during the run-in phase. Then as the plasma begins to stagnate on axis, some of the stored kinetic energy is converted into internal energy by $P-d(\text{volume})$ work and shock heating. The result is a hot, highly ionized plasma which produces a radiation spectrum largely dependent upon the temperatures and densities achieved at stagnation. Zero- and 1-D PRS analyses show that there are two main requirements for producing radiation in the 3 - 15 keV range. First, there must be sufficient kinetic energy per ion to insure that large enough temperatures are obtained at stagnation, and secondly, the ion density has to be high so that the plasma can efficiently radiate. Although a modest current is theoretically capable of heating a small load to the necessary temperatures, it cannot do this and at

the same time push on enough mass to produce the ion densities needed for significant radiative emission. This theoretical result is supported by an experimental I^4 scaling law⁽⁵⁾ observed for K-shell emission in Neon plasmas. (Note, in order to conserve energy, at high currents this scaling law must turn over and be less than or equal to I^2 .) On the other hand, the K-shell emission might not be produced by direct conversion of kinetic energy into thermal energy as is proposed in the simple 0- and 1-D simulations. Rather it could arise from runaway electrons and hot spots generated by instabilities or other three-dimensional phenomena. The actual origin of the emission is still subject to theoretical and experimental investigation. From simple scaling arguments based on conventional z-pinch PRS loads, Apruzese and Davis⁽⁶⁾ found that a 60 kJ yield from the K-shell of iron, which is in the 10 keV photon range, would require a superclass generator of 100 TW. Further analysis of the-state-of-the-art PRS sources can be found in Refs. (7) and (8). In lieu of a superclass device it is worthwhile to investigate alternative schemes such as the DZPRS.

The essential difference between the DZPRS and the PRS is that ion densities at implosion are much larger for the DZPRS. Densities are higher because the load is initially at solid state density and rapid shock heating is minimized. The longer rise time of the current pulse in the DZPRS leads to a gentler "cooking" and compression compared to the rapid implosion in a PRS. These conditions make it possible to keep the plasma in a quasi-equilibrium or Bennett-like state whereby the average particle pressure inside the plasma is in equilibrium with the magnetic pressure at the edge of the plasma. The evolution of the plasma is determined by slow changes in this equilibrium pressure. There are three mechanisms controlling the pressure. They are: 1) the ohmic heating rate, 2) the radiative cooling rate and 3) the rate of change of the current. If the radiative rates dominate then the plasma will collapse, hence the name "radiative collapse". In general the ohmic heating rate is larger than the radiative cooling rate until the time at which the current becomes greater than or equal to the "Pease-Braginskii" current. There is experimental evidence to indicate that these plasmas remain stable while the current is rising: stable pinches have been observed for currents up to 640 kA⁽²⁾. If the DZPRS is found to be stable for higher currents and smaller line densities then have already been achieved, it will be possible to obtain the temperatures and densities needed to produce significant radiation

yields in the 3 - 15 keV range, as the plasma radiatively collapses. In our theoretical work we find that a deuterium plasma of 10^{18} cm^{-1} line density yields ~ 60 kJ of radiation above 3 keV while undergoing the radiative collapse. The significant feature is that this radiation production can be produced by a machine in the 1 - 10 TW class.

REFERENCES

- (1) J. W. Thornhill, J. L. Giuliani, and J. Davis, NRL Memorandum -- to be published.
- (2) J. D. Sethian, A. E. Robson, K. A. Gerber, and A. W. Desilva, Phys. Rev. Lett., 59, 892 (1987). Errata: ibid. p.1790.
- (3) J. E. Hammel and D. W. Scudder, Proc. 14th EUROP. Conf. on Controlled Fusion and Plasma Physics, Madrid 1987, Contributed Papers, Pt. 2 (EPS 1987), p.450.
- (4) W. H. Bennett, Phys. Rev., 45, 890 (1934); J. A. Bettencourt, Fundamentals of Plasma Physics, (Pergamon Press: New York, 1986), p.339.
- (5) S. J. Stephanakis, J. P. Apruzese, P. G. Burkhalter, J. Davis, R. A. Meger, S. W. McDonald, G. Mehlman, P. F. Ottinger, and F. C. Young, Appl. Phys. Lett., 48 (13), 829 (1986).
- (6) J. P. Apruzese and J. Davis, NRL Memorandum, 5406, (1984).
- (7) N. R. Pereira and J. Davis, J. Appl. Phys., 64, (1988).
- (8) K. G. Whitney, J. Davis, and N. R. Pereira, NRL Memorandum, 5970, (1987).

VII. Z-PIMP: A Zero-D Z-Pinch Implosions Code

A zero-dimensional plasma hydrocode called ZPIMP has recently been developed within the Plasma Radiation Branch. This code solves the hydrodynamic equations for a cylindrical plasma Z-pinch being driven by an applied external current. By using circuit parameters and an applied voltage appropriate to GAMBLE II, a circuit equation is solved for the current. The hydrodynamic model is coupled self-consistently to radiation physics routines which calculate the ionization energy, average charge, and radiative cooling of the plasma; opacity effects are taken into account in the radiation transport. Detailed atomic structure models or average-atom models are used to calculate the radiation physics results. Energy is conserved throughout the calculation.

This code has recently been applied to the simulation of Z-pinch implosions of Al plasmas under varying initial conditions. The object of the study was to observe the effects of the variation of these parameters on the implosion dynamics. Hopefully, these results can be a useful guide to experiments. These results will now be summarized.

It should be noted that in many of these simulations, the outer radius of the plasma reached a minimum value and "bounced," but subsequently exhibited a collapse. These results deal with data before or about the time of minimum outer radius; any subsequent collapse is not treated.

Results

A. Shells with Different Thickness

The ZPIMP code described in the preceding paragraphs was used to simulate the implosions of Al plasma shells of varying mass loading and initial radii. Mass loadings of 30, 35, and 40 $\mu\text{g}/\text{cm}$ were assumed. Initial outer and inner radii pairs used were (1.00, 0.90), (1.05, 0.85), and (1.15, 0.75) cm; these pairings gave initial shell thickness of 0.1, 0.2, and 0.4 cm. Initial electron and ion

temperatures of 5 eV were assumed. Some results of these calculations will now be presented.

Figure 1 shows the minimum outer radius R obtained in this series of runs (the inner radius always went to zero). The smallest R always resulted at the lowest density and smallest shell thickness. Figure 2 gives the times of peak compression for this set of calculations. The earliest time occurs for the smallest shell thickness and lowest density.

This pattern of the highest maximum parameter occurring for the smallest shell width and density occurs in the next several plots (Figs. 3-7) for electron temperature, average charge and radiated power. The higher radiative cooling under these conditions allows the plasma to be compressed to higher densities (or smaller radii). The exceptions are the line and continuum radiation maxima below the K edge, which are fairly flat.

All the \bar{Z} maxima are well above 11, which means that the Al ions are usually in the He-like and H-like states at peak compression. This is reflected in the fact that the line and continuum radiation maxima above the K edge are higher than those below the K edge. These results indicate that, under the set of conditions simulated by these calculations, it should be possible to create highly-ionized Z-pinch Al plasmas in the NRL GAMBLE II device.

B. Filled Cylinder Plasmas

Using the same mass loadings, a set of filled-shell (inner radius=0) runs were made for different initial outer radii ranging from 0.5 cm to 2.0 cm. Initial temperatures of 5 eV were assumed. The next several figures show some results from these calculations.

Figure 8 shows the minimum outer radius R_{\min} obtained at each mass loading vs. initial outer radius R_0 . Generally, the trend is for R_{\min} to increase with R_0 . However, the 35 $\mu\text{g}/\text{cm}$ curve peaks slightly at $R_0=1.875$ cm, and the 40 $\mu\text{g}/\text{cm}$ curve shows a very pronounced dip between 1.625 cm and 2.0 cm. Unlike Figure 1, the smaller R_{\min} occurs at the larger mass loadings.

Figure 9 gives the times of maximum implosion (R_{\min}) vs. R_0 for the different mass loadings. The larger times occur at the larger mass loading and larger R_0 , generally.

Figure 10 displays the maximum electron temperatures achieved during these calculations. These maxima usually occurred at, or just prior to, maximum implosion. The higher maximum temperatures result at the lower masses. The 40 $\mu\text{g}/\text{cm}$ curve drops very rapidly in the area where R_{\min} also decreases rapidly, then it seems to stabilize as R_{\min} increases again.

The maximum average ionic charge \bar{Z} is shown in Figure 11. The results seem to peak around $R_0=1.0$; the highest ionization occurs at the smallest mass. The 40 $\mu\text{g}/\text{cm}$ curve crosses $\bar{Z}=11$ in the region where R_{\min} drops rapidly. When \bar{Z} is 11 or greater, He-like and H-like ions are predominant. When \bar{Z} drops below 11, L-shell radiation appears. The result of \bar{Z} falling below 11 is enhanced L-shell radiation and total radiation as will be seen in subsequent figures.

Figure 12 shows the maximum total radiated power for these runs. The higher radiation occurs for the larger mass, which helps to explain the fact that the smaller R_{\min} occur with the larger mass.

Figures 13 and 14 give the maximum line and continuum radiation below and above the K edge. Figures 12, 13a, and 14a show an increase in radiated power at 40 $\mu\text{g}/\text{cm}$ at $R_0 \approx 1.69$ cm. This is the point at which maximum \bar{Z} crosses 11 and at which R_{\min} decreases rapidly. The enhanced cooling of the plasma, as shown in Figure 10, reduces plasma pressure and allows for increased compression. Beyond $R_0 \approx 1.75$ cm, the radiative cooling drops; plasma thermal energy is retained and it becomes harder to compress the plasma. Hence R_{\min} increases again.

It should also be noted in Figures 13a and 14a that the L-shell radiative cooling reaches a minimum at large R_0 and rises again for the 35 $\mu\text{g}/\text{cm}$ mass. This accounts for the peak in this R_{\min} curve noted earlier.

These curves show high radiative losses at low R_0 for all the mass loadings; hence, all R_{\min} are small at small R_0 .

RD-A211 665

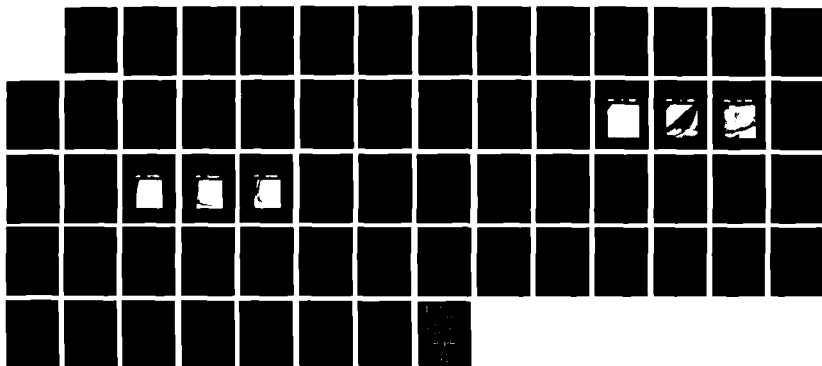
ADVANCED CONCEPTS THEORY ANNUAL REPORT 1988 (U) NAVAL
RESEARCH LAB WASHINGTON DC 03 AUG 89 NRL-MR-6517
NIPR-88-577

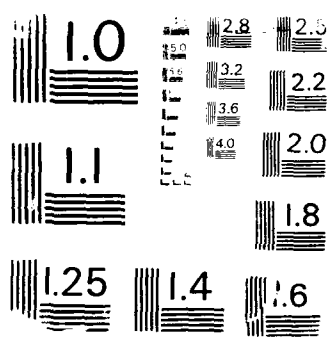
272

UNCLASSIFIED

F/G 20/9

NL





Conclusions

Using a one-cell (zero-dimensional) plasma hydrocode coupled to a detailed atomic physics radiation package, an attempt has been made to model the Z-pinch implosion of an Al plasma using parameters suitable to the NRL GAMBLE II device. The energy conserving hydrocode solves a circuit equation for the current using a GAMBLE II voltage profile and circuit parameters. The code is coupled self-consistently to the radiation package. The effects of the variation of such parameters as mass loading, radius, and shell thickness have been studied, and the results have been summarized here. It is hopeful that these results will be a useful guide to experiments.

Figure Captions

Fig. 1 Minimum outer radius for the thin shell Al plasma implosions. The solid line represents a shell thickness $\Delta R = 0.1$ cm, the long dashed line represents $\Delta R = 0.2$ cm, and the short-dashed line represents $\Delta R = 0.4$ cm.

Fig. 2 Time of maximum implosion for the thin shell cases. Same notation as Figure 1.

Fig. 3 Maximum electron temperature for the thin shell cases. Same notation as Figure 2.

Fig. 4 Maximum average ionic charge for the thin shell cases. Same notation as Figure 1.

Fig. 5 Maximum total radiated power for the thin shell cases. Same notation as Figure 1.

Fig. 6 Maximum line radiation below (a) and above (b) the K edge for the thin shell cases. Same notation as Figure 1.

Fig. 7 Maximum continuum radiation below (a) and above (b) the K edge for the thin shell cases. Same notation as Figure 1.

Fig. 8 Minimum outer radius for the filled cylinder Al plasma implosions. The solid line is 30 $\mu\text{g}/\text{cm}$, the long-dashed line is 35 $\mu\text{g}/\text{cm}$, and the short-dashed line is 40 $\mu\text{g}/\text{cm}$.

Fig. 9 Time of maximum implosion for the filled cylinder cases. Same notation as Figure 8.

Fig. 10 Maximum electron temperature for the filled cylinder cases. Same notation as Figure 8.

Fig. 11 Maximum average ionic charge for the filled cylinder cases. Same notation as Figure 8.

Fig. 12 Maximum total radiated power for the filled cylinder cases. Same notation as Figure 8.

Fig. 13 Maximum line radiation below (a) and above (b) the K edge for the filled cylinder cases. Same notation as Figure 8.

Fig. 14 Maximum continuum radiation below (a) and above (b) the K edge for the filled cylinder cases. Same notation as Figure 8.

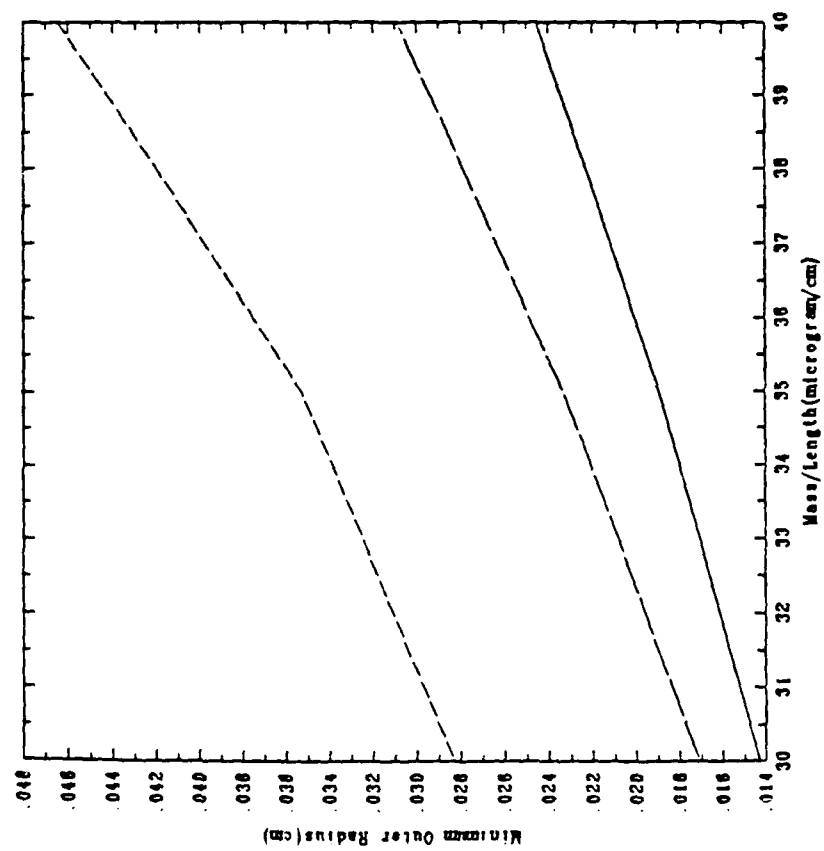


Figure 1

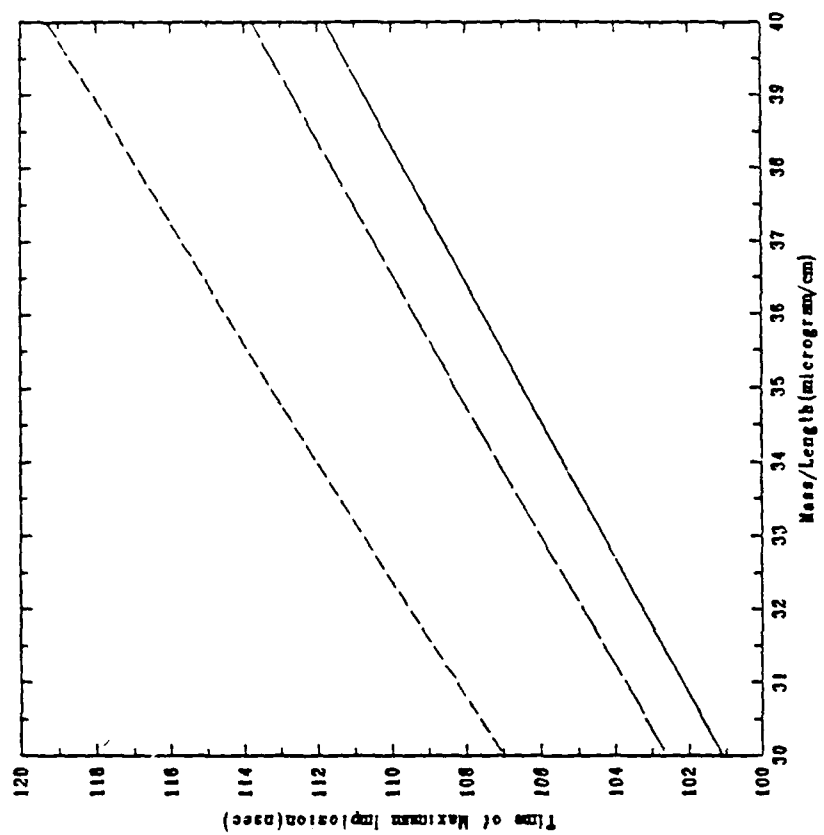


Figure 2

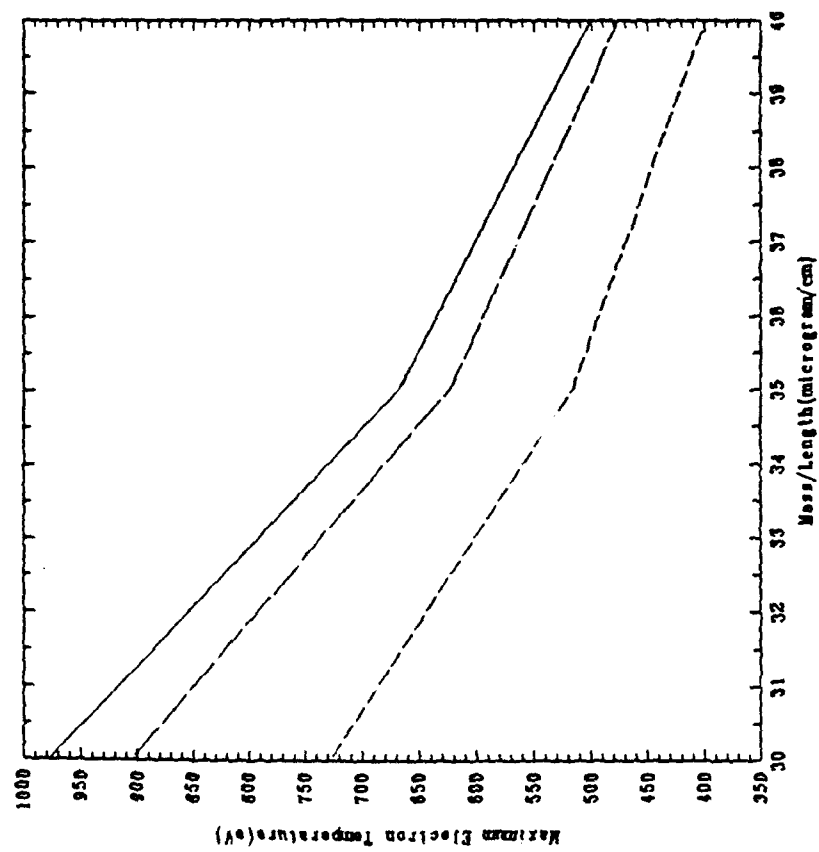


Figure 3

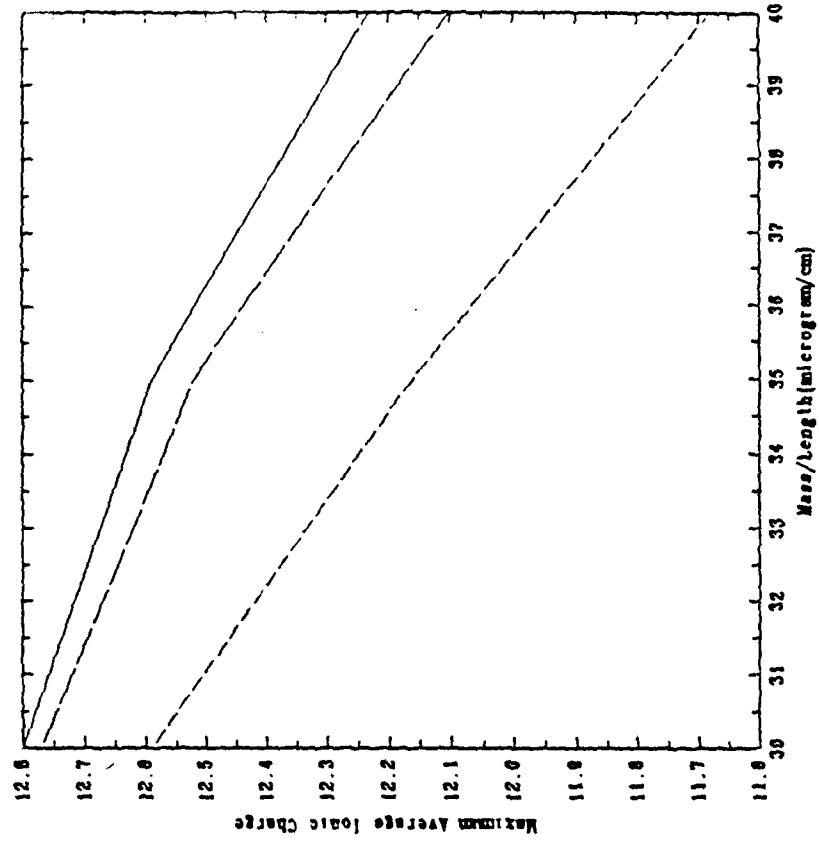


Figure 4

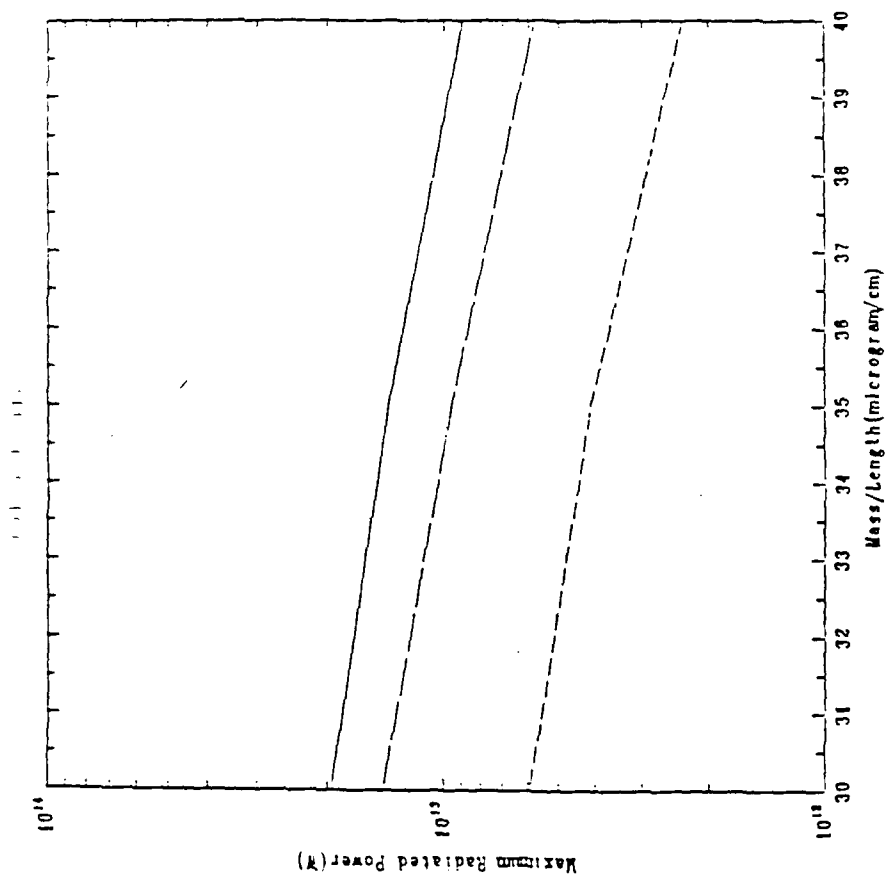


Figure 5

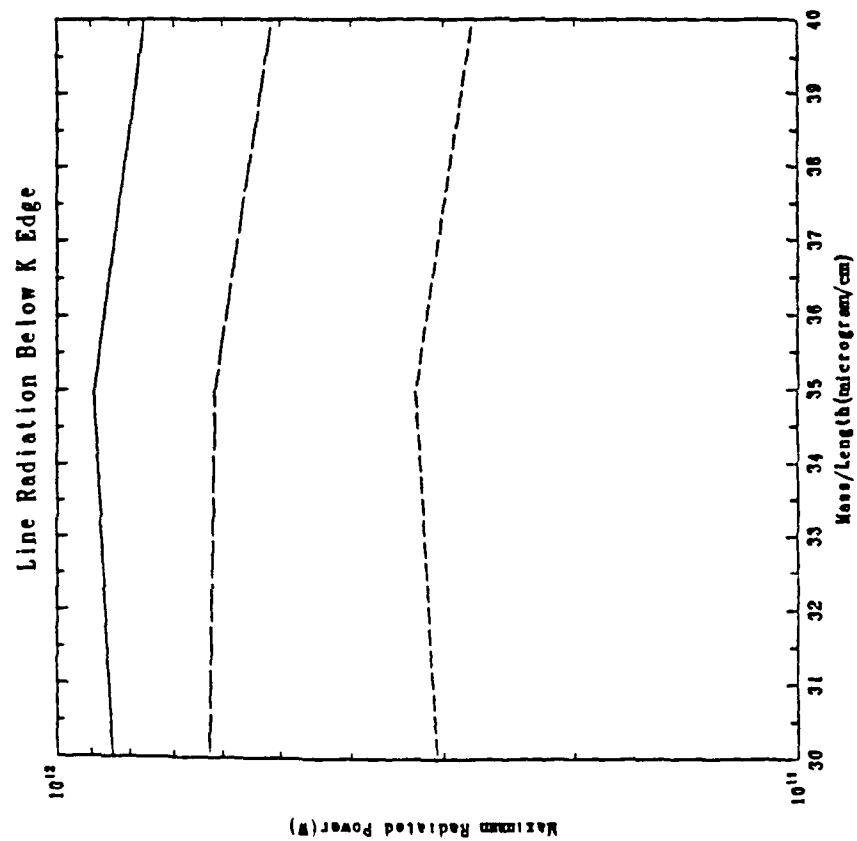


Figure 6(a)

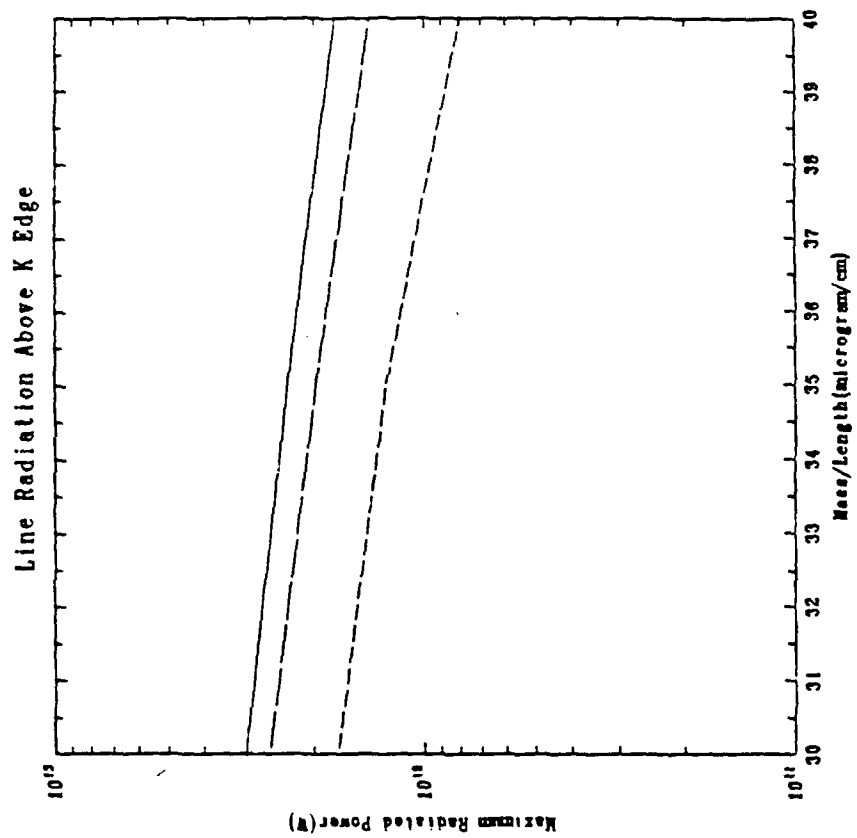


Figure 6(b)

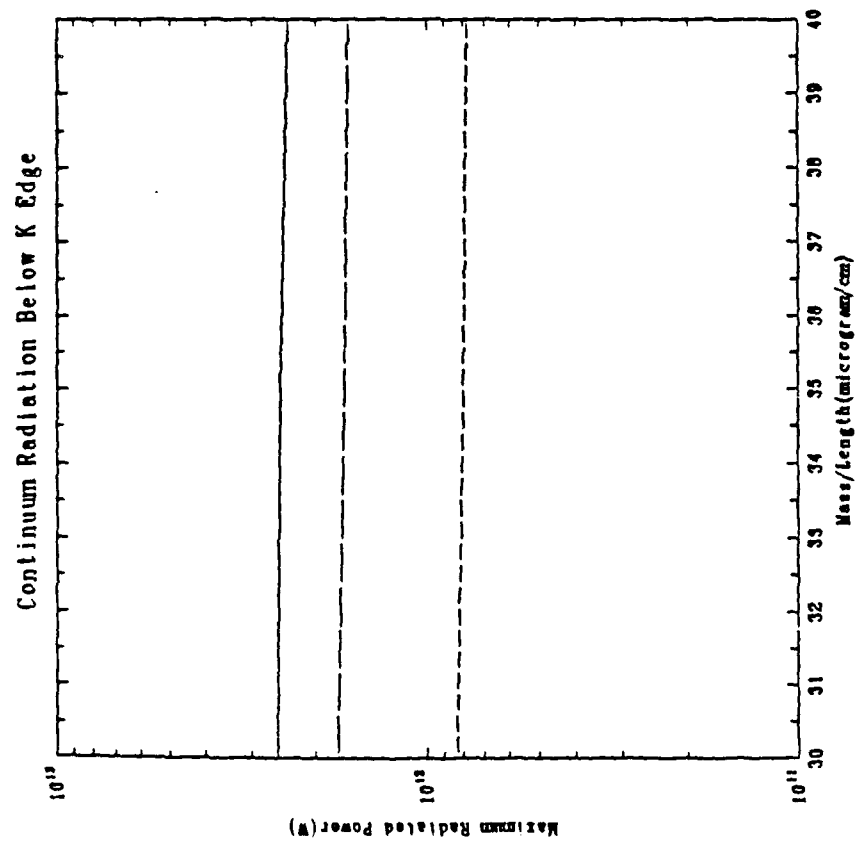


Figure 7(a)

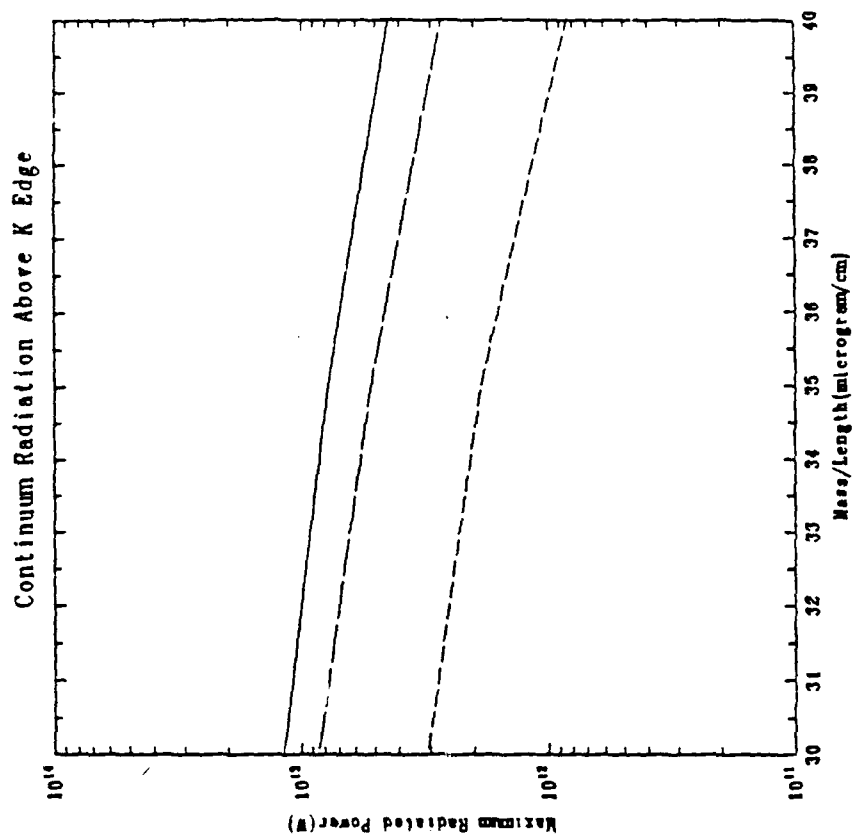


Figure 7(b)

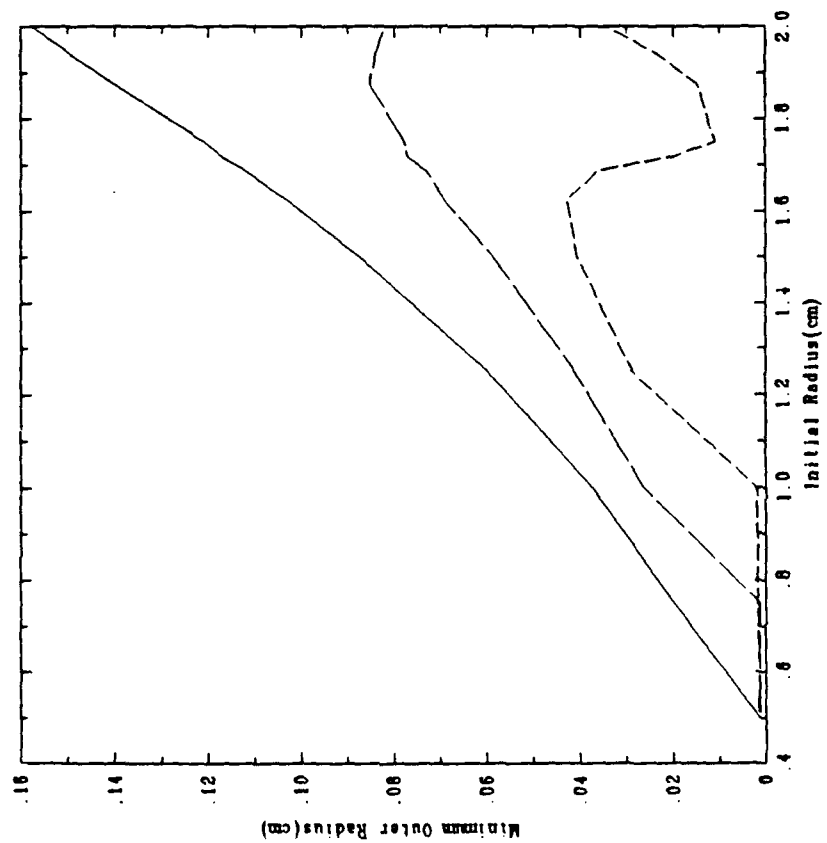


Figure 8

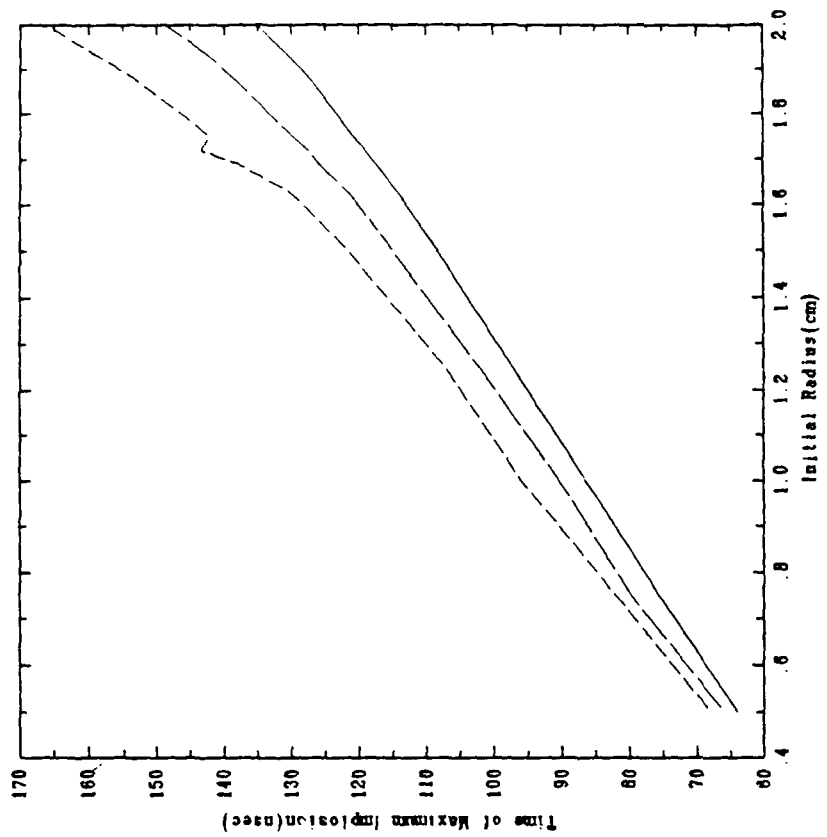


Figure 9

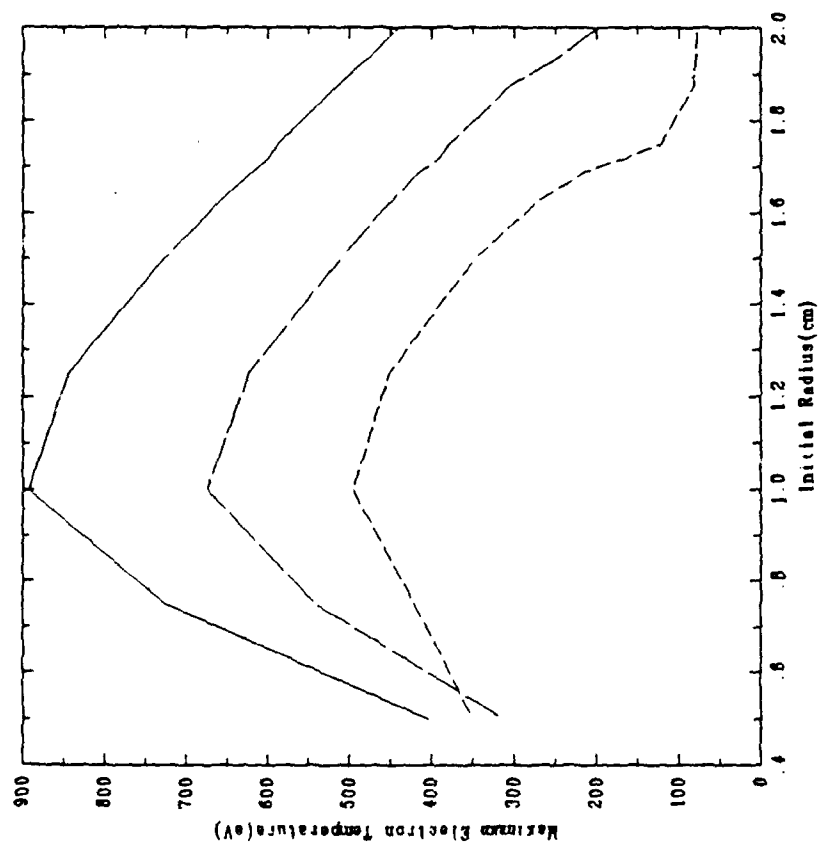


Figure 10

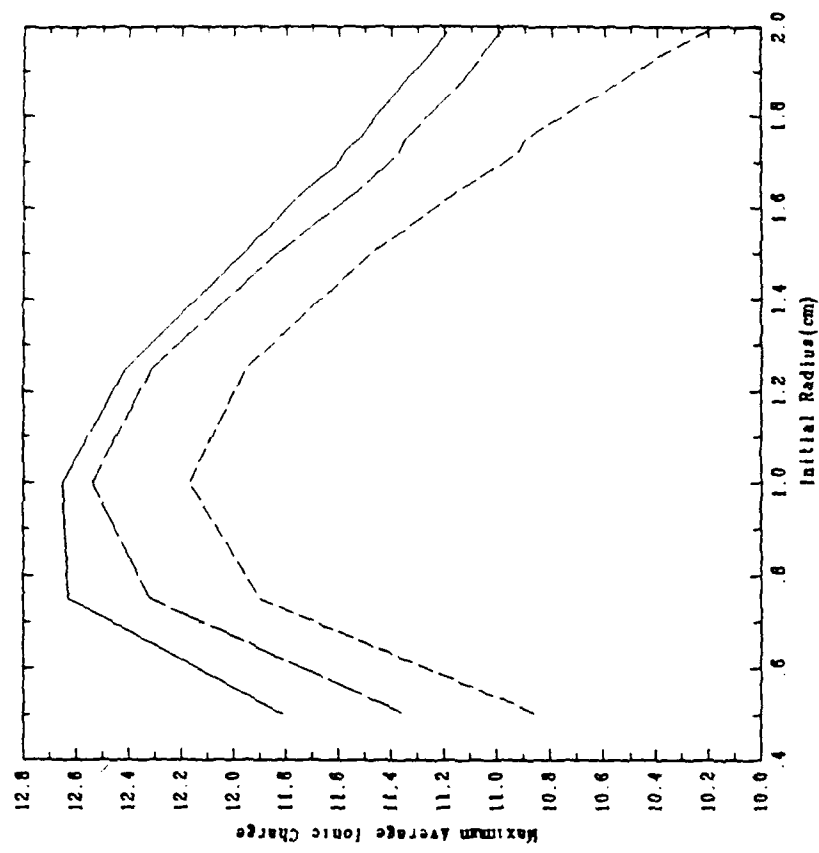


Figure 11

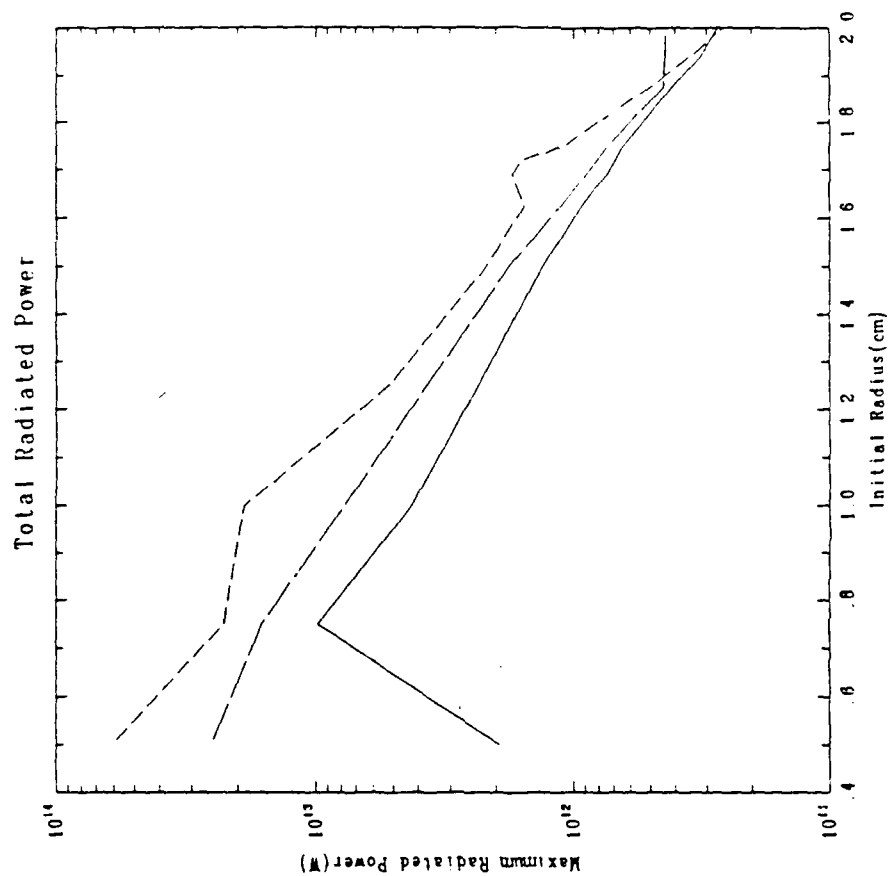


Figure 12

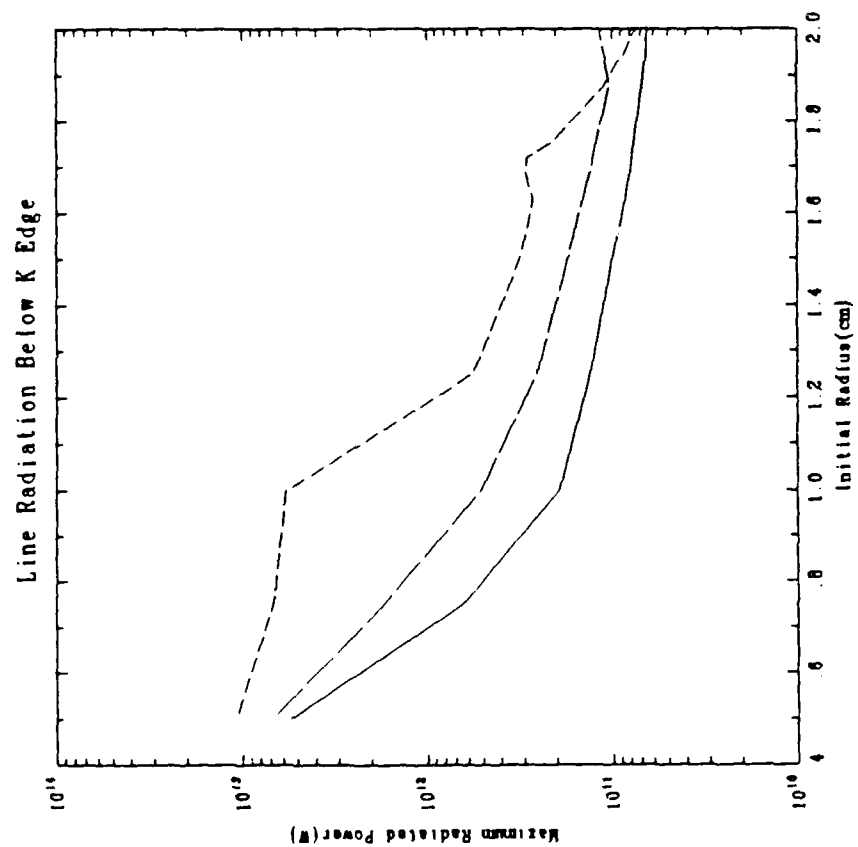


Figure 13(a)

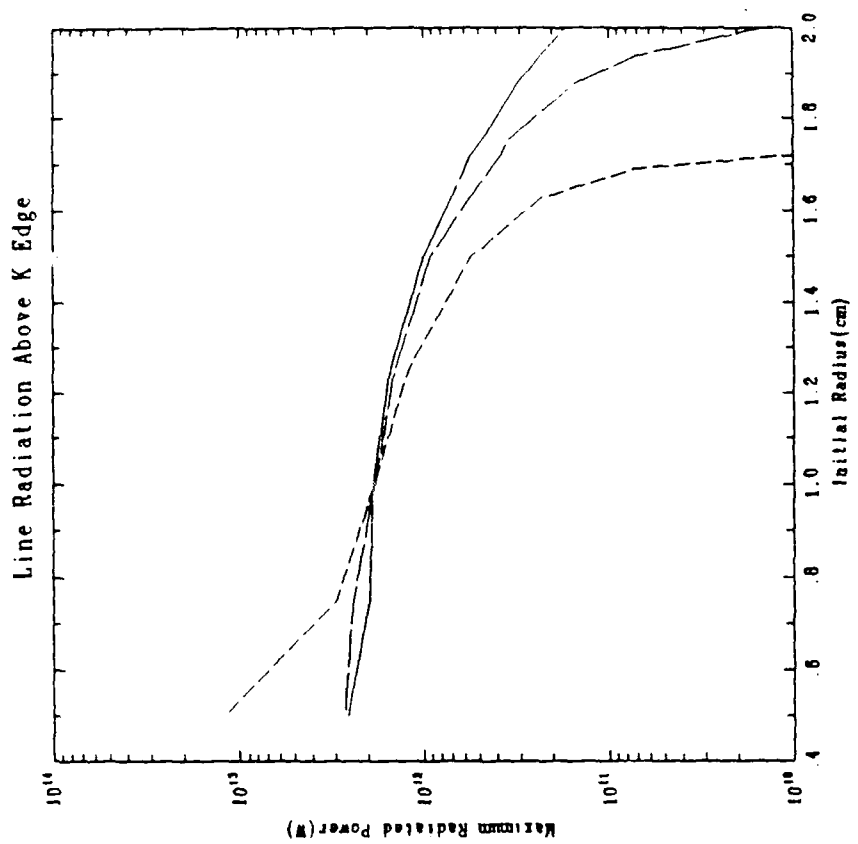


Figure 13(b)

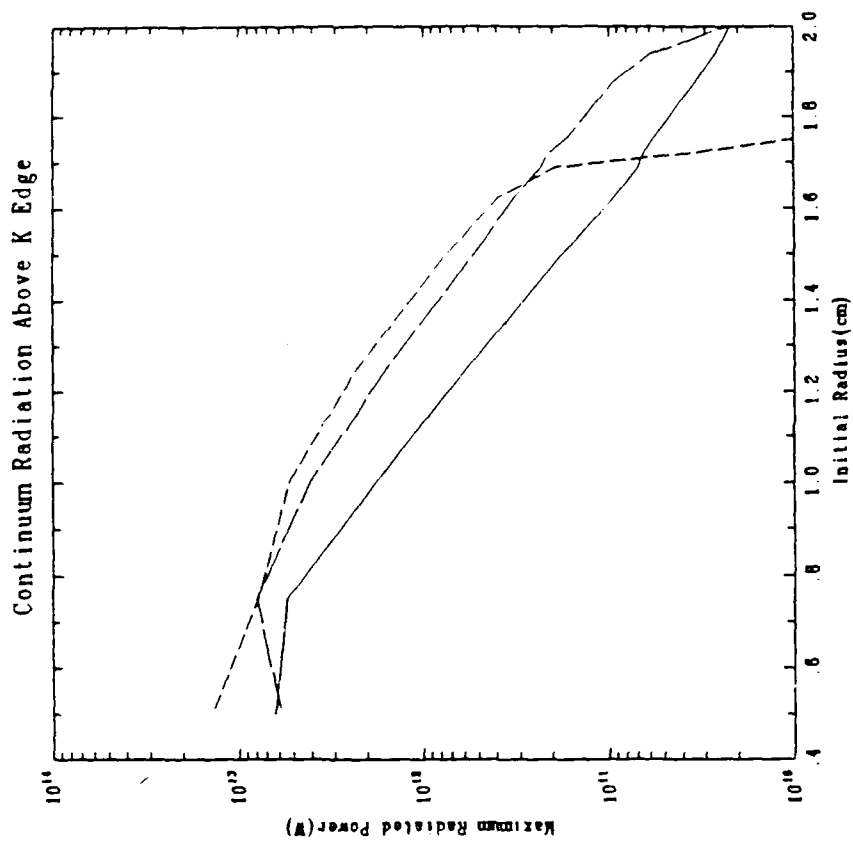


Figure 14(a)

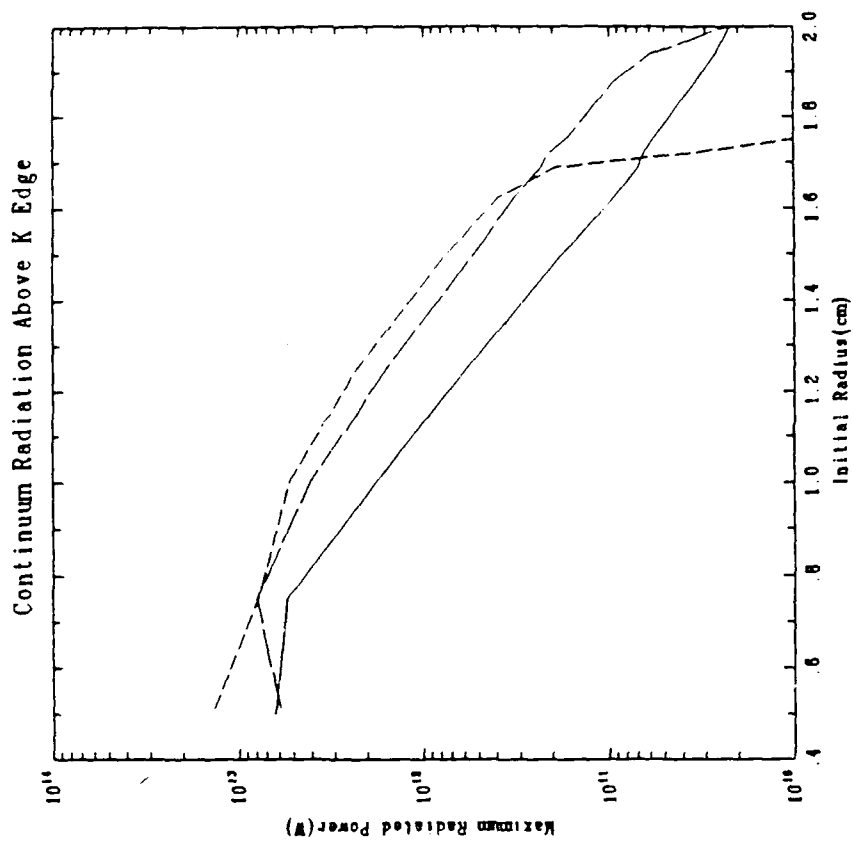


Figure 14(b)

VIII. Modeling the Radiation Hydrodynamics of Mixed Element Pulsed Power Driven Loads

Several years ago two studies were carried out exploring the radiative properties of puff gas mixtures.^{1,2} The results of these studies indicated that it was possible to both enhance the radiative yield and fill-in the spectrum over and above that produced by a single puff gas. However, these investigations were conducted in a static environment for conditions representative of puff gas implosions and could only provide guidance for further, more realistic, studies. Based on these studies there is considerable optimism that conditions conducive to enormous radiative yields can be achieved in pulsed-power driven Z-pinch plasmas by appealing to multimaterial loads. Advances in puff gas technology, in the fabrication of structured targets, and in the theoretical understanding of pulsed power load dynamics have been reported by Physics International, Sandia National Labs and NRL³. Although soft X-ray radiation has been produced in abundance, the K-shell efficiencies which are attainable by this method are modest. In an effort to explore new concepts leading to an enhancement of the K-shell yield a number of load designs are under theoretical and experimental investigation. Recent experiments with concentric gas puffs and with gas puffs imploding onto low density foam plasmas or solid density targets have shown that stable, uniform plasmas can be produced with the pulsed-power technology. In these experiments, the outer plasma, usually a gas puff, is imploded onto the inner plasma, producing a stagnation; the uniformity of the resulting plasma is a consequence of the uniformity of the inner target plasma.

Experiments at NRL include a sodium/neon line coincidence photopumping configuration. Preliminary results⁴ indicate that resonance fluorescence has been produced in the pumped transitions. At Sandia, experiments have been carried out with inert-gas puffs imploding onto structured targets⁵. These targets are thin OH capillaries coated with a low-Z element (such as aluminum) on the outside and a high-Z material on the inside. Physics International has studied neonlike krypton loads using double-puff krypton Z-pinch⁶. Computer simulations of the PI krypton experiment⁷ suggest that substantial soft x-ray yields can be achieved. The NRL and PI results were reported at the Lasers '87 Meeting.

Physics International has also reported⁸ on time-resolved measurements of XUV emissions from recombining neon and aluminum plasmas. Using the DNA/PITHON generator, neon gas puffs were imploded onto aluminum coated parylene capillaries (or onto equivalent mass solid aluminum targets). The implosion heated the Al to form an axial plasma which they estimated to have a density of $\sim 10^{20}$ cm⁻³ and a temperature of ~ 500 eV. Evidence was presented for anomalous brightness in the 4d-3p and 4f-3d lines of Al XI at 150.5 and 154.5 Å and in the 4-3 line of Ne X at 187.3 Å.

Digitized spectra from 3 and 5 cm long, neon/aluminum Z-pinches were compared; the Al lines were confined to the innermost mm or so in radius, while the Ne emissions extended to substantial radii. The 4f-3d and 4d-3p lines of Al XI were seen to be substantially brighter than the 3d-2p line at 98.2 Å and the 4d-2p line at 39.2 Å, even though the latter line was favored by the grating, detector and film response. The intensities of the 4-3 lines relative to the 4d-2p line were significantly higher for the 5 cm pinch; however the continuum background and the emission lines also appear brighter. An alternative explanation for these aluminum anomalies is opacity in the 4-2 transitions; more will be said about this below. In addition, the Ne X 4-3 line appeared to be anomalously bright compared with the 4-2 line at 48.55 Å. However, this latter line was not resolved from the Al XI 3p-2s resonance line at 48.3 Å. A possible contribution to the pumping of the $n = 4$ levels of lithiumlike aluminum is K-shell neon line radiation. The Lyman-alpha and He-alpha lines of Ne are capable of photoionizing Li-like Al; under the right conditions, this photoionization can substantially exceed collisional ionization and result in enhanced recombination to the $n = 4$ levels of Al XI. In a similar way, it is possible for aluminum radiation to photoionize H-like Ne. We studied these mechanisms with the radiation-hydrodynamics model that will presently be described.

Since the implosion and stagnation of plasmas in a Z-pinch can result in a substantial fraction of the total plasma energy being radiated away, it is necessary to treat the hydrodynamics, atomic physics and the transport of radiation in a self-consistent manner. The basic hydrodynamic variables of mass, momentum and total energy are transported in one dimension using a sliding-zone version of flux-corrected transport. A special gridding algorithm

is employed that moves zones in a Lagrangian fashion and adjusts the mesh to resolve gradients in the flow. A single temperature assumption is made, and should be adequate in the stagnation region, where the equilibration time can be of the order of tenths of nanoseconds; the timescale for significant change in temperature is at least an order of magnitude larger.

The complexity of the atomic models for neon and aluminum can be adjusted, depending upon the requirements for accuracy in the diagnostics calculation. The atomic models for neon which were used in this study ranged from 27 levels with 13 lines to over 100 levels with about 300 lines; the aluminum models were comparable in scope. The rate coefficients that are used to calculate the level populations are obtained using atomic calculational methods summarized elsewhere⁹. Inner-shell opacities are included in the model, since these processes are important in the cool, dense plasma regions. Inner-shell photoionization cross sections are calculated as described in Duston et al.¹⁰ and the positions of the ionization-dependent absorption edges in the low density limit are taken from the Hartree-Fock calculations of Clementi and Roetti¹¹.

Radiation emission from and absorption by a plasma are dependent on the local atomic level population densities. Except for optically thin plasmas, the level populations depend on the radiation field, since optical pumping via photoionization and photoexcitation can produce significant population redistribution. Thus, the ionization and radiation transport processes are strongly coupled and must be solved self-consistently. Both probabilistic and multifrequency multimaterial radiation transport algorithms were employed in this study. The probabilistic method forms local angle and frequency averaged escape probabilities for each emission line and for each bound-free process. It is a cost effective method and provides good overall energetics, but it cannot treat certain physical processes such as the photoionization or photoexcitation of one atomic species by another. The multifrequency model breaks each emission line and each bound-free edge into a number of discrete frequencies, and performs a radiation transport calculation at each frequency. The latter method is general and self-consistent, but relatively expensive. Both methods take into account Doppler and Voigt line profiles in the transport of bound-bound radiation.

RESULTS: A number of preliminary calculations were performed with the radiation hydrodynamics model to determine the sensitivity of the results to the initial conditions of the aluminum target. Based on conversations with experimentalists at PI and Sandia Labs, it cannot be ruled out that some fraction of the total current initially flows through the capillary. It is difficult to estimate the temporal behavior of this current or how important it is to the dynamics of the target. Even in its absence, there will be heating and ablation of the outer surface of the capillary due to incident radiation from the imploding gas puff. Two extreme cases with respect to the target can be imagined. At one extreme, it remains cold and solid until the gas puff impacts upon it. In this case, neglecting radiation and thermal transport, the dynamics could be modeled analytically¹²: the target would stay cold, and the gas puff would become hot as the kinetic energy of implosion was converted into thermal energy. A strong shock would propagate out from the target and mark the outer boundary of the stagnation region. In the other extreme, heated by some combination of driver current and radiation from the gas puff, the target rapidly expands; its density is comparable to that of the gas puff when the stagnation commences. In this case, comparable volumes of gas puff and target plasmas become hot.

The preliminary calculations neglected the effects of the driving magnetic field, but instead assigned an initial radial velocity and temperature profile to the puff gas plasma. This allowed us to study the physics of the imploding plasmas in an idealized framework, without the complications of an external driver and coupled circuit. The simulations were performed with a Gaussian neon gas puff having a total mass of 100 micrograms and an initial radial velocity of 4×10^7 cm/sec. Only the stagnation phase of the implosion was modeled in these simulations; thus, the gas puff was initially centered at 1.0 cm (when driven with a B-field, it takes several tens of nanoseconds to implode to this radius). The capillary was taken to be pure aluminum, and the initial density and temperature profiles were varied over a fairly wide range to model the effects of target preheat. The initial configuration for these simulations is shown schematically in Figure 1.

For the extreme case where the target was taken to be solid density initially, the neon puff gas stagnated and heated to several hundred eV, but the aluminum remained cool, substantially less than 100 eV (in the absence of thermal conduction and radiation transport, the analytic solution described above was closely approximated). When the aluminum was taken to be moderately pre-expanded, but still substantially higher in density than the puff gas, radiation cooling maintained the aluminum at a relatively low temperature. Lower initial densities resulted in higher temperatures. When these cases were simulated without radiative cooling, the target temperatures were considerably higher (greater than 100 eV).

The initial configuration that resulted in conditions approximating those reported by PI consisted of a Gaussian target with a peak ion density of $8 \times 10^{20} \text{ cm}^{-3}$ centered at 0.08 cm, with an initial temperature of 30 eV. A time history of the aluminum/neon interface is given in Figure 2. The innermost 1.0 cm of plasma is represented along the horizontal axis, and time (20 to 50 nsec) runs along the vertical axis. Corresponding contours of electron density and temperature are given in Figures 3 and 4. The target density monotonically increases, reaching about $2 \times 10^{20} \text{ cm}^{-3}$ at 50 nanoseconds; it also becomes quite hot (about 500 eV on axis) at about 45 nanoseconds, and then rapidly cools radiatively. These simulations were not intended to model the experiment directly, since no self-consistent magnetic driver was included in the model. They were intended as a test bed for ideas we had about the experiment, including questions about optical pumping of one material by another.

One question concerned possible photoionization of Al XI to Al XII by the K-lines of neon, thereby increasing the recombination rate into the $n = 4$ levels of Al XI. At a few tens of eV, sufficient lithiumlike aluminum would be present, but the collisional ionization rate would be relatively small. Thus, the photoionization rate could exceed the collisional rate if the neon pump source were sufficiently large. The latter consideration required that a substantial fraction of the neon be in the hydrogenlike or heliumlike ionization state. Conditions at 43 nsec looked promising. The temperature of the aluminum was about 36 eV and there was a substantial quantity of neon at about 500 eV. The hydrodynamic profiles at this time are shown in Figure 5. These profiles were post-processed with the multimaterial multifrequency code, described above. Radiation from the neon substantially altered the ionization

state of the aluminum (there was considerably more heliumlike aluminum present when photopumping by the neon was allowed). In addition, some enhancement in the 4f and 4d levels of Al XI was observed. The emission spectrum as calculated by the multifrequency code at this time (43 nsec) is shown in Figure 6, and corresponding optical depths as a function of photon energy are shown in Figure 7. The 4f-3d and 4d-3p lines of Al XI are seen to be comparable with, but not larger than, the 4d-2p line. The corresponding optical depths for these lines can be estimated from Figure 7. Continuum opacity in the vicinity of the 4f-3d and 4d-3p lines is seen to be small (mostly free-free opacity), whereas it is substantially greater in the vicinity of the 4d-2p line (about equally divided between bound-free and inner shell opacity). Although the continuum optical depth is less than unity in the latter case, it will be a very sensitive function of the ionization state of the plasma. The inner-shell opacity (the dashed curve in Figure 7) "burns out" as the plasma ionizes; at this time the 4d-2p line is situated near the threshold for inner-shell burnout. Relatively small changes in temperature can cause large changes in opacity in this neighborhood, and this line could be substantially reduced in intensity. This is one of the factors which makes the interpretation of experimental spectra difficult.

A fully self-consistent simulation was performed with the multimaterial probabilistic radiation model. In this case, the implosion was driven by an magnetic field. A very small amount of current was assumed to flow initially through the outer surface of the capillary; thus aluminum was initially assumed to be solid density, with a finite falloff. The temperature in the aluminum was taken to be about 0.5 eV initially. The neon gas puff was assumed to be a Gaussian centered at 2.0 cm, with a total mass of 100 micrograms. The current was assumed to rise linearly over about 70 nanoseconds to 3 megamperes, and then fall off as a Gaussian with a 40 nanosecond timescale. A time history of the aluminum/neon interface is shown in Figure 8. The innermost 1.0 cm of plasma is represented along the horizontal axis, and time (0 to 100 nsec) runs along the vertical axis. Corresponding contours of electron density and temperature are given in Figures 9 and 10. The aluminum is seen to expand until almost 110 nsec; a low density blowoff develops, and stagnation with the gas puff commences at about 120 nsec, producing temperatures in excess of 500 eV. It should be noted that the simulations described above correspond to the stagnation phase (the final 20 or 30 nsec) of this calculation.

The potential for the photopumping of lithiumlike aluminum by the K-lines of neon appears to be relatively small. From about 120 nsec, a region of cool (a few tens of eV) aluminum persists, but it is rarefied (the electron density is about 10^{18} to 10^{19} cm⁻³). There is substantially less Al XI in this shell than in the case studied above. Furthermore, there does not appear to be a sufficiently strong K-shell aluminum source to produce significant photopumping of the neon. One mechanism which may be important is recombination into the n=4 levels of Al XI and Ne X following rapid cooling of the plasma in the post-stagnation phase. However, cooling times must be sufficiently fast or the plasma will remain in collisional radiative equilibrium and no enhancement over and above the conventional yield will occur. The enhanced brightness in the 4-3 transitions reported by PI might be due to a population inversion caused by rapid recombination. It is more than likely a manifestation of opacity effects. Additional simulations combined with improved experimental diagnostics will have to be done before the measurements can be interpreted and better understood. We will also place the outer puff gas at considerably larger radius from the axis to allow longer run-in times in the hope of obtaining larger implosion speeds and much larger radiative yields (see, for example, K. Whitney, et.al.¹³).

References

1. D. Duston, J. Davis and C. Agritellis, J. Appl. Phys. 57, 785 (1985).
2. J. Apruzese and J. Davis, J. Appl. Phys. 57, 4349 (1985).
3. N.R. Pereira and J. Davis, J. Appl. Phys. 64, R1 (1988).
4. J.P. Apruzese, et al., in Proceedings of the International Conference on Lasers '87 (STS Press, McLean, VA, 1988), p. 37; S.J. Stephanakis et al., IEEE Trans. Plasma Sci. 16, 472 (1988)
5. T.W. Hussey, M.K. Matzen, E.J. McGuire and H.E. Dalhed, Sandia National Laboratory Report No. SAND88-0764, 1988, (unpublished), and submitted to J. Appl. Phys.
6. M. Krishnan, R. Nash, P. LePell and R. Rodenburg, Physics International Report No. PIT-87-02, 1987 (unpublished).
7. J. Davis, R.W. Clark, J. Apruzese and P. Kepple, IEEE Trans. Plasma Sci. 16, 482 (1988).
8. M. Krishnan, T. Nash, and P.D. LePell, IEEE Trans. Plasma Sci. 16, 491 (1988).
9. R.W. Clark, J. Davis and F.L. Cochran, Phys. Fluids 29, 1971 (1986).
10. D. Duston, R. Clark, J. Davis and J. Apruzese, Phys. Rev. A 27, 1441 (1983).
11. E. Clementi and C. Roetti, Atomic Data Tables 14, 177 (1974).
12. H.W. Liepmann and A. Roshko, Elements of Gasdynamics (J. Wiley, NY, 1957), p. 62
13. K. Whitney et al., DNA/PRS Workshop (Kalman Sciences, Alexandria, VA), October 5-6 (1988).

- Fig. 1.** Schematic of initial conditions for numerical simulations in the absence of a magnetic driver. The neon gas puff is given an initial radial velocity of 4×10^7 cm/sec.
- Fig. 2.** Time history of the aluminum/neon interface. Radius from 0.0 to 1.0 cm. is represented horizontally, and time from 20.0 to 50.0 nanoseconds is represented vertically. The outer edge of the neon gas puff moves into view at about 45 nanoseconds.
- Fig. 3.** Electron density contours as a function of radius (0.0 to 1.0 cm) and time (20.0 to 50.0 nanoseconds). Peak density is reached on axis at about 46 nanoseconds.
- Fig. 4.** Temperature contours as function of radius and time. Peak neon temperature occurs near the aluminum/neon interface. The aluminum reaches ~ 500 eV at about 45 nanoseconds, and then rapidly cools radiatively.
- Fig. 5.** Hydro profiles at 43.13 nanoseconds. Radial displacement is given in cm., \log_{10} density in g/cm³, \log_{10} temperature in eV, \log_{10} pressure in 10^{12} ergs/cm³, and \log_{10} velocity in 10^2 cm/nsec.
- Fig. 6.** Emission spectrum at 43.13 nanoseconds. The instantaneous power (ergs/sec-cm-keV) is given as a function of photon energy (keV). Selected emission lines are identified.
- Fig. 7.** Optical depths at 43.13 nanoseconds as a function of photon energy (keV). The contributions of free-free opacity (ff) and inner-shell opacity (is) are indicated. Total optical depth includes contributions from free-bound and bound-bound processes.
- Fig. 8.** Time history of the aluminum/neon interface with B-field driver. Radius from 0.0 to 1.0 cm runs horizontally, and time from 0.0 to 136.0 nanoseconds runs vertically. The outer edge of the neon gas puff moves into view at about 120 nanoseconds.
- Fig. 9.** Electron density contours as a function of radius (0.0 to 1.0 cm) and time (0.0 to 136.0 nsec) with B-field driver.
- Fig. 10.** Temperature contours as function of radius and time with B-field driver.

Neon-Aluminum Initial Configuration

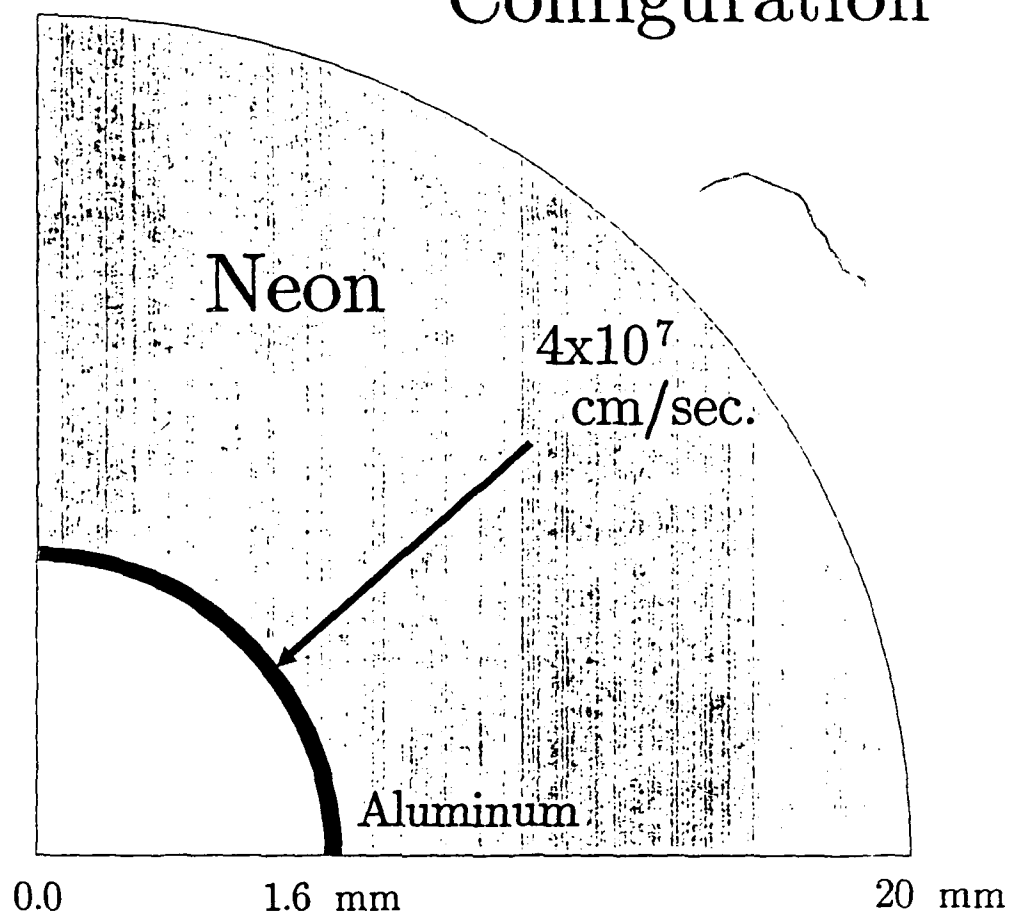


Figure 1

ALUMINUM/NEON: interface

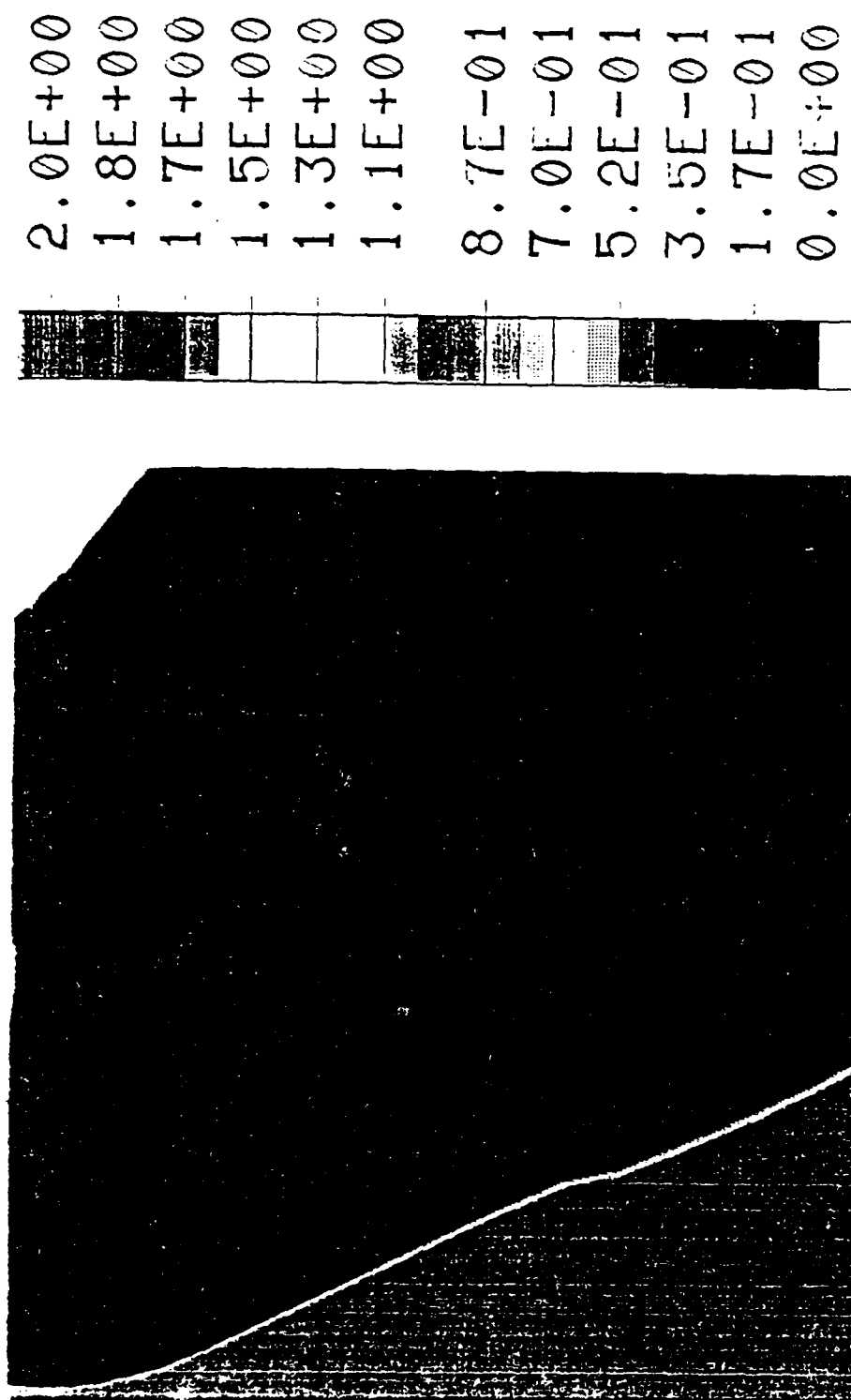


Figure 2

ALUMINUM/NEON: electron density

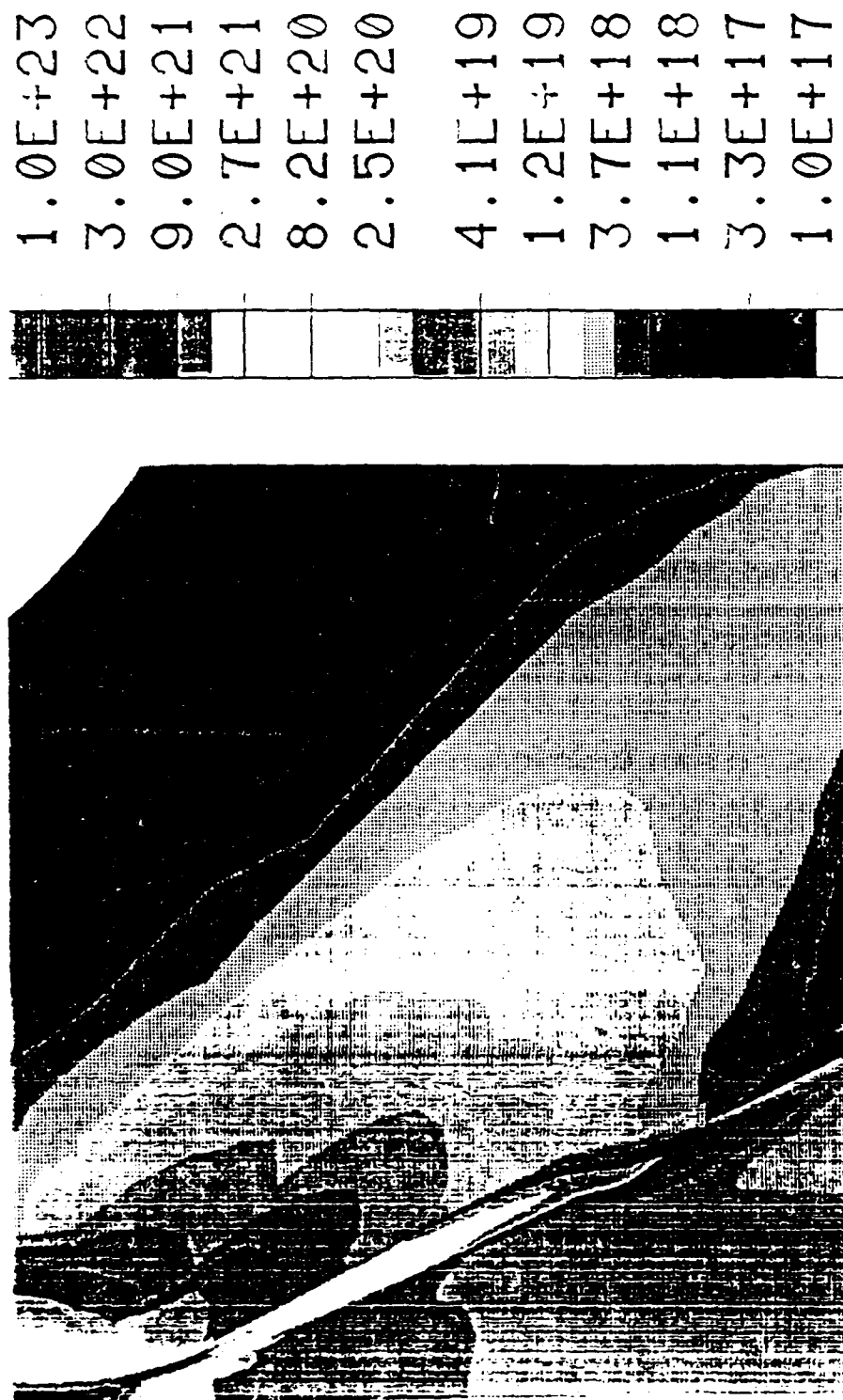


Figure 3

ALUMINUM/NEON: temperature



Figure 4

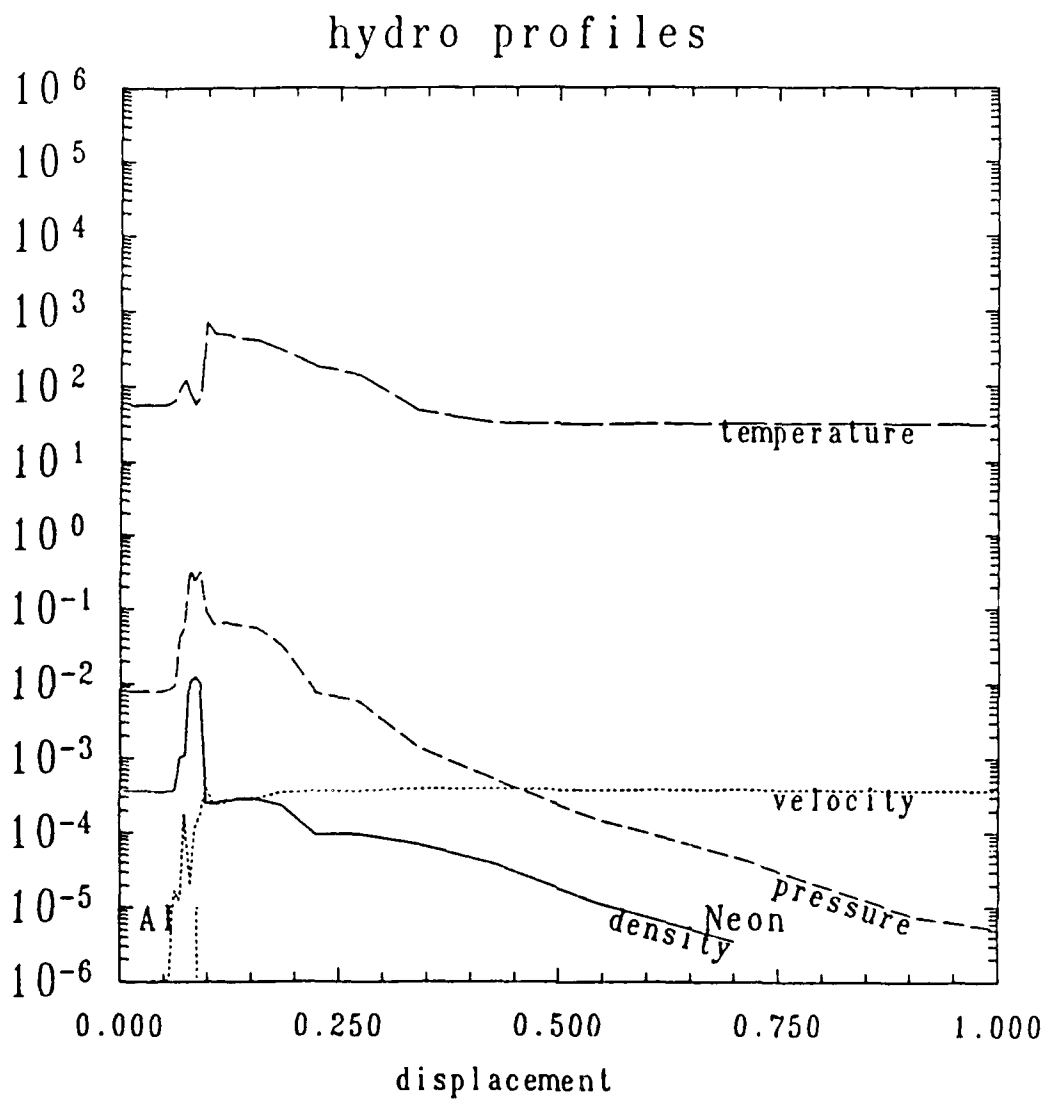


Figure 5

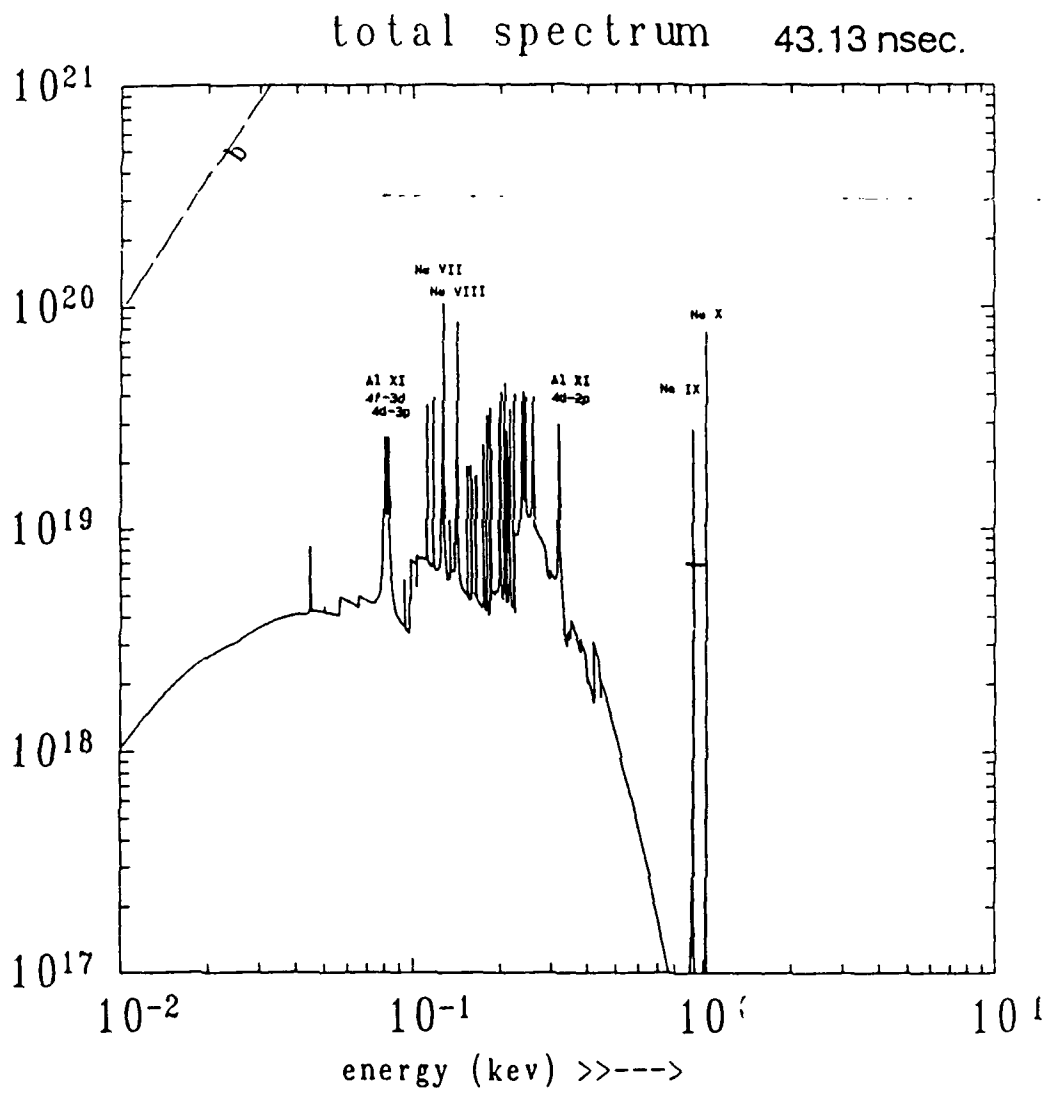


Figure 6

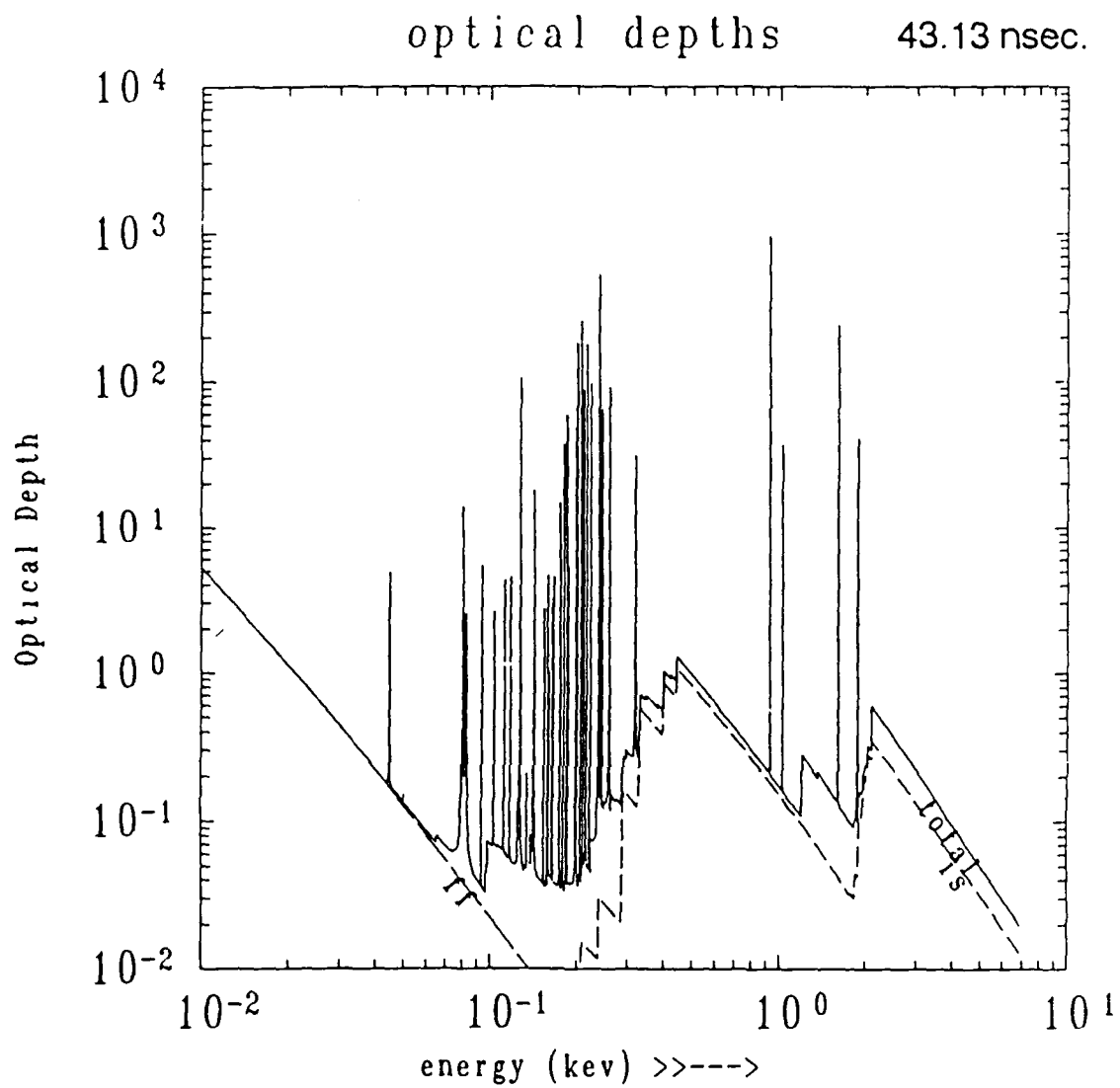


Figure 7

ALUMINUM/NEON: INTERFACE

1.1E+00
1.0E+00
9.1E-01
8.1E-01
7.2E-01
6.2E-01
4.3E-01
3.8E-01
2.9E-01
1.9E-01
9.6E-02
0.0E+00

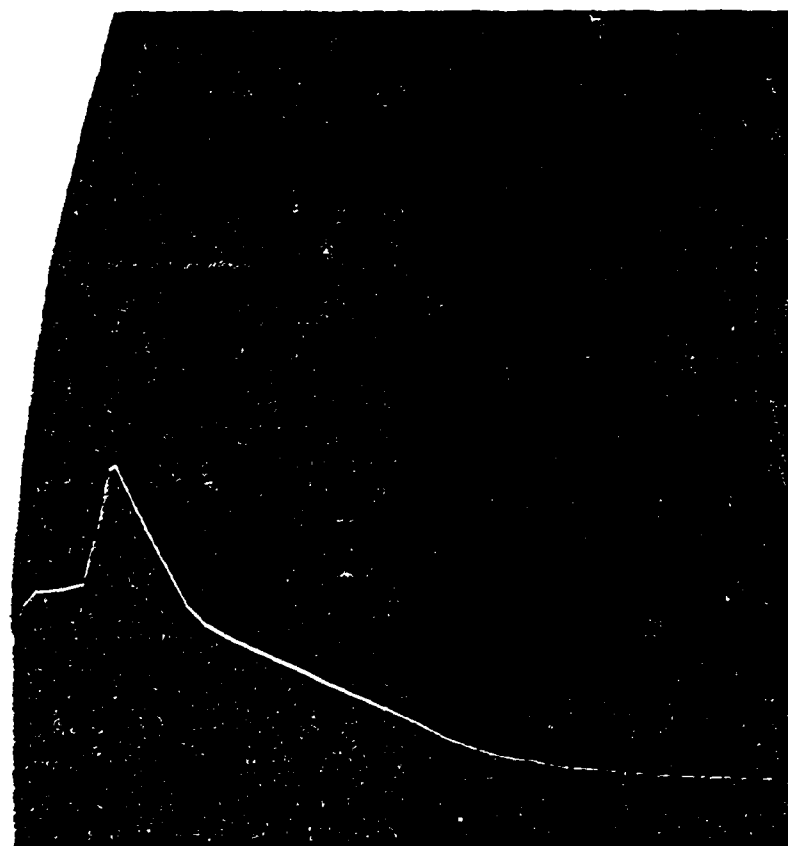


Figure 8

ALUMINUM/NEON: ELECTRON DENSITY

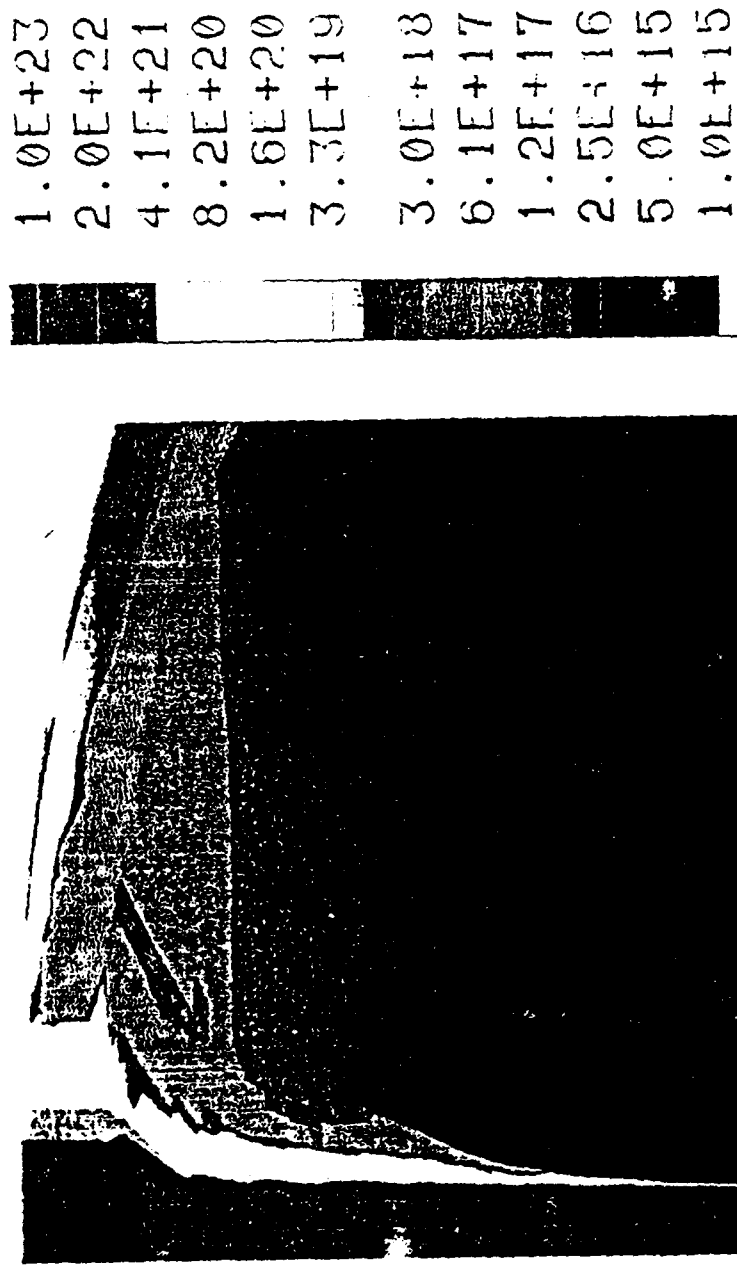


Figure 9

ALUMINUM/NEON: TEMPERATURE

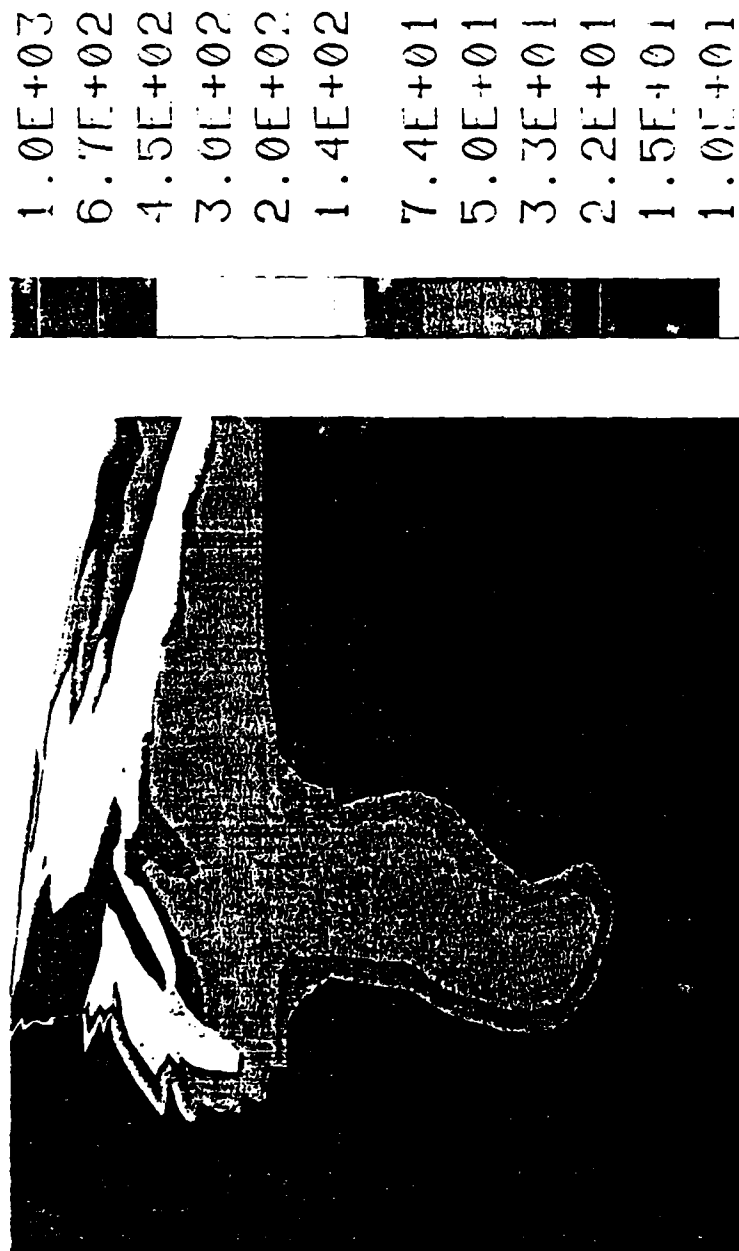


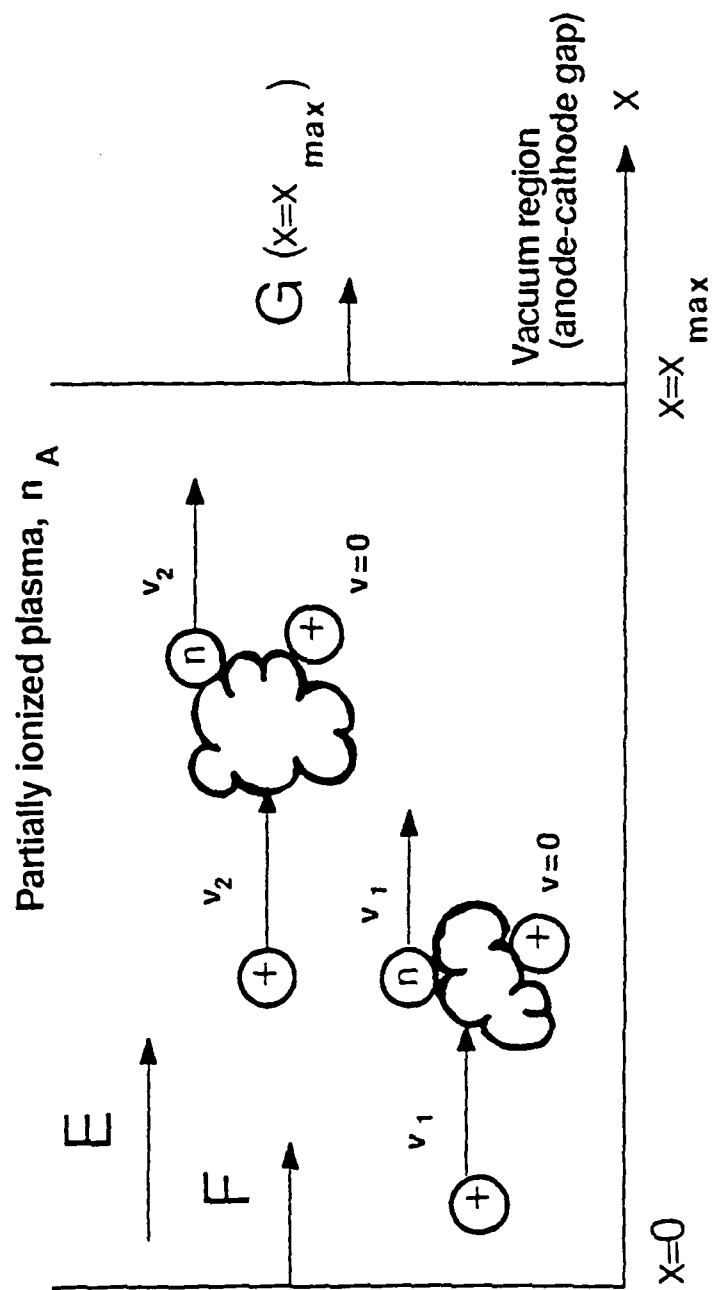
Figure 10

IX. CHARGE EXCHANGE NEUTRAL SIMULATION FOR A REFLEX SWITCH

When a reflex switch^{1,2} opens prematurely, less power is delivered to the load. Thus, if we can understand why the switch opens early, we can take preventive measures that would in turn increase the efficiency of the energy transferred to the load. A possible explanation for premature opening is that energetic neutrals fill the anode-cathode gap, causing electrical breakdown and shorting out the gap. These neutrals are produced by ions charge-exchanging as they are being accelerated through the partially ionized anode plasma. In the discussion below we will describe the model in detail, then present some results from simulation.

The charge-exchange model as envisioned by Prono et al.³ is given in figure 1. Ions are injected at the left hand boundary and the ion flux is F , where F has the units of number of particles per unit area per time. Since this one dimensional problem is assumed to be in a steady state, the ion flux has the constant value F throughout the region $0 < x < x_{\max}$. There is also a constant applied electric field E , again for $0 < x < x_{\max}$, and the partially ionized plasma, which contains mostly neutrals, has the uniform density n_A . It is with these neutral atoms that the ions undergo charge-exchange. Again referring to figure 1, we see that an ion is accelerated by E , then charge-exchanges, creating a fast neutral with the same velocity and an identical ion at rest. This process can be repeated over and over, so one ion can produce many energetic neutrals. This means that we have a flux of neutrals throughout the entire background gas region, and there is a neutral flux into gap region, given by $G(X=x_{\max})$. It is this flux into the gap region, as mentioned previously, that causes premature switch opening.

By using the one-dimensional Boltzmann equation, Prono et al.³ found both the ion and neutral distribution functions, which were then used to find the neutral and energy fluxes. However, because they used a charge-exchange cross section that decreased with energy, this created some mathematical difficulties, which caused them to give only approximate solutions. Since we wanted these analytical results to be used in benchmarking a computer code, that will be presented later, we



Charge Exchange Model

Figure 1

decided that exact results were needed to reduce the errors in our comparisons. So we made the less physical assumption that the charge-exchange cross section σ , was constant for all energies, but in doing so we obtained exact analytical solutions. For completeness we give some of these results below,

$$G(x) = \left(\frac{x}{\lambda}\right) \cdot F \quad (1)$$

$$\langle E_n \rangle = (qE\lambda) \left[\left(\frac{\lambda}{x}\right) (e^{-x/\lambda} - 1) + 1 \right] \quad (2)$$

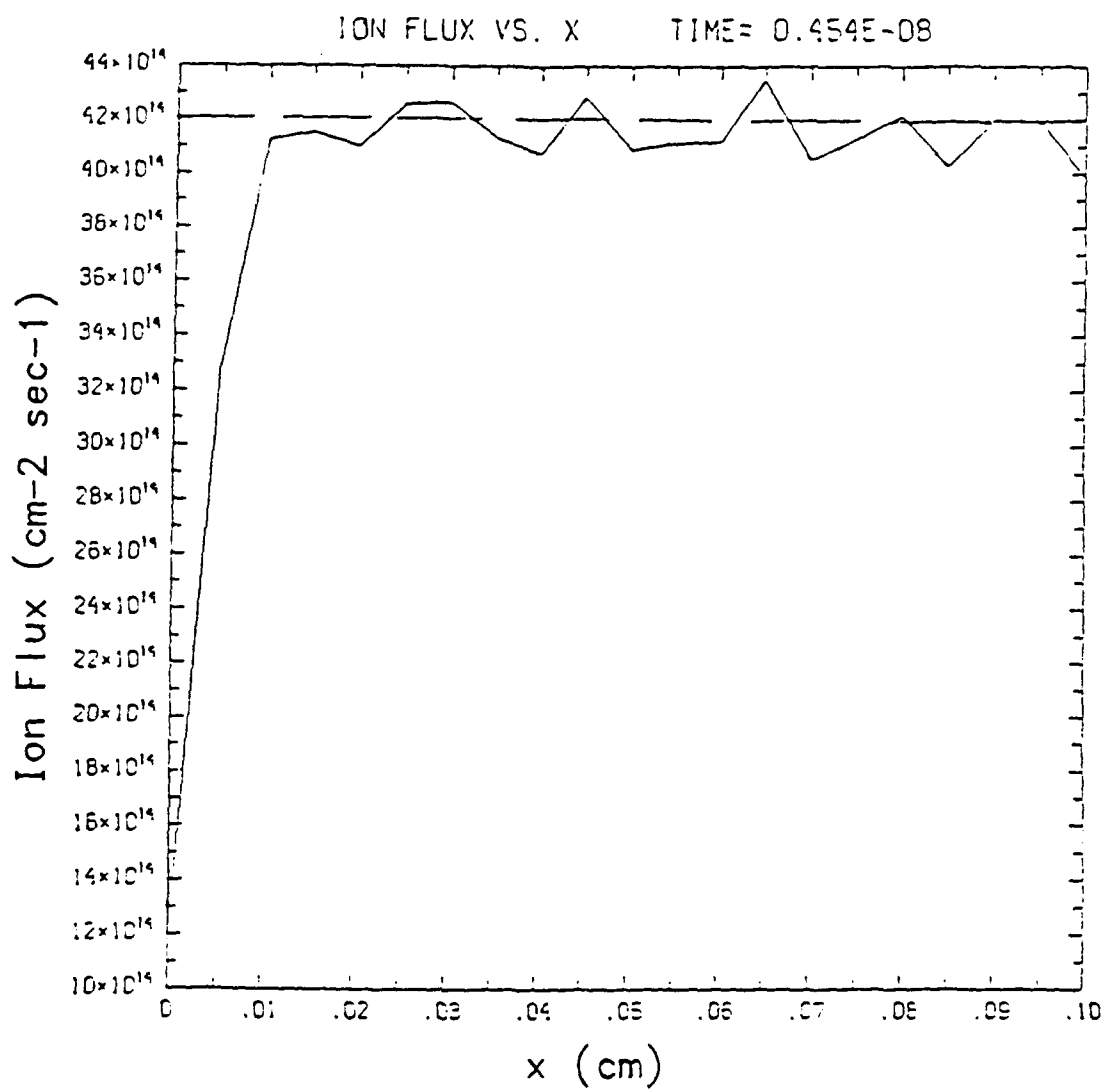
$$g(w, x) = \frac{mF}{qE\lambda} e^{-w/qE\lambda} H\left(x - \frac{w}{qE}\right) \left[1 + \frac{1}{\lambda} \left(x - \frac{w}{qE}\right) \right] \quad (3)$$

$$\int_0^{x_{\max}} g(w, x) dx = \frac{mF}{qE} \left(\frac{x_{\max}}{\lambda}\right) \left(1 - \frac{w}{qEx_{\max}}\right) e^{-w/qE\lambda} \left[1 + \frac{x_{\max}}{2\lambda} \left(1 - \frac{w}{qEx_{\max}}\right) \right] \quad (4)$$

where q is the charge of the ion, w is the kinetic energy, and λ is the mean free path for charge-exchange, given by $\lambda = 1/n_A \sigma$. The quantity $\langle E_n \rangle$, equation (2), is just the average neutral energy. Note that the neutral flux profile $G(x)$ has a simple linear relationship, and that $g(w, x)$ is the neutral distribution function, the number of neutrals per unit volume per unit velocity.

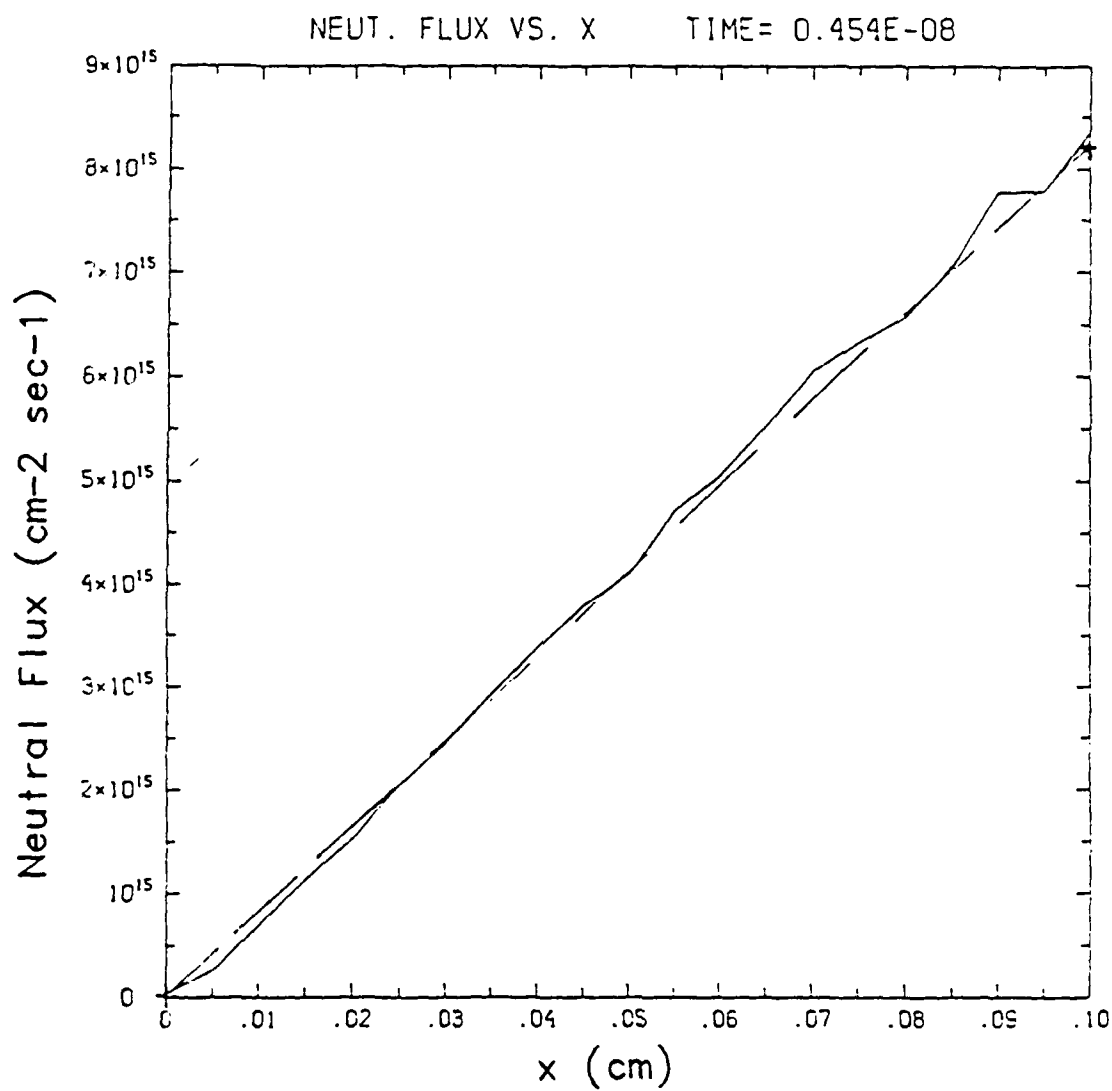
To simulate the charge-exchange problem, the code neutral was written. NEUTRAL is a time dependent Monte Carlo code and is the final member in a series of codes that varied in their degree of complexity. By monte carlo we mean that a given event (charge-exchange) is determined randomly. NEUTRAL was written so that one can consider a constant or self-consistent electric field, which has not been tested. NEUTRAL can also handle the general case where the neutral background density depends on position and the charge-exchange cross section depends on energy, a situation that certainly is analytically intractable.

We ran the code NEUTRAL to simulate the charge-exchange problem as envisioned by Prono et al. We considered protons exchanging with



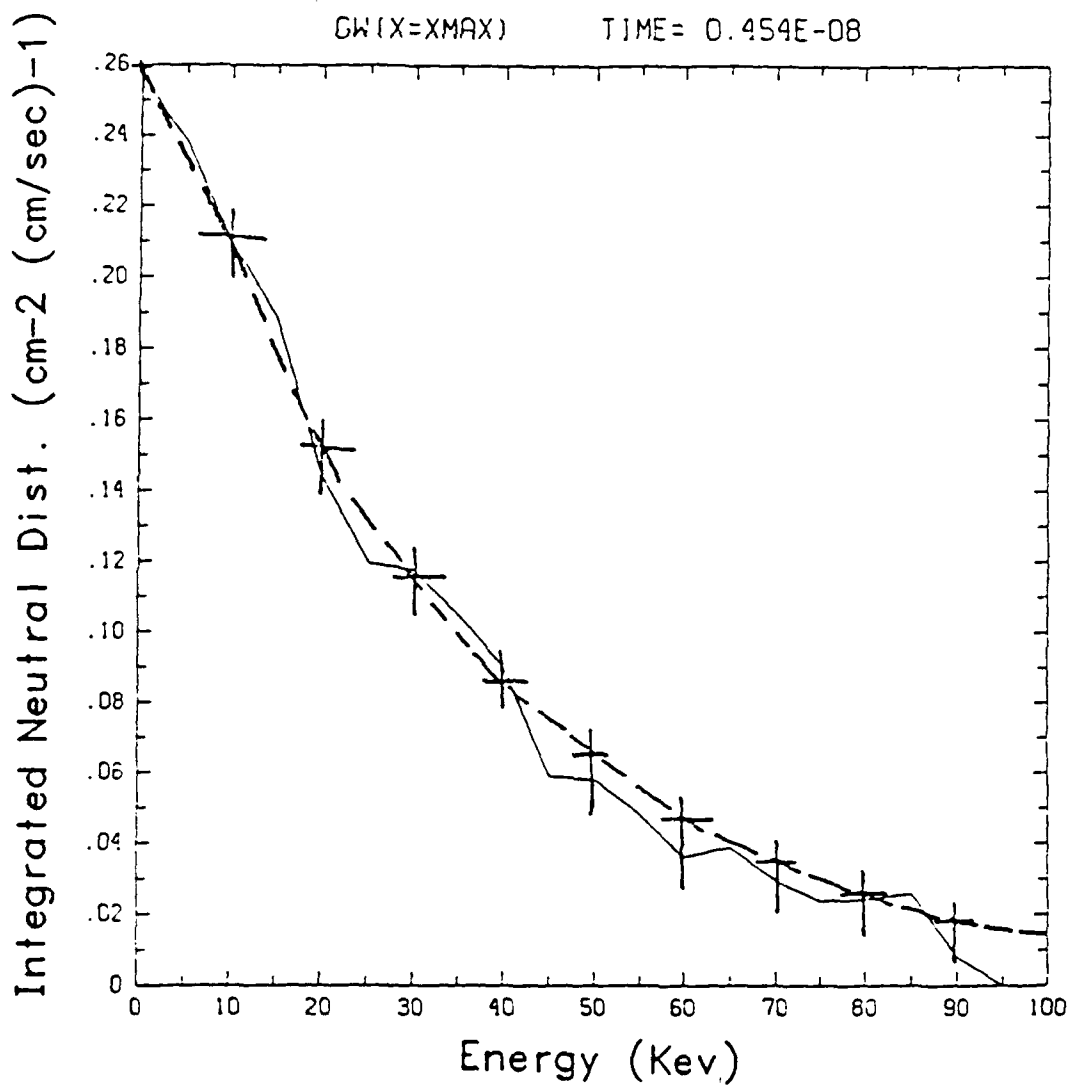
Ion Flux as a Function of x

Figure 2



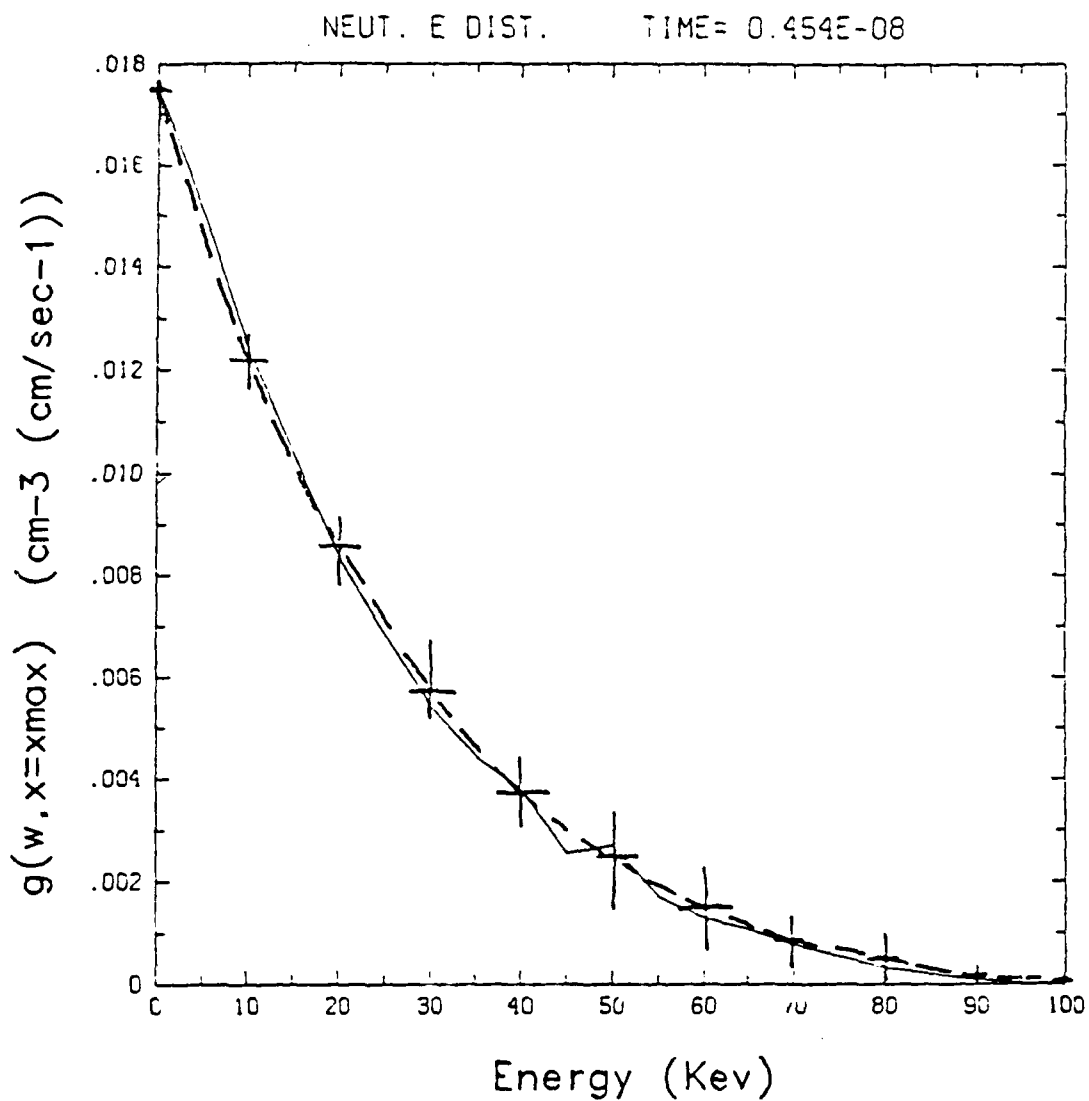
Neutral Flux as a Function of x

Figure 3



Integrated Neutral Distribution as a
Function of Energy

Figure 4



Neutral Distribution at the Vacuum Interface
as a Function of Energy

Figure 5

hydrogen gas and $E=1$ MV/cm, $\lambda=5.0 \times 10^{-2}$ cm and $x_{\max}=0.1$ cm. Some of the code results are given in figures 2-5. From figure 2, we chose $F=4.2 \times 10^{15}$ cm $^{-2}$ sec $^{-1}$, the dashed line, to be used in equations (1) - (4). In figures 3 through 5 the dashed curves are the exact solutions, and are to be compared to the simulation results. In figure 3, the neutral flux as a function of x , there is very good agreement between the code and $G(x)$, equation (1). In figure 4, which is the integrated neutral distribution vs. w , see equation (4), we see once again that the code agrees quite well with theory. In figure 5 we compare the neutral distribution function at $x=x_{\max}$, or $g(w, x=x_{\max})$ as a function of energy w . We see that the comparison is quite good, except near the tail. This may be due to statistics or an error in the code plotting logic. So, in general, at least for this benchmark case, NEUTRAL has performed very well.

Summary and Conclusions

The premature opening of the reflex switch can be explained by energetic neutrals filling the anode-cathode gap, which causes electron breakdown and hence shorting of the gap. Thus it is essential that we must first determine the flux and velocity distribution of the neutrals into the vacuum gap. We have written a code named NEUTRAL which finds these neutral profiles by simulating the charge-exchange model as given by Prono et al. We have compared the code results, such as the neutral flux and the neutral distribution function at the gas-vacuum interface, to exact analytic solutions, and we have found very good agreement for this benchmark case.

The code NEUTRAL is just a first step in the complete understanding of the premature gap shorting problem. We plan to use the results of NEUTRAL as input to a simple neutral gas breakdown model, yet to be determined, for the vacuum gap. And because physical parameters, such as density and electric fields, are unknown in a reflex switch, we will do a parameter study using NEUTRAL. From this study we will be able to offer some guidance and proposals to experimentalists on ways to increase the time before the gap closes. Some possible suggestions might involve operating voltages and anode

design and composition. One may even be able to use the code as a diagnostic tool. For example, by comparing the code result to experimental measurements one could try and infer the conditions inside the anode plasma. In addition, we will use NEUTRAL, modified to handle a linearly time varying electric field, to model experimental evidence from Physics International on the relationship between gap closure-time and gap spacing.

References

1. L. J. Demeter in Opening Switches, ed. by A. Guenther, M. Kristiansen and T. Martin, Vol. I, Plenum Press, N.Y., (1987), pg. 177.
2. J. M. Creedon, L. J. Demeter, B. Ecker, C. Eichenberger, S. Glidden, H. Helava, and G. A. Proulx, J. Appl. Phys. 57, 1582 (1985).
3. D. S. Prono, H. Ishizuka, E. P. Lee, B. W. Stallard, and W. C. Turner, J. Appl. Phys. 52, 3004 (1981).

ELECTRON SCATTERING IN A REFLEX SWITCH

In the closed mode of the reflex switch^{1,2} electrons must repeatedly traverse (reflex) through an anode foil. Of course, as these electrons pass through the foil, they scatter and lose energy until they are absorbed. Because the theories³ involving the operation of the reflex switch depend on the reflexing electron population at the anode, it is important that electron scattering be included in the modeling of the reflex switch. In the discussion below we will discuss Moliere's theory of small angle multiple scattering and then present the theory's implementation in a Monte Carlo module, in the particle-in-cell code REFLEX⁴.

Our criterion in evaluating the various scattering theories was that the model should not be too computationally intensive, and should be reasonably accurate. This is because the scattering routine will be combined with a particle-in-cell module. Using these basic criteria, we determined that the small angle multiple scattering theory of Moliere was adequate⁵. By small angle multiple scattering we mean that an electron will undergo many (>20) small angle deflections as it passes through the scattering medium. From the simplified derivation of Bethe⁶, we find taking only the first term in the distribution function expansion, that

$$f(\theta)\theta d\theta = 2e^{-\theta^2/(X_c^2 B)} \theta d\theta \quad (1)$$

Where $f(\theta)$ is the scattered electron distribution and θ is the scattering angle relative to the incident direction. The quantity X_c , is defined as the angle such that the total probability of single scattering greater than X_c is one. The real number B is defined by the transcendental equation,

$$\frac{e^B}{B} = \frac{X_c^2}{1.167X_\alpha^2} \quad (2)$$

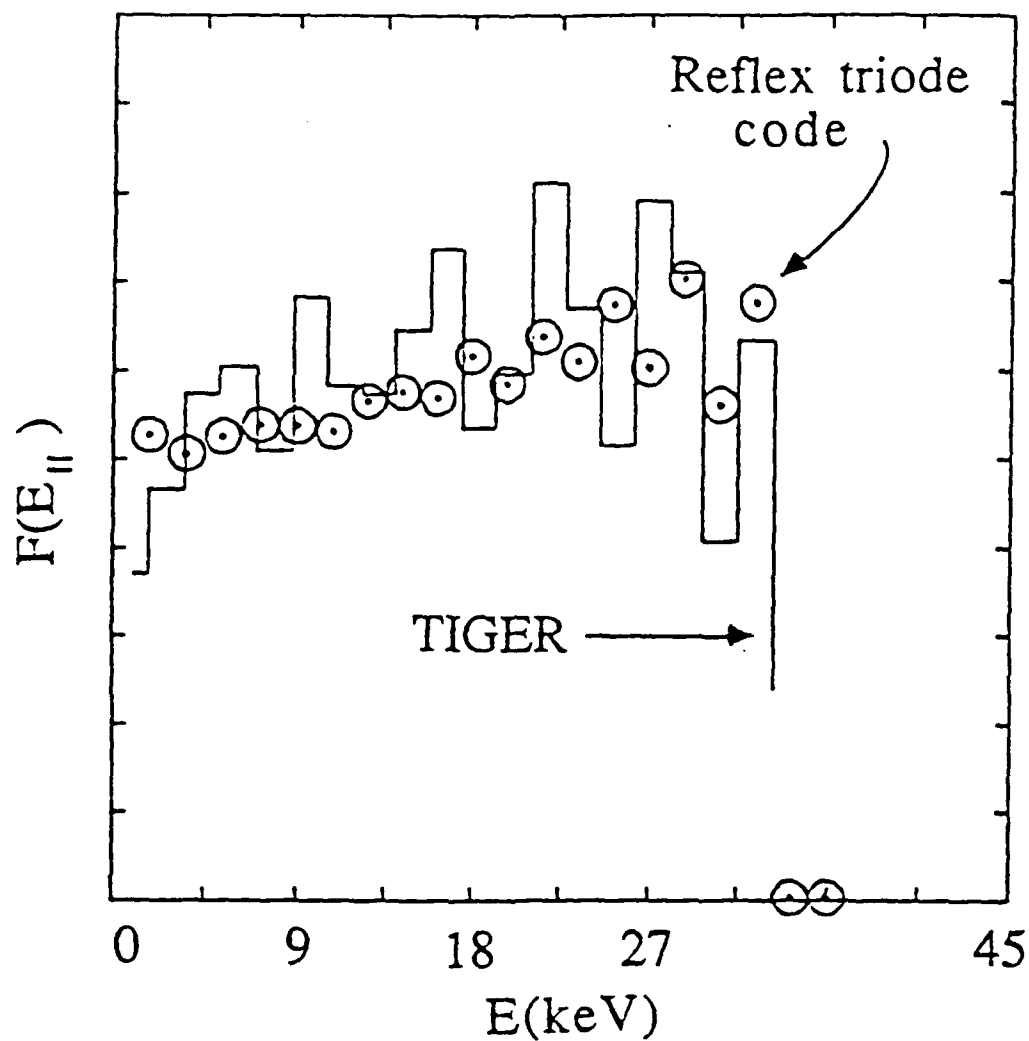
where $X_\alpha^2 = X_0^2 (1.13 + 3.76 \alpha^2)$.

The angle X_0 , is the minimum cut-off angle, and α depends linearly on the atomic number of the scattering atoms, and inversely on the incident electron's speed. We note at this point, from equation (1), that $X_c^2 B$ is the so called width of the gaussian. Both (1) and (2) are essentially the results utilized in the scattering algorithm given below.

As was mentioned above, the scattering algorithm for implementation in the particle-in-simulation needed to be reasonably accurate and have simple distributions to sample from, such as equation (1). We also demand that the algorithm be largely vectorizable, in order to further increase computational speed. We assume that the initially high energy electrons do not scatter at all in the thin foil, and that we can simulate the electron energy loss and scattering independently, which is important in making the algorithm vectorizable. We also assume that the electron loss can be described by the continuous slowing down approximation.⁵

Using equation (1) and (2), and the previous assumptions, the algorithm proceeds as follows. First, for a given set of incident energies, table are precomputed for the energy loss and the Moliere scattering widths. Next when a particle (electron) passes through the anode foil, the energy is decremented by using the energy loss table. Then a random number is generated, and using the appropriate Moliere width, we find the spherical polar scattering angle θ . Also an azimuthal scattering angle ϕ is found. Once these angles are found, the particle's velocity is rotated. This process, energy loss to scattering, is done for every pass through the anode foil until the particle is absorbed.

This simplified monte carlo scattering routine was benchmarked against the standard Monte Carlo code TIGER for 35 KeV electrons



Parallel Energy Distribution as a
Function of Energy

Figure 1

repeatedly scattered through a 2 micron thick carbon foil until they are absorbed. Figure 1 compares the, parallel to the incident direction, kinetic energy distributions. We see that the comparison is reasonable, and this gives us confidence in our simulation model. Also, timings indicate that the module can process over a million particles in approximately 2 seconds on a Cray XMP. Thus the algorithm is well suited to work within REFLEX.⁵

Summary and Conclusions

From the considerations of accuracy and speed it was determined that Moliere's theory of small angle multiple scattering, using only the first term in the expansion, was to be used in a monte carlo scattering module, which then would be implemented in the particle-in-cell code REFLEX. Benchmarking the module against the standard Monte Carlo code TIGER, we found reasonable agreement, which shows that the module is working correctly and can be implemented in the REFLEX code.

References

1. L. J. Demeter in Opening Switches, ed. by A. Guenther, M. Kristiansen and T. Martin, Vol. I, Plenum Press, N.Y., (1987), pg. 177.
2. J. M. Creedon, L. J. Demeter, B. Ecker, C. Eichenberger, S. Glidden, H. Helava, and G. A. Proulx, J. Appl. Phys. 57, 1582 (1985).
3. D. S. Prono, J. M. Creedon, I. Smith, and N. Bergstrom, J. Appl. Phys. 46, 3310 (1975).
4. J. Ambrosiano and J. Geary, "A One-Dimensional PIC-Circuit Code For Simulating a Reflex Triode," Berkeley Research Report, BRA 89-W014R, Berkeley Research Associates, VA, Sept. 1988.

5. J. Les and J. Ambrosiano, "Electron Scattering in a Reflex Switch Foil," Berkeley Research Report, BRA 89-W018R, Berkeley Research Associates, VA, Sept. 1988.

6. H. A. Bethe, Phys. Rev. 89, 1256 (1950).

X. Continuum Theory of the Reflex Triode

Introduction

The reflex switch (RS) concept¹ and its present implementation at Physics International on the EYESS device² represent an important option on the path to a higher dose ("x10") simulator based upon plasma switching and modern inductive store technology. As one element in a modular array, which is the FALCON upgrade to EYESS, a reflex switch provides several clear advantages as a bremsstrahlung load.

Unique in the spectrum of opening switch concepts, the reflex switch offers the possibility of triggering the opening phase to control the overall synchronism of the simulator. The basic triode construction (and even its more elaborate variations) has an attractive simplicity when compared to the complex source hardware for plasma erosion opening switches, density controlled opening switches or plasma filled diodes. In common with the plasma filled diode the reflex switch is its own load and thus minimizes the inductance "downstream" of the opening switch, a property long known to be helpful in any inductive store concept.

There are two principal concerns in bringing the switch into routine use. A relatively minor problem is the requirement for an axial magnetic guide field, which leads to auxillary coil and shielding hardware. The more critical problem is the fact that the larger currents demanded in the "x10" machine are neither presently achievable nor credibly implied by the heretofore successful scaling laws. It is a fair assessment that the device stands or falls on the success of present efforts to

understand and control or remove the presently observed "anomalous gap closure", which limits the peak conduction phase current.

The physics that determines the upper current limit for the conduction phase is not fully understood at present, nor is the basic operational concept necessarily accepted among many in the DNA community. The theory developed seeks (i.) to establish a more complete physical basis for the Reflex Switch operation, (ii.) to refine, in the context of real devices, some of the classical notions held from early equilibrium theory and, (iii) to provide some conceptually simple models which allow estimates for the effects of "anomalous gap closure" and competing, hypothetical opening mechanisms on the predicted device waveforms.

Therefore we addressed, using a quasi-steady state Vlasov formulation, some important questions which arise in connection with the Reflex Switch:

- Does charge exchange with neutrals provide the rapid gap closures observed; how can one derive and improve the observed scaling laws?
- What are the fundamental limits on the current density? Are they determined by the electrode physics, microinstabilities, or electron neutral collisions?

While definitive answers cannot be provided as yet, the framework to develop partial answers can be constructed and some first estimates on the path to these goals have been extracted. Three ingredients were prerequisite.

We first built an extension of the "classical" theory to develop those ideas needed in connecting the steady state, single particle Vlasov metaequilibria to slow timescale changes in the boundary conditions and reflexing spectra. Next we showed the development of a circuit model which addressed the initial current buildup phase and the transition from low to high impedance. With some simplified results of the more complicated models, the circuit model was used to make a comparison to

experimental data for the MOSES and EYESS parameters.

Phenomenology of the Reflex Switch

Present Reflex Switch devices are generally triode systems³, operated on the early phase of the current pulse discharging energy into the storage inductor. The triode first presents a high voltage to the driver as the electron population builds up and begins to oscillate (reflex) through the foil anode. Those electrons transiting the primary gap (the so-called AK1 gap) at high energy are stopped by the secondary cathode and begin to charge it negative relative to the anode. This process continues until there is a detailed balance between received and re-emitted electron current and a floating potential is established on the secondary cathode K2. This floating potential usually exhibits one or more positive voltage steps during the conduction phase, perhaps due to bursts of ion current. Yet, so long as there exists a voltage on the AK2 gap which is less than that required to boost a re-emitted electron to a one range energy in the foil anode⁴, viz. $\leq -10\text{kV}$, the reflex electrons can continue to populate a spectrum of energies above that required for capture and thereby enhance the ion emission from the anode.

It is the ion emission that is the key to the low impedance state which then develops after a few tenths of μs . For, while the ion current is relatively small (particularly for the true triode geometries), the ion space charge in the gap neutralizes the primary electron space charge and shortens the effective gap spacings near each electrode. The emission is thus many times enhanced over that expected from a bipolar Child-Langmuir⁵ analysis of the original gap.

The low impedance state would persist forever (in principle) but always falls prey (in practice) to some catastrophe associated with the movement of the floating conductor nearer the anode potential. The primary problem for the Reflex Switch,

in the context of pulse power engineering for the "x10" machine, is that the opening phase occurs too soon in the driver pulse and fails to follow previously observed conduction time scalings, based on the notion that charge exchange neutrals fill the triode and short the gaps. As noted above, the future utility of the device stands or falls on the success of present efforts to understand and control or remove this so-called "anomalous gap closure" limitation.

Results and Conclusions from the Equilibrium Vlasov Model

When viewed in the context of the analytical theory and the REFLEX particle code work documented in the NVOO proceedings⁶, the qualitative picture of the reflex switch which arises is both simple and compelling. The device operates at an enhanced current density because neutral plasma plays the role of a conducting medium that effectively shortens the initial gap spacing to two smaller gaps (for a triode) as reflexing electron flux builds up. Each basic notion of the "classical" Reflex Switch model can be partially substantiated by these diverse theoretical approaches and by experiment. Taken as a whole these results show the device to be based on solid physics, but clearly not understood well enough (as yet) to be certain it can fulfill its intended role. We have detailed three points of sensitivity possessed by the reflexing state: ion charge exchange, electron drag from either turbulence or neutral interaction, and ion emission boundary conditions. Each of these may operate along with the "classical" opening mechanism, viz. the shorting of K2 to A, in determining the opening time and, hence, the maximum current.

Several modification to the "classical" picture are implied by our new formulation, in particular

- η_{crit} is coupled to Ψ_0 and no longer is purely a function of voltage;

- High current, low impedance equilibria persist until the A-K2 potential is less than a range energy $\approx 10\text{keV}$;
- The triode phase space is especially unstable, but the K2 potential will work to keep the hole open;
- The spectral convolutions are simplified and can often be performed analytically, yielding quantitative agreement with the observed current enhancement β .

We have found that the reflexing state is potentially susceptible to the starvation of ion current due to charge exchange or the decay of reflexing electron flux due to electron neutral collisions. If such sensitivity does indeed occur in the laboratory, this would result in a rapid increase in impedance. No experiments yet fielded can preclude any of these ideas but these mechanisms can be quantified with some effort and can help to understand the opening process. The present work also points up very concrete avenues of approach to the additional answers we seek by

- i. fixing, through an evaluation of the charge exchange neutral fluxes, the gap breakdown times and rates of impedance collapse,
- ii. incorporating, from the particle code, estimates of turbulent drag and ion sweepout rates.

Moreover, these additions can be tested in a relevant and cheap circuit model to gain insight and to suggest future experiments. The circuit model clearly operates around the experimentally observed current and voltage traces – without benefit of any free parameters.

Evaluating the Ion Charge Exchange Neutral Flux

What governs the behavior of charge exchange neutrals in a typical reflex switch triode? To be sure large electric fields near the electrode surfaces must do the work required to extract the ion fluxes required to support, in turn, the low impedance state of the conduction phase. The spatial structure of these fields will exhibit a complex dependency on the surface hydrodynamic evolution because the decomposition of the anode in particular into a cloud of metal droplets, vapor, and plasma is unavoidable at the power densities characterising the operating point. A detailed fluid model, including sheath and presheath effects, will be required to unravel these details well enough to guide future experiments. In our recent work⁷ the attempt is made only to explain the observations to date and to answer a few simple questions, in the context of a fixed neutral layer and surface electric field which are of the expected order of magnitude.

- How fast can one expect charge exchange neutrals to get?
- Can one derive or improve the observed scaling laws?
- How well does this picture describe the rapid gap closures observed?

A Monte Carlo code has been developed which treats the ion charge exchange process through a given background of neutral gas. The model benchmarks well to the correct linear spatial dependence of neutral flux in the case of constant cross section and E field.

The input required is a neutral density spatial profile, an electrostatic potential function or E field, a flux of hot ions, and the appropriate charge exchange cross section⁸

The calculation reported here uses a Maxwellian population of injected ions, the

energy dependent cross section for H, and is done in the limit that $\lambda_{mfp} \gg \lambda_{Debye}$. The output is a neutral flux profile and energy distribution which can be used as a first step in calculating the closure rate scaling laws.

The scaling of the neutral velocity with electric field is seen to be

$$v_n \sim E^{\frac{1}{2}} = d_{AK1} \propto \dot{I} \tau_{close}^{\frac{3}{2}}$$

when we use a neutral density: $1.0 \cdot 10^{16} \text{ cm}^{-3}$, and a layer thickness: .05cm.

Inserting MOSES I parameters into the circuit model, a run for the conduction phase and opening phase, induced by the quick drop of β requires an estimate of the time to flash the AK1 gap and thus extinguish the high voltage opening phase. In the circuit model this is done by giving a time difference, a lifetime of the high voltage phase, at the beginning of a run. The difference in the opening and closing time which works to describe the observations is well approximated by

$$v_n(E = 0.1 E_{peak, \beta_n})(\tau_{close} - \tau_{open}) \approx (d_{AK1} - d_{AK2}) ,$$

where the electric field is that associated with the **equilibrium solution for the observed current enhancement factor**.

From the experience to date in our modeling we can make the following conclusions and recommendations.

- The basic assumption of the *PI* scaling is borne out by these preliminary studies.
- The implied circuit behavior does roughly agree with experiment if one fixes, through this evaluation of the charge exchange neutral fluxes, the gap breakdown times.
- **Measurements** are needed to set the plasma densities near the anode if a more detailed investigation is needed.

- Testing such refinements in the context of the experiment with a relevant and cheap circuit model is useful.

General References

- (1.) J.M.Creedon,et.al, *J.Appl.Phys.*,**57**(5), 1582, (1985).
- (2.) M.Krishnan and P.Sincerny, "The Inductive Store Simulator Development Program at PI", PIIR 1-88, Feb 3, 1988.
- (3.) D.S.Prono,et.al, *J.Appl.Phys.*,**46**(8), 3310 (1975)
- (4.) H.A.Bethe,"Moliere's theory of multiple scattering", *Phys.Rev.*,**89**, 1256 (1952).
- (5.) I.Langmuir,"The interaction of electron and positive ion space charges in cathode sheaths", *Phys.Rev.*,**33**, 954 (1929).
- (6.) R.E.Terry, J.M.Les, J.L.Geary, J.J.Ambrosiano, N.R.Pereira, "Continuum Theory of the Reflex Triode", DNA Pulse Power Conference, NVOO, April 1988.
- (7.) R.E.Terry, J.M.Les,J.J.Ambrosiano,"Reflex Triode Closure by Charge Exchange Neutrals", DNA Opening Switch Workshop, September 1988.
- (8.) R.A.Mapleton,Theory of Charge Exchange, Wiley(1972),pp.210-214.

II. Energy Transfer From High Power Pulselines to the Next Generation of PRS Loads

Introduction

The design of more complex loads for Plasma Radiation Sources and the quest for ever higher simulator radiative yields and power levels require heretofore unexplored energy densities in the load region, perhaps as high as 1.50 MJ/cm^3 . Quite apart from detailed design questions, there is some concern that these higher power and energy densities (delivered by "sub-Ohm" pulselines) cannot couple well to the PRS configurations used today¹ or to even higher inductance designs that might be used in the future.

In a separate report² we have examined the energy transfer to two PRS loads from generic pulselines of the Saturn class operating at the $8 - 15 \text{ MA}$ level. Saturn is nearly a 10x machine in terms of power flows and has recently been outfitted with PRS front end hardware. A basic slug PRS model and an appropriate X-pinch model, derived from 2-D MHD simulations, were used.

The pulselines are modeled with a transmission line code. Apart from generalization to spacetime dependent line parameters (impedance, propagation speed, and damping), the solution technique is quite standard, robust, and accurate in its energy transfer characteristics. Even the simplest transmission line models of machines like Saturn provide the expected result - PRS loads will accommodate the line impedance and draw energy effectively. A more delicate question is that of loss mechanisms. This is left to future work.

The coupling of pulsers like Saturn or the Falcon design (proposed by PI as a 10x device) to an X-pinch load was also discussed. The particular load chosen is

first modeled with the 2-D MHD code PRISM to exhibit the behavior we wish to exploit. The inductance history can then be used as a rough guide to the behavior of such loads in Saturn or Falcon class machines.

Results and Conclusions

All the experience to date with this transmission line and load model indicates that for all of the generic machine designs presently contemplated for the 10x machine, for all the likely domains of load stagnation radius, one can state two results with some confidence.

- The front end inductance of a PRS load per se is not a problem for energy coupling, provided this inductance remains in the range $\leq 20\text{nH}$.
- The gas puff PRS load on Saturn should draw at least 8—10 MA in the present configuration.

The observed behavior on Saturn - 10 MA into gas puffs and 12.5 MA into short circuit loads - is quite nicely in line with this prediction.

Furthermore, all the experience to date with the more complex X-pinch load design indicates that (i.) it represents a very credible PRS concept in terms of energy coupling and (ii.) it should be quite compatible with the presently contemplated 10x machine designs. The model we have discussed here will be refined further by 2D MHD studies to include the role of runaway electron populations in the energy budget and to optimize the load dynamics.

More general problems, involving loss mechanisms in MITL segments, can be readily addressed by the method and some initial work is already underway.

References

1. Theoretical and Experimental Comparison of GAMBLE II Argon Gas Puff Experiments, J. W. Thornhill, et. al., NVOO Proceedings, to be published, 1988.
2. R.E.Terry and F.L.Cochran, NRL Memo Rep. (in preparation), 1988, "Energy Transfer From High Power Pulselines to the Next Generation of PRS Loads".

DISTRIBUTION LIST

Assistant to the Secretary of Defense Atomic Energy Washington, D.C. 20301 Attn: Executive Assistant	1 copy
Director Defense Nuclear Agency Washington, D.C. 20305 Attn: DDST TITL RAEV STVI	1 copy 4 copies 1 copy 1 copy
Commander Field Command Defense Nuclear Agency Kirtland AFB, New Mexico 87115 Attn: FCPR	1 copy
Chief Field Command, Livermore Division Department of Defense Post Office Box 808 Livermore, California 94550 Attn: FCPRL	1 copy
Director Joint Strat TGT Planning Staff Offutt AFB Omaha, Nebraska 68113 Attn: JLKS	1 copy
Undersecretary of Defense for RSCH and ENGRG Department of Defense Washington, D.C. 20301 Attn: Strategic and Space Systems (OS)	1 copy
Deputy Chief of Staff for RSCH DEV and ACQ Department of the Army Washington, D.C. 20301 Attn: DAMA-CSS-N	1 copy
Commander Harry Diamond Laboratories Department of the Army 2800 Powder Mill Road Adelphi, Maryland 20783 Attn: DELHD-N-NP DELHD-R J. Rosado DELHD-TA-L (Tech. Lib.)	1 copy each

U.S. Army Missile Command
Redstone Scientific Information Center
Attn: DRSMI-RPRD(Documents)
Redstone Arsenal, Alabama 35809

3 copies

Commander
U.S. Army Nuclear and Chemical Agency
7500 Backlick Road
Building 2073
Springfield, Virginia 22150
Attn: Library

1 copy

Commander
Naval Intelligence Support Center
4301 Suitland Road, Bldg. 5
Washington, D.C. 20390
Attn: NISC-45

1 copy

Commander
Naval Weapons Center
China Lake, California 93555
Attn: Code 233 (Tech. Lib.)

1 copy

Officer in Charge
White Oak Laboratory
Naval Surface Weapons Center
Silver Spring, Maryland 20910
Attn: Code R40
Code F31

1 copy each

Air Force Weapons Laboratory
Kirtland AFB, New Mexico 87117
Attn: Dr. William Baker
SUL
CA

1 copy each

Deputy Chief of Staff
Research, Development and Accounting
Department of the Air Force
Washington, D.C. 20330
Attn: AFRDQSH

1 copy

Commander
U.S. Army Test and Evaluation Command
Aberdeen Proving Ground, Maryland 21005
Attn: DRSTE-EL

1 copy

Auburn University Department of Physics Attn: Dr. J. Perez Auburn, Al 36849	1 copy
AVCO Research and Systems Group 201 Lowell Street Wilmington, Massachusetts 01887 Attn: Library A830	1 copy
BDM Corporation 7915 Jones Branch Drive McLean, Virginia 22101 Attn: Corporate Library	1 copy
Berkeley Research Associates Post Office Box 983 Berkeley, California 94701 Attn: Dr. Joseph Workman	1 copy
Berkeley Research Associates Post Office Box 852 5532 Hempstead Way Springfield, Virginia 22151 Attn: Dr. Joseph Orens	1 copy each
Boeing Company Post Office Box 3707 Seattle, Washington 98134 Attn: Aerospace Library	1 Copy
The Dikewood Corporation 1613 University Blvd., N.E. Albuquerque, New Mexico 87110 Attn: L. Wayne Davis	1 copy
General Electric Company - Tempo Center for Advanced Studies 816 State Street Post Office Drawer QQ Santa Barbara, California 93102 Attn: DASIAC	1 Copy
Institute for Defense Analyses 1801 N. Beauregard Street Alexandria, Virginia 22311 Attn: Classified Library	1 copy
IRT Corporation Post Office Box 81087 San Diego, California 92138 Attn: R. Mertz	1 copy

JAYCOR 1608 Spring Hill Road Vienna, Virginia 22180 Attn: R. Sullivan	1 copy
JAYCOR 11011 Forreyane Road Post Office Box 85154 San Diego, California 92138 Attn: E. Wenaas F. Felbar	1 copy
KAMAN Sciences Corporation Post Office Box 7463 Colorado Springs, Colorado 80933 Attn: Library	1 copy each
Lawrence Livermore National Laboratory University of California Post Office Box 808 Livermore, California 94550 Attn: DOC CDN for 94550 DOC DCN for L-47 L. Wouters DOC CDN for Tech. Infor. Dept. Lib.	1 copy each
Lockheed Missiles and Space Company, Inc. Post Office Box 504 Sunnyvale, California 94086 Attn: S. Taimlty J.D. Weisner	1 copy each
Maxwell Laboratory, Inc. 9244 Balboa Avenue San Diego, California 92123 Attn: A. Kolb M. Montgomery J. Shannon K. Ware	1 copy ea.
McDonnell Douglas Corporation 5301 Bolsa Avenue Huntington Beach, California 92647 Attn: S. Schneider	1 copy
Mission Research Corporation Post Office Drawer 719 Santa Barbara, California 93102 Attn: C. Longmire	1 copy each
Mission Research Corporation-San Diego 5434 Ruffin Road San Diego, California 92123 Attn: Victor J. Van Lint	1 copy

Northrop Corporation Northrop Research & Technology Center 1 Research Park Palos Verdes Peninsula, California 90274	1 copy
Physics International Company 2700 Merced Street San Leandro, California 94577 Attn: M. Krishnan C. Denney T. Nash	1 copy each
R and D Associates Post Office Box 9695 Marina Del Rey, California 90291 Attn: Library	1 copy each
Sandia National Laboratories Post Office Box 5800 Albuquerque, New Mexico 87115 Attn: Doc Con For 3141 D. McDaniel P. VanDevender K. Matzen, Code 4247	1 copy each
Science Applications, Inc. 10260 Campus Point Drive Mail Stop 47 San Diego, California 92121 Attn: R. Beyster	1 copy
Spectra Technol, Inc., 2755 Northup Way Bellevue, Washington 98004 Attn: Alan Hoffman	1 copy
Spire Corporation Post Office Box D Bedford, Massachusetts 07130 Attn: R. Little	1 copy
S-CUBED Post Office Box 1620 La Jolla, California 92038 Attn: A. Wilson	1 copy
Director Strategic Defense Initiative Organization Pentagon 20301-7100 Attn: DE Lt. Col Richard Gullickson/DEO IST Dr. Dwight Duston IST Dr. Jonathan Farber	1 copy each

Texas Tech University
Post Office Box 5404
North College Station
Lubbock, Texas 79417
Attn: T. Simpson

1 copy

TRW Defense and Space Systems Group
One Space Park
Redondo Beach, California 90278
Attn: Technical Information Center

1 copy

Naval Research Laboratory
Plasma Radiation Branch
Washington, D.C. 20375
Code 4720 - 50 copies
4700 - 26 copies

Do NOT make labels
for these two-below:
Records-(1 copy)
Code 2628 (22 cys)

Naval Research Laboratory
Washington, DC 20375-5000
Code 2630
Timothy Calderwood

CODE 1220

1 COPY

DIRECTOR OF RESEARCH
U. S. NAVAL ACADEMY
ANNAPOLIS, MD 21402

2 COPIES